EFFICIENT GEOMECHANICAL SIMULATIONS OF LARGE-SCALE NATURALLY FRACTURED RESERVOIRS USING THE FAST MULTIPOLE-DISPLACEMENT DISCONTINUITY METHOD (FM-DDM)

A Dissertation

by

ALEXANDER JOSE VERDE SALAS

Submitted to the Office of Graduate and Professional Studies of
Texas A&M University
in partial fulfillment of the requirements for the degree of

DOCTOR OF PHILOSOPHY

Chair of Committee,	Ahmad Ghassemi
Committee Members,	Peter Valko
	Eduardo Gildin
	Benchun Duan
Head of Department,	A. Daniel Hill

May 2014

Major Subject: Petroleum Engineering

ABSTRACT

Geothermal and unconventional reservoirs play an important role in supplying fuel for a growing energy demand in the United States. The development of such reservoirs relies on creating a fracture network to provide flow and transport conduits during injection and production operations. The Displacement Discontinuity Method (DDM) is frequently used for modeling the behavior of fractures embedded in elastic and poroelastic rocks. However, DDM requires the calculation of the influence among all fractures being computationally inefficient for large systems of cracks. It demands quadratic and cubic complexity of memory and solution time by direct methods, respectively, limiting its application to only small-scale situations.

Recent fast summation techniques such as the Fast Multipole Method (FMM) have been used to speed up the solution of several boundary element problems using modest computational resources. FMM relies in accelerating matrix-vector products in iterative methods by splitting the computation of the influences among elements into near and far-field interactions. While the former are calculated similarly to the conventional DDM, the latter, where most of the interactions are found, are efficiently approximated by the FMM using analytical multipole and local expansions. However, in spite of its immediately apparent application in the geomechanic context, FMM has been limited to only certain fracture problems because those analytical expansions are only available for selected fundamental solutions and the development for new ones requires complex mathematical derivations even for those kernels of simple form.

This work presents a new method called Fast Multipole–Displacement Discontinuity Method (FM-DDM) for an efficient flow-geomechanical simulation of large-scale naturally fractured reservoirs undergoing fluid injection and extraction. The approach combines both DDM and FMM using for the latter a kernel-independent version where multipole and local expansions are not required opening a range of potential applications within the geothermal and oil industries. Several case studies involving fracture networks with up to one hundred thousands of boundary elements were presented to evaluate accuracy, computational efficiency and applications of the FMM approach. From the results, FM-DDM showed an excellent agreement with well-known benchmark solutions outperforming DDM with linear complexity in both memory and execution time. In addition, a variety of large-scale geomechanical applications were efficiently evaluated with FM-DDM involving interactions between transverse hydraulic fractures and a fracture network, fast visualization of high-resolution stress distribution, and the design of exploitation strategies in elastic and poroelastic fractured reservoirs.

DEDICATION

To my parents for their love, education, and heartwarming words that renewed my confidence during this academic endeavor.

To my brothers for their continuous support, who are always thinking and wishing the best for me.

To my wife for her patience and trust who gave me the time and freedom to pursue this career goal even though this meant being apart for a long time. And for her love, that filled up my life with happiness and hope and under which our daughter was born, the most special gift I could ever have been given.

To all my friends and rest of my family who have supported me throughout the process.

ACKNOWLEDGEMENTS

Thanks to Texas A&M University and particularly the Harold Vance Department of Petroleum Engineering for accepting me in the doctoral program which has opened new horizons in my career and better professional opportunities.

I would like also to thank my committee chair, Dr. Ghassemi for the financial support of my research studies in the field of geomechanics and for giving me the opportunity to work on an interesting and challenging project and the freedom to explore and develop new ideas. A special thanks to Dr. Valko, who introduced me in the area of fractured reservoir modeling, for contributing in the financial support of my initial research activities and in general for his willingness in helping me.

I offer my most sincere gratitude for the other committee members, Dr. Duan and Dr. Gildin, for their guidance and friendship throughout the course of my research. Thanks also to Dr. Eric Darve from the Mechanics and Computation Group at Stanford University for providing the source code of the Black-Box FMM.

TABLE OF CONTENTS

LIST OF FIGURES

Page

Page

Page

LIST OF TABLES

1. INTRODUCTION

Geothermal and unconventional petroleum reservoirs contain vast resources to supply the energy demand in the United States. However due to their ultra-low permeability, the development of such reservoirs depends mainly on the ability to transport the underground fluid to the surface through extensive natural fracture networks subjected to geoemachanical deformation of the rock and fractures. In these reservoirs, natural fractures represent the main channels for the movement of the fluid during injection and production operations. They are usually densely packed and interconnected forming large and complex networks subjected to different physical phenomena (e.g., fluid-flow and diffusion, deformation, elastic and poroelastic effects) that control the processes of fracture initialization, and propagation. As the later governs the flow pattern and total heat and fluid recovery in the reservoir (Bagheri and Settari 2005; Jalali and Dusseault 2008), large-scale numerical simulations are necessary for a realistic representation of those unconventional reservoirs to model their complexity with a high level of details for the proper design of exploitation strategies. This section will begin with an explanation of the problem followed by a literature review of previous works focused on large-scale fracture modeling. Finally, the objectives and a summary of the dissertation will be presented.

1.1. Problem definition

Modeling fractures embedded in linear-elastic rock relies on solving conservative (i.e., mass, momentum, equilibrium) and constitutive (i.e., Darcy's law, poroelasticity) equations for the fluid and solid matrix. Among the available numerical techniques for solving those equations, the Displacement Discontinuity Method (DDM) (Crouch 1984), an indirect Boundary Element Method (BEM), provides an alternative to the prevailing domain methods in continuum mechanics such as Finite Differences (FDM) or Finite Elements (FEM) Methods (Tao et al. 2009a; Tao et al. 2009b; Tao and Ghassemi 2010). DDM is frequently used due to its semi-analytical nature and because it reduces the dimensionality of the problem by needing only the discretization of the boundary. Therefore, DDM is suitable for modeling linear problems with small surface-volume ratio (cavities within an infinite medium) and due to its semi-analytical nature it is more accurate than FDM and FEM becoming a powerful tool for fracture mechanic analysis. The basis behind DDM is to transform the original partial differential equations that define a physical problem into equivalent boundary integral equations (BIE) by means of fundamental solutions and then solve the corresponding integral equations by numerical methods.

DDM has been extensively applied in mining and hydraulic fracturing (Curran and Carvalho 1987; Tao et al. 2009a; Tao et al. 2009b; Tao and Ghassemi 2010). However, DDM requires computing the influences among all fracture elements so the coefficient matrix of the system of equations is dense and nonsymmetrical. This requirement impacts the computational performance of conventional strategies, either direct or iterative, for the solution of the system of equations when large numbers of elements are involved making DDM computationally intensive. Direct methods such as Gaussian elimination are robust and easy to implement but are limited to solving a few thousands of elements, demanding $O(N^2)$ memory and $O(N^3)$ floating point operations to construct (and store) the matrix and solve the system, where N is the number of degrees of freedom. On the other hand, computational applications (Bängtsson and Neytcheva 2005; Elvin and Leung 1999; Kolk et al. 2006) based on iterative algorithms such as the Generalized Minimum Residual Method (GMRES) still need $O(N^2)$ memory but are able to solve larger systems because the number of algebraic operations are reduced to $O(kN^2)$, where k is the number of iterations to achieve convergence. If preconditioning algorithms are implemented (Bängtsson and Neytcheva 2005; Kolk et al. 2006), additional reduction of computation can be achieved making k virtually independent of N ($k<<N$). However, realistic representation of most fracture problems of interest that involve a high number of boundary elements are still beyond the current capability of personal computers because matrix-vector products become prohibitive, so other methods are necessary to make improvements.

1.2. Literature review

During the last two decades, fast summation techniques such as the Fast Multipole Method (FMM) (Greengard and Rokhlin 1987) have improved the performance of some boundary-value problems in terms of memory requirements and CPU time (Liu 2009; Nishimura et al. 1999; Wang, H. et al. 2005; Wang and Yao 2005;

Wang, P. et al. 2005; Wang et al. 2007; Yoshida et al. 2001b). FMM has been regarded as one of the top 10 algorithms in scientific computing created in the 20th century (Board and Schulten 2000). Originally developed to solve electrostatic and gravitation problems, it has been now successfully applied to many other (Fu et al. 1998; Li and Huang 2011; Liu and Shen 2005; Tornberg and Greengard 2008) scientific problems (See Figure 1-1). The FMM relies on an iterative strategy in which the matrix-vector multiplication is accelerated without forming the coefficient matrix explicitly. This acceleration is carried out by efficiently calculating the interaction between elements using the same BEM discretization but by recursive operations of a quad-tree structure for computation and storage. It permits the solution of larger problems by combining the robustness and accuracy of conventional BEM but with superior performance (See Figure 1-2).

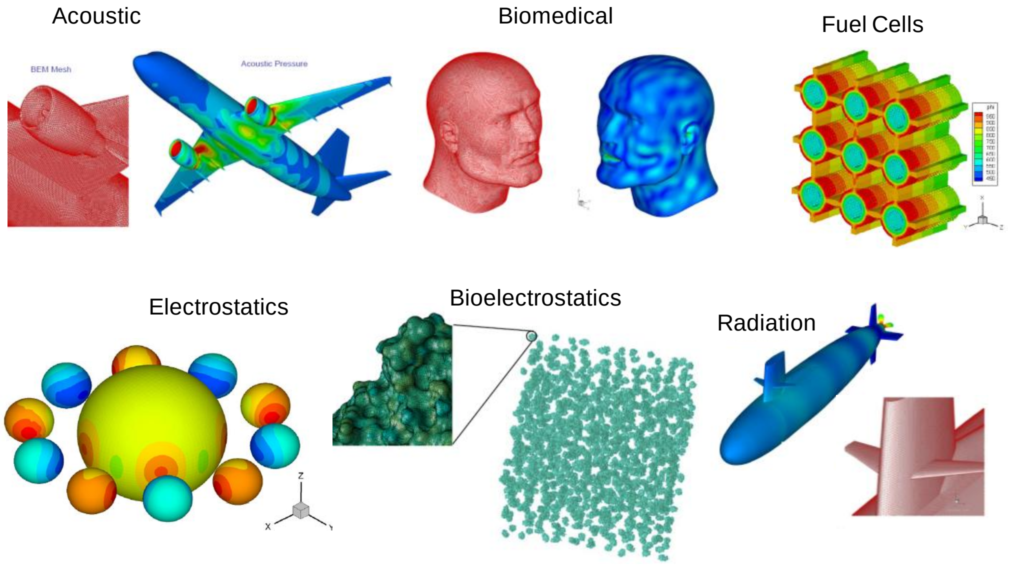

Figure 1-1. Applications of the FMM for the solution of several large-scale scientific problems (Liu 2009).

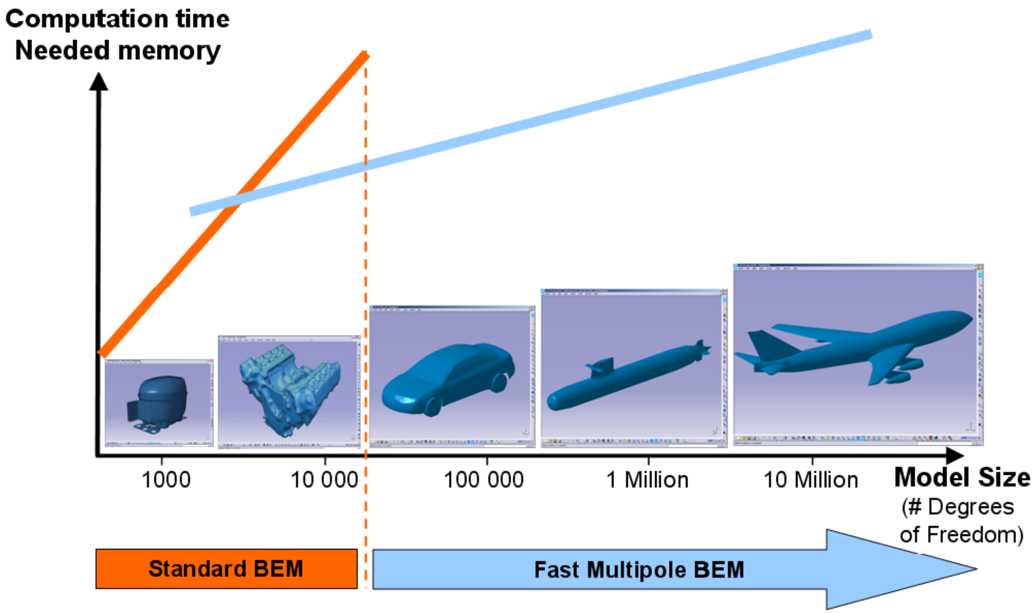

Figure 1-2. Comparison of the typical computational performance of BEM and FMM for different problem sizes. In general, FMM solves for large problems and exhibits a linear complexity with unit slope in a log-log plot.

However, and in contrast to its immediately apparent application, FMM has not been extensively applied in combination with the DDM mainly because of the difficulty of understanding FMM and lack of mathematical developments for the fundamental solutions of interest as well as high programming complexity. Previous works using both DDM and FMM has been limited to elastic rocks (Morris and Blair 2000; Peirce and Napier 1995). Both studies used the available mathematical developments of FMM in electrostatic potential for two-dimensional problems.

Peirce and Napier (Peirce and Napier 1995) were the first to explore this area introducing a spectral version of the FMM. They proposed a potential representation of the fundamental solutions to approximate the normal and shear displacement discontinuities applying the method to the granular assemblies problem using a maximum of 1800 boundary elements. Although the approach provides memory savings of $O(N)$, its computational implementation is quite inefficient demanding $O(N^2\mathrm{Log}N)$ operations. On the other hand, Morris and Blair (Morris and Blair 2000) explored the problem of discontinuities within an elastic solid for simulating a brittle rock fracture with up to 22,500 fracture elements. In their work, the far-field behavior of the fundamental solutions is approximated by decaying kernels of the form $\mathrm{Log}(r)$, where r is the distance between source and field points. However, such approximation is accurate if the interacting elements are separated by a distance greater than a certain number element lengths. This condition restricts the maximum number of levels in the quad-tree and then increases the amount of fractures contained in the cells for near interactions. Because these interactions are computed directly as in the conventional DDM, the efficiency of the algorithm is deteriorated when the cells enclose high numbers of elements. Moreover, the implementation requires the evaluation of 27 unique multipoles to perform the matrix-vector multiplication, presumably producing an ideal $O(N)$ behavior only for certain element arrangements.

Others FMM implementations based on multipole expansions have been reported in the literature for modeling elastic but unconnected linear (Wang, H. et al. 2005; Wang, P. et al. 2005; Wang et al. 2007; Wang and Yao 2006; Yao et al. 2007), circular (Lai and Rodin 2003; Pham et al. 2012; Yoshida et al. 2001a, 2001b; Yoshida), and penny-shape (Nishimura et al. 1999; Pham et al. 2012; Yoshida et al. 2001a, 2001b; Yoshida) fractures problems in absence of fluid-flow. However, these works use a direct formulation of the boundary element method usually called Fast Multipole-Boundary

Element Method (FMBEM) not suitable for modeling fractures problems in unbounded reservoir domains so that they are out of the scope of this work.

In recent years, a new FMM formulation called “black-box” has been developed which does not require the implementation of multiple expansions of the underlying kernel but only the kernel evaluations (Fong and Darve 2009). This FMM formulation differs from the previous ones (Morris and Blair 2000; Peirce and Napier 1995) and is very useful for problems where the kernel is known analytically but is quite complicated for which analytical expansions might be difficult to obtain. The complexity of the method would be completely hidden from the end-user which opens up a range of potential applications to more general problems. This kernel-independent version exhibits the same structure and performance of the classical FMM but it is simpler to implement. Table 1-1 presents a summary of previous works discussed above for solving large-scale fracture problems using FMM showing potential contributions of the proposed approach.

This work presents a novel approach called Fast Multipole – Displacement Discontinuity Method (acronymed as FM-DDM) by combining DDM and a kernel-independent version of the classical FMM for the efficient solution of the coupled fluid flow-geomechanical problem in large-scale naturally fractured reservoirs subjected to injection and production operations.

Table 1-1. Summary of previous works for solving large-scale fracture problems using FMM showing potential contributions of the proposed approach.

Author/Year		(Peirce and Napier 1995)	(Morris and Blair 2000)	(Lai and Rodin 2003; Nishimura et al. 1999; Pham et al. 2012; Wang, H. et al. 2005; Wang, P. et al. 2005; Wang et al. 2007; Wang and Yao 2006; Yao et al. 2007; Yoshida et al. 2001a, 2001b; Yoshida)	Current work
Fracture problem formulation	Direct			X	
	Indirect (DDM)	X	X		X
Fast Multipole formulation	Multipole-based[†]	X	X	X	
	Kernel-independent				X
Fracture model components	Rock type	Elastic	Elastic	Elastic	Elastic/Poroelastic
	Joint				X
	Fluid-flow				X
	Rock failure		X		
Numerical examples	No. of elements	1800	22,500	10^4 - 10^6	~10^5
	Performance	$O(N^2 \text{Log} N)$	$O(N)$[‡]	$O(N \log N)$ - $O(N)$	$O(N)$
	Application	Mining	Brittle rock	No specific purpose	Reservoir geomechanics

1.3. Objectives

The proposed research will accomplish the following objectives:

[†] Loss of accuracy is present due to a necessary simplification of kernels

[‡] Only for certain element arrangements.

1. Develop a computational implementation of the Fast Multipole Method with the Displacement Discontinuity Method (acronymed as FM-DDM) to estimate the coupled fluid flow-geomechanical response of large-scale naturally fractured reservoirs under injection and production operations.
2. Evaluate the accuracy of the FMM approach and compare its computational performance with the conventional DDM in terms of the memory requirements and execution time.
3. Evaluate several two-dimensional configurations of large-scale fracture networks under elastic and poroelastic conditions using the FM-DDM.

1.4. Summary of the dissertation

Section 1 explains the problem of interest and its relevance and presents a critical review of previous works in the area followed by the objectives of the research. Section 2 formally describes the conventional DDM for modeling the geomechanical response of naturally fractured reservoirs undergoing fluid injection and production. Three geomechanical models of increasing complexity are proposed to describe the fluid flow phenomenon through elastic and poroelastic fracture networks. Section 3 presents a general description of the FMM for the solution of large-scale boundary-value problems along with its advantages and limitations. Simplified reviews of the classical multipole-based and kernel-independent versions of the FMM are also presented. Section 4 presents the details of the proposed approach called Fast Multipole–Displacement Discontinuity Method (FM-DDM) as well as the numerical procedure and computational implementation. Section 5 presents several cases studies to evaluate the accuracy and computational performance of the FM-DDM on those numerical models described in Section 2 associated with geomechanical conditions of increasing complexity. Section 6 shows large-scale numerical applications to evaluate geomechanical interactions among multiple transverse fractures in unconventional reservoirs and fluid flow-geomechanical problems in elastic and poroelastic fracture networks under fluid injection and extraction. Finally, Section 7 presents the conclusions and recommendations of this research.

2. DISPLACEMENT DISCONTINUITY METHOD (DDM)

The Displacement Discontinuity Method (DDM) (Crouch 1984) is an indirect Boundary Element Method (BEM) that provides an alternative to the prevailing domain methods in continuum mechanics such as finite differences (FDM) or finite elements (FEM) methods (Tao et al. 2009a; Tao et al. 2009b; Tao and Ghassemi 2010). The basis behind DDM is to transform the original partial differential equations that define a physical problem into equivalent boundary integral equations (BIE) by means of fundamental solutions and then solve the corresponding integral equations by numerical methods. DDM has been extensively applied in mining and hydraulic fracturing modeling (Curran and Carvalho 1987; Tao et al. 2009a; Tao et al. 2009b; Tao and Ghassemi 2010) due to its semi-analytical nature and ability to reduce the dimensionality of the problem by needing only the discretization of the boundary.

In this work, DDM will be used for modeling the geomechanical response of naturally fractured reservoirs undergoing fluid injection and production. To facilitate the integration with the FMM and the corresponding verification process, three (3) geomechanical models of increasing complexity are proposed in this section to gradually integrate the physical phenomena involving Elastic Deformation (ED), Flow-Elastic Deformation (FED), and Flow-Poroelastic Deformation and Difussion (FPDD).

2.1. Elastic Deformation (ED) model

DDM can be used for modeling the normal (opening) and shear (ride) displacement discontinuities of fractures embedded in an infinite and elastic medium (Crouch 1984). The method is based on fundamental or analytical solutions to the problem of a finite segment fracture centered in a Cartesian plane with constant normal and shear discontinuities in displacement (see Figure 2-1). The displacement discontinuity, D_i, is defined as the difference in displacement between the two sides of the segment as:

$$D_i = u_i(x_1, 0_-) - u_i(x_1, 0_+) \; i = n, s \tag{2-1}$$

The fundamental solutions provide expressions to compute the induced stresses (σ_{xx}, σ_{yy}, and σ_{xy}) at any field point (x,y) of the domain caused by displacement discontinuities (D_n and D_s) of the fracture with its center at the origin (source) (Crouch 1984):

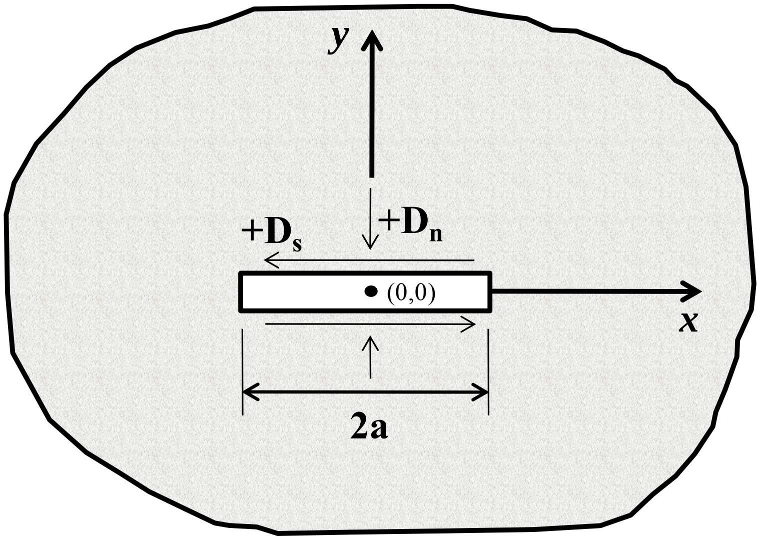

Figure 2-1. Fracture segment embedded in a two-dimensional and infinite medium showing constant normal and shear discontinuity displacements.

$$\sigma_{xx} = 2G\big(2f_{,xy} + yf_{xyy}\big)D_s + 2G\big(f_{,yy} + yf_{,yyy}\big)D_n \tag{2-2}$$

$$\sigma_{yy} = 2G\big(-yf_{,xyy}\big)D_s + 2G\big(f_{,yy} - yf_{,yyy}\big)D_n \tag{2-3}$$

$$\sigma_{xy} = 2G\big(f_{,yy} + yf_{,yyy}\big)D_s + 2G\big(-yf_{,xyy}\big)D_n \tag{2-4}$$

where:

$$f(x,y) = -\frac{1}{4\pi(1-\nu)}\left[\begin{matrix} y\left(tg^{-1}\dfrac{y}{x-a} - tg^{-1}\dfrac{y}{x+a}\right) - \\ (x-a)ln\sqrt{(x-a)^2+y^2} + (x+a)ln\sqrt{(x+a)^2+y^2} \end{matrix}\right] \tag{2-5}$$

whete f is the relative position function between the source and field points, G is the shear modulus, ν represents the Poisson's ratio of the solid medium, and a the fracture half-length.

For a curvy fracture in an infinite two-dimensional medium, its length needs to be divided into *j* fracture segments, each one with a local coordinate system whose *x*-axis is parallel to the orientation of the *jth* fracture segment (See Figure 2-2). As the fundamental solutions (Eqs. (2-2) to (2-4)) are defined for a fracture element parallel to the *x*-axis and centered at the origin, the following coordinate transformations are necessary to compute the effects of one of these fracture segments in a field point (*x*,*y*) at the global coordinate system:

$$\bar{x} = \big(x - x_j\big)cos\beta_j + \big(y - y_j\big)sin\beta_j \tag{2-6}$$

$$\bar{y} = \big(x - x_j\big)sin\beta_j + \big(y - y_j\big)cos\beta_j \tag{2-7}$$

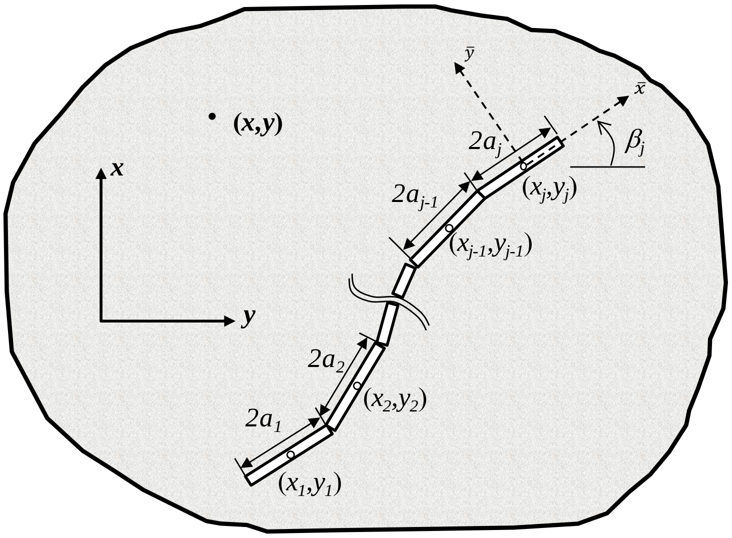

Figure 2-2. Two-dimensional medium with a curvy fracture divided by *j* fracture segments showing global and local coordinate system.

where β_j is the angle of the *jth* fracture segment with the x-axis. Now, the induced stresses on the field point in the local *x,y* co-ordinate system by the normal and shear displacement discontinuity of the *jth* fracture are:

$$\sigma_{\bar{x}\bar{x}} = 2G\left(2f_{,\bar{x}\bar{y}} + \bar{y}f_{,\bar{x}\bar{y}\bar{y}}\right)D_s + 2G\left(f_{,\bar{y}\bar{y}} + \bar{y}f_{,\bar{y}\bar{y}\bar{y}}\right)D_n \tag{2-8}$$

$$\sigma_{\bar{y}\bar{y}} = 2G\left(-\bar{y}f_{,\bar{x}\bar{y}\bar{y}}\right)D_s + 2G\left(f_{,\bar{y}\bar{y}} - \bar{y}f_{,\bar{y}\bar{y}\bar{y}}\right)D_n \tag{2-9}$$

$$\sigma_{\bar{x}\bar{y}} = 2G\left(f_{,\bar{y}\bar{y}} + \bar{y}f_{,\bar{y}\bar{y}\bar{y}}\right)D_s + 2G\left(-\bar{y}f_{,\bar{x}\bar{y}\bar{y}}\right)D_n \tag{2-10}$$

where the spatial derivatives of influence function *f* are denoted by F_4, F_5, F_6, and F_7 and defined as follow:

$$f_{,\bar{x}\bar{y}} = F_4(\bar{x},\bar{y}) = \frac{1}{4\pi(1-v)}\left[\frac{\bar{y}}{(\bar{x}-a)^2+\bar{y}^2} - \frac{\bar{y}}{(\bar{x}+a)^2+\bar{y}^2}\right] \tag{2-11}$$

$$f_{,\bar{x}\bar{x}} = -f_{,\bar{y}\bar{y}} = F_5(\bar{x},\bar{y}) = \frac{1}{4\pi(1-v)}\left[\frac{\bar{x}-a}{(\bar{x}-a)^2+\bar{y}^2} - \frac{\bar{x}+a}{(\bar{x}+a)^2+\bar{y}^2}\right] \tag{2-12}$$

$$f_{,\bar{x}\bar{y}\bar{y}} = -f_{,\bar{x}\bar{x}\bar{x}} = F_6(\bar{x},\bar{y})$$

$$= \frac{1}{4\pi(1-v)}\left[\frac{(\bar{x}-a)^2-\bar{y}^2}{\{(\bar{x}-a)^2+\bar{y}^2\}^2} - \frac{(\bar{x}+a)^2-\bar{y}^2}{\{(\bar{x}+a)^2+\bar{y}^2\}^2}\right] \tag{2-13}$$

$$f_{,\bar{y}\bar{y}\bar{y}} = -f_{,\bar{x}\bar{x}\bar{y}} = F_7(\bar{x},\bar{y})$$

$$= \frac{2\bar{y}}{4\pi(1-v)}\left[\frac{\bar{x}-a}{\{(\bar{x}-a)^2+\bar{y}^2\}^2} - \frac{\bar{x}+a}{\{(\bar{x}+a)^2+\bar{y}^2\}^2}\right] \tag{2-14}$$

Finally, by using the superposition method, the induced stresses at a field point *i* caused by the effect of *m* fractures at different source locations can be computed as the sum of the contributions of the *m* fracture segment involved. After rotating the stresses components to the normal (σ_n) and shear directions (σ_s), we have:

$$\sigma_s^i = \sum_{j=1}^{m} A_{ss}^{ij} D_s^j + \sum_{j=1}^{m} A_{sn}^{ij} D_n^j \tag{2-15}$$

$$\sigma_n^i = \sum_{j=1}^{m} A_{ns}^{ij} D_s^j + \sum_{j=1}^{m} A_{nn}^{ij} D_n^j \tag{2-16}$$

with

$$\sigma_s^i = (\sigma_{yy}^{\infty} - \sigma_{xx}^{\infty}) sin\beta_j cos\beta_j + \sigma_{xy}^{\infty}(cos\beta_j{}^2 - sin\beta_j{}^2) \tag{2-17}$$

$$\sigma_n^i = \sigma_{xx}^{\infty} sin\beta_j{}^2 - 2\sigma_{xy}^{\infty} sin\beta_j cos\beta_j + \sigma_{yy}^{\infty} cos\beta_j{}^2 \tag{2-18}$$

and

$$\sigma_n^{i\,\prime} = \sigma_n^i - P \tag{2-19}$$

where $\sigma_n^{i\,\prime}$ is the effective normal stress, *P* is the fluid pressure, and σ_{xx}^{∞}, σ_{yy}^{∞}, and σ_{xy}^{∞} are the field stress components in *xx*, *yy*, and *xy* directions, respectively. Note that the coefficients A_{sn}, A_{ss}, A_{nn}, and A_{ns} represent the global influence containing multiple spatial derivative of $f(\bar{x}, \bar{y})$ and depending of the relative position of the element i and j and upon the orientation and length of fracture element j. If the mechanical responses of a natural fracture (joint) over the initial stress field ($\sigma_{s,n}\big|_0^\infty$) is taken into account (Tao et al. 2009b) then the total displacement discontinuities are solved simply by adding local or self-influence coefficients to Eqs. (2-15) and (2-16):

$$-\left(\sigma_s^i\right)_0^\infty = K_s^i D_s^i + \sum_{j=1}^{m} A_{ss}^{ij} D_s^j + \sum_{j=1}^{m} A_{sn}^{ij} D_n^j \tag{2-20}$$

$$-\left(\sigma_n^i\right)_0^\infty = K_n^i\left(D_n^i + D_s^i \tan\emptyset_d\right) + \sum_{j=1}^{m} A_{ns}^{ij} D_s^j + \sum_{j=1}^{m} A_{nn}^{ij} D_n^j \tag{2-21}$$

where ($\sigma_{s,n}\big|_0^\infty$) is the initial stress field, K_s and K_n represent the normal and shear joint stiffness, respectively, and $\emptyset_d$ is the dilation angle which account for the increase of joint aperture by shear displacement. Based on the Goodman model (Goodman 1976), K_n is estimated via an hyperbolic equation as a function of the initial stiffness (K_{ni}) and maximum closure (D_{nmax}):

$$K_n = K_{ni}\left(1 - \frac{\acute{\sigma_n}}{K_{ni}D_{nmax} + \acute{\sigma_n}}\right)^{-2} \tag{2-22}$$

In a problem with multiple field and source points, a linear system of equations can be formed by setting up the field locations equal to the source points as:

$$[A]\{x\} = \{b\} \tag{2-23}$$

where A is the coefficient matrix, b is a vector of stresses, and x represents the shear and normal displacement discontinuities. Given the stresses as boundary conditions, the displacement discontinuities can be obtained by solving the linear system of equations.

2.2. Flow-Elastic Deformation (FED) model

This model incorporate the fluid flow phenomenon through the fracture network and account for simultaneous changes of normal and shear displacements discontinuities as well as fluid pressure. The FED model extends the previous ED one which assumes constant pressure in the fracture and has limited applicability for the geothermal and oil industries. In this model, the change in time of the traction components to the normal (Δt_n) and shear (Δt_s) directions expressed in Eqs. (2-20) and (2-21) can be re-written as:

$$\Delta t_s^i = K_s^i \Delta D_s^i + \sum_{j=1}^{m} A_{ss}^{ij} \Delta D_s^j + \sum_{j=1}^{m} A_{sn}^{ij} \Delta D_n^j = 0 \qquad (2\text{-}24)$$

$$\Delta t_n^{i\,\prime} = K_n^i \left(\Delta D_n^i + \Delta D_s^i \tan \emptyset_{\mathrm{d}} \right) + \sum_{j=1}^{m} A_{ns}^{ij} \Delta D_s^j + \sum_{j=1}^{m} A_{nn}^{ij} \Delta D_n^j = \Delta P_k^i \qquad (2\text{-}25)$$

where ΔP_k^i represents the change of the fluid pressure inside a fracture element i in a given time step *k*. An additional equation (Tao et al. 2009a; Tao et al. 2009b) formed by combining the mass balance equation and Darcy's law is needed for the distribution of fluid pressure in an interconnected fracture network:

$$\frac{k_f w_f}{\mu} \frac{\partial p}{\partial s} = n w_f \Delta L c_f \frac{\partial p}{\partial t} - n \Delta L \frac{\partial D_n}{\partial t} - \Delta L Q_l - q_s \qquad (2\text{-}26)$$

In Eq. (2-26), the term on the left, $\frac{k_f w_f}{\mu} \frac{\partial p}{\partial s}$, is the net flow rate in the fracture, the first right term, $n w_f \Delta L c_f \frac{\partial p}{\partial t}$, represents the change of fluid volume due to fluid expansion or compression, the second right term, $n \Delta L \frac{\partial D_n}{\partial t}$, is the change of fluid volume by fracture deformation. Finally, the third and last right terms, $\Delta L Q_l$ and q_s are the fluid leak-off rate per unit height between fracture and the matrix (neglected in this model), and the production or injection rate per unit formation thickness, respectively.

2.3. Flow-Poroelastic Deformation and Diffusion (FPDD) model

The previous FED model represents an improvement of the ED model after accounting for fluid flow through the fracture network. However, this is still limited to handle more realistic cases involving simultaneously poroelasticity deformation of the fracture and rocks in shale reservoirs as well as fluid leak-off or interface flow between the fracture and porous matrix. However, poroelastic rock simulations are even more time consuming than the elastic case while solving for additional unknowns and by requiring the implementation of computational intensive time-marching schemes for the numerical integration.

2.3.1. Description of poroleasticity effects

The theory of poroelasticity for a fluid saturated rock accounts for the coupled diffusion–deformation mechanism (Biot 1941; Rice and Cleary 1976). Based on this theory, the relation of stress to strain and pore pressure assuming a linear isotropic poroelastic media is given by:

$$\sigma_{ij} = 2G\left[e_{ij} + \delta_{ij}\frac{v}{1-2v}e_{kk}\right] - \delta_{ij}\alpha p \tag{2-27}$$

where σ, p, and e represent the stress, pore pressure and strain, respectively; α, v and G are Biot's poroelastic coefficient, Poisson's ratio, and shear modulus, respectively. On the other hand, δ_{ij} represents the Kronecker delta function and e_{kk} is the volumetric strain. Using Eq. (2-27) in the force balance equation, the Navier equation of poroelasticity is formed as:

$$Gu_{i,kk} + \frac{G}{1-2v}u_{k,ki} - \alpha p_{,i} + F_i = 0 \tag{2-28}$$

where F is the body force (neglected in this work) and u is the solid displacement. The coupled fluid diffusion equation for pressure-dependent fluid density is expressed as follow (Tao et al. 2009b):

$$p_{,ii} = \frac{\mu}{kM}\frac{\partial p}{\partial t} + \frac{\alpha\mu}{k}\frac{\partial e_{kk}}{\partial t} - \frac{\mu Q_s}{k} \tag{2-29}$$

with

$$\frac{1}{M} = \phi c_f + \frac{\alpha - \phi}{K_s} \tag{2-30}$$

where K_s is the bulk modulus of the solid grains, ϕ is the porosity, k is the matrix permeability, μ is the fluid viscosity, Q_s is the volumetric flow rate, and c_f is the fluid compressibility.

Note in Eqs. (2-28) and (2-29) that the fluid diffusion in a rock matrix induces porous matrix deformation and stress redistribution, and that porous matrix deformation also induces fluid flow and fluid pressure redistribution. Also when fractures are presented in the porous media, their opening or closing will induce the deformation not only of the porous matrix and but also pore-pressure and fluid flow (Curran and Carvalho 1987; Goodman 1976; Wang 2000). In this work, however, we only consider a one-way coupling and neglect the second term on the right-hand-side of Eq. (2-29).

2.3.2. Poroelastic geomechanical model

The displacement discontinuity method (DDM) is used again to numerically solve the poroelastic equations (2-28) to (2-29), under prescribed conditions on the boundary of the region of interest, to solve for simultaneous changes of the normal (n) and shear (s) displacement discontinuities, fluid leak-off rate and pore-pressure (see Fig. 2-3). This is accomplished by first transforming those partial differential equations into an integral representation by using fundamental solutions which are analytical solutions corresponding to singular impulses (e.g., displacement discontinuities, point fluid source) at a point in an infinite region. Then using the superposition method, the integral equations are numerically approximated by dividing the boundary Γ (or fracture surface in our case) into N elements and distributing those singular impulses on the elements so that the combine effects of all them satisfy the boundary conditions (e.g., stresses).

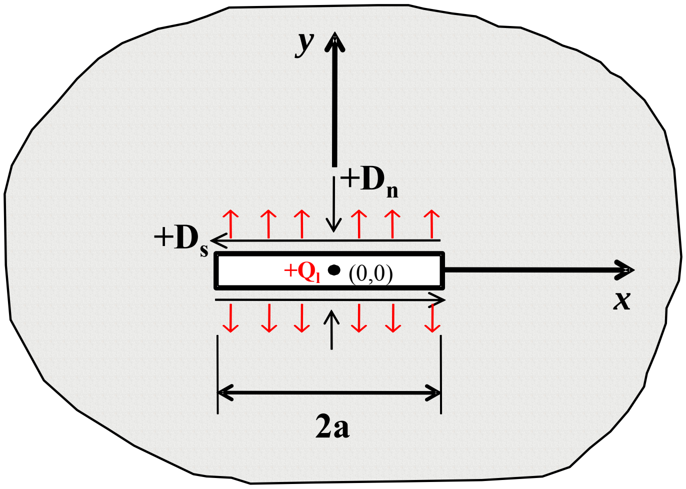

Figure 2-3. Fracture segment embedded in a two-dimensional and infinite porous medium showing constant normal and shear discontinuity displacements and interface flow between the fracture and porous matrix.

For a fracture problem in a poroelastic rock with a one-way coupling, the following two (2) integral equations for the stresses and pore pressure are required to be solved in space and time:

$$\sigma_{ij}(\boldsymbol{x},t) = \int_0^t \int_\Gamma \left\{\sigma_{ijk}^{id}(\boldsymbol{x},\boldsymbol{\chi};t-\tau)D_k(\boldsymbol{\chi},t) + \sigma_{ij}^{is}(\boldsymbol{x},\boldsymbol{\chi};t-\tau)\phi(\boldsymbol{\chi},t)\right\}d\Gamma(\boldsymbol{\chi})d\tau \quad (2\text{-}31)$$

$$p(\boldsymbol{x},t) = \int_0^t \int_\Gamma \left\{p^{is}(\boldsymbol{x},\chi;t-\tau)\phi(\boldsymbol{\chi},t)\right\}d\Gamma(\boldsymbol{\chi})d\tau \quad (2\text{-}32)$$

where $\boldsymbol{x}$ and $\boldsymbol{\chi}$ are the two-dimensional coordinate vectors. $\sigma_{ij}(\boldsymbol{x},t)$ denotes the stress component at $\boldsymbol{x}$ and time *t*. The influence functions $\sigma_{ijk}^{id}(\boldsymbol{x},\boldsymbol{\chi};t-\tau)$ and $\sigma_{ij}^{is}(\boldsymbol{x},\boldsymbol{\chi};t-\tau)$ represent the stress component due to an instantaneous unit point DD (*id*) and fluid source (*is*), respectively, located at $\boldsymbol{\chi}$ and taking place at τ. Similarly, $p^{is}(\boldsymbol{x},\chi;t-\tau)$ is the pore pressure due to the same instantaneous source. Note also that $D_k(\boldsymbol{\chi},t)$ and $\phi(\boldsymbol{\chi},t)$ are the unknown strengths of the point DD and fluid sources.

For time-dependent normal displacement discontinuity, ΔD_n, shear displacement discontinuity, ΔD_s, and fluid leak-off, ΔQ_l, a time-marching scheme as shown in Figure 2-4 is applied to discretize the time-dependent quantities into M constant steps using the superposition method to account for each step change at the time it occurs. Following Tao and Ghassemi (Tao and Ghassemi 2010), the total induced tractions and pore-pressure on the *ith* fracture segment at time *t* are obtained by summing the influences from all time steps as follow:

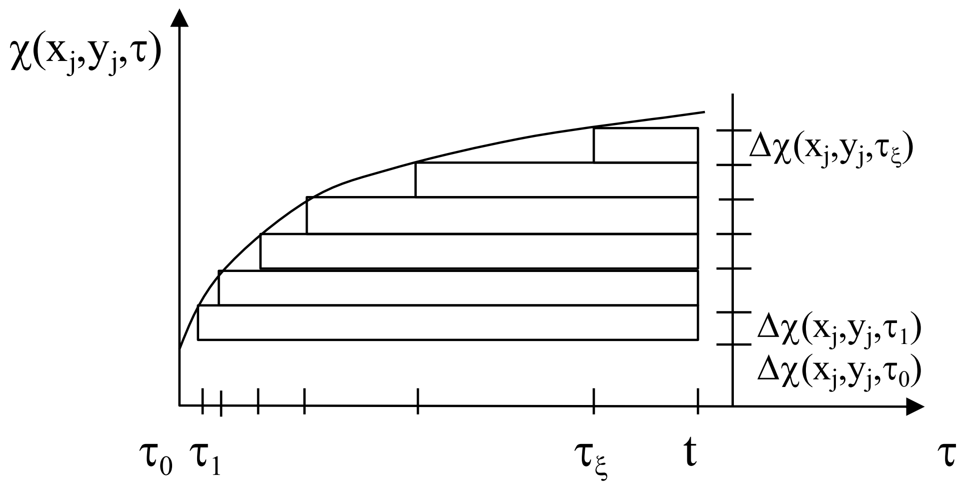

Figure 2-4. Illustration of the time-marching scheme for the changes of a generic source variable $\Delta\chi$.

$$t_s^i(t) = \sum_{h=0}^{M} \left(\sum_{j=1}^{N} A_{ss}^{ij}(t - t_h)\Delta D_s^{jh} + \sum_{j=1}^{N} A_{sn}^{ij}(t - t_h)\Delta D_n^{jh} + \sum_{j=1}^{N} A_{sl}^{ij}(t - t_h)\Delta Q_l^{jh} \right) \tag{2-33}$$

$$t_n^i(t) = \sum_{h=0}^{M} \left(\sum_{j=1}^{N} A_{ns}^{ij}(t - t_h)\Delta D_s^{jh} + \sum_{j=1}^{N} A_{nn}^{ij}(t - t_h)\Delta D_n^{jh} + \sum_{j=1}^{N} A_{nl}^{ij}(t - t_h)\Delta Q_l^{jh} \right) \tag{2-34}$$

$$p^i(t) = \sum_{h=0}^{M} \left(\sum_{j=1}^{N} A_{pl}^{ij}(t - t_h)\Delta Q_l^{jh} \right) \tag{2-35}$$

where h is the time step index and ΔD_s^{jh}, ΔD_n^{jh}, and ΔQ_l^{jh} denote the increments of normal displacement discontinuity, shear displacement discontinuity and fluid leak-off or interface flow rate of the *jth* fracture segment at h. Kernels components such as the $A_{ss}^{ij}(t-t_h)$ are the influence coefficients of jth fracture segment on the ith fracture element at time t_h according to the time-convolution. In this work, the coefficients A_{ss}^{ij}, A_{sn}^{ij}, A_{ns}^{ij}, and A_{nn}^{ij} that account for the influences of the displacements discontinuities over the traction components consider only elastic effects while the coefficients A_{sl}^{ij}, A_{nl}^{ij}, and A_{pl}^{ij} take into account the poroelastic effects of the fluid leak-off over traction and pore-pressure (Curran and Carvalho 1987; Tao et al. 2011; Vandamme and Roegiers 1990).

To account for shear dilation and joint deformation in Eqs. (2-33) and (2-34), the coefficient A_{ss}^{ij} and A_{nn}^{ij} are modified as follow:

$$\begin{aligned} A_{ss}^{ij} &= A_{ss}^{ij} + K_s^i(t-t_h)\Delta D_s^{ih} \\ A_{nn}^{ij} &= A_{nn}^{ij} + K_n^i(t-t_h)\left(\Delta D_n^{ih} + \Delta D_s^{ih}\tan \emptyset_{\mathrm{d}}\right) \end{aligned} \tag{2-36}$$

where $\emptyset_d$ is the dilation angle which account for the increase of joint aperture by shear displacement, and K_n and K_s are the normal and shear joint stiffness. By rearrenging equations (2-33) to (2-35), a more compact representation of the linear system of equations is formed by keeping on the left side the kernel coefficients (A) and unknown variables (Δx) associated with the current time step (Tao and Ghassemi 2010):

$$A_{sk}^{ij}(t-t_h)\Delta x_k^{j\xi} = b_s^i(t) \tag{2-37}$$

$$p^i(t) + A_{nk}^{ij}(t-t_h)\Delta x_k^{j\xi} = b_n^i(t) \tag{2-38}$$

$$-p^i(t) + A_{pl}^{ij}(t-t_h)\Delta x_l^{j\xi} = b_p^i(t) \tag{2-39}$$

where $j = 1, .., N$, and $k = s, n, l$. The right-hand side (b) groups the accumulated effects of variables corresponding to previous time steps and is writeen as follow:

$$b_s^i(t) = -A_{sk}^{ij}(t-t_h)\Delta x_k^{jh} \tag{2-40}$$

$$b_n^i(t) = p_0^i - A_{nk}^{ij}(t-t_h)\Delta x_k^{jh} \tag{2-41}$$

$$b_p^i(t) = -p_0^i - A_{pl}^{ij}(t-t_h)\Delta x_l^{jh} \tag{2-42}$$

where $h = 0, .., \xi - 1$, and Δx_k represents the *kth* unknown variable ΔD_s, ΔD_n, and p. Note that computing b requires the computation of T_h matrix-vector multiplications $O(T_h N^2)$ which exhibit a quadratic complexity according to the number of time steps *h*:

$$T_h = \sum_{k=1}^{h} k = 1 + 2 + 3 + \cdots + h = \frac{h(h+1)}{2} \tag{2-43}$$

For example, if 20 time steps are set for a numerical simulation, the total number of matrix-vector multiplications would be 210. Therefore, our approach will also use the FMM to accelerate the calculation of *b*.

Finally, Eq. (2-24) for the fluid flow through the fracture network represents the last equation that needs to be simultaneously solved along with Eqs. (2-33) to (2-35). Comparing with the previous FED model, it now accounts not only for changes in the fluid density and compressibility but also for the leak-off fluid between the fracture and formation. Here, fracture permeability (k_f) is computed using the cubic law as a function of fracture width (w_f) as:

$$k_f = \frac{w_f^2}{12} \tag{2-44}$$

The final form of Eq. (2-24) after proper discretization in time and space using a convolution scheme is:

$$\sum_{j=1}^{m} C^{ij} p^j(t) - 2a\Delta D_n^{i\xi} + 2a\Delta Q_l^{i\xi} = C^{ii} p^i(t_\xi) - 2a \sum_{h=0}^{\xi-1} \Delta Q_l^{ih} - \sum_{h=0}^{\xi} q_s^{ih} \tag{2-45}$$

Note that in order to solve Eq. (2-45), fluid pressure, displacement discontinuities, fluid leak-off rate as well as production or injection rates need to be set with initial and boundary conditions, respectively.

3. FAST MULTIPOLE METHOD (FMM)

The Fast Multipole Method (FMM) (Greengard and Rokhlin 1987) has been used to reduce the computational complexity of some boundary value problems in terms memory requirements and execution time (Liu 2009; Nishimura et al. 1999; Wang, H. et al. 2005; Wang and Yao 2005; Wang, P. et al. 2005; Wang et al. 2007; Yoshida et al. 2001b). However, its application to other general problems has been limited mainly due to the difficulty of understanding the method and lack of mathematical developments for the fundamental solutions of interest as well as high programming complexity. Recently, a new FMM formulation called "black-box" has been developed which does not require the implementation of multiple expansions of the underlying kernel but only the kernel evaluations (Fong and Darve 2009), opening up a range of potential applications for engineering applications.

This section presents a comprehensive description of the FMM beginning with a brief overview of the method and then showing the mathematical background of both the conventional and kernel-independent versions of the FMM, in particular for the latter the Black-Box FMM (bbFMM) that will be adopted as the building block in our approach.

3.1. Overview

The main idea behind the FMM is to accelerate matrix–vector products (*Ax*) in iterative algorithms without forming the coefficient matrix explicitly which reduces computation time and saves memory (Greengard and Rokhlin 1987; Liu 2009).

Algebraically, the product of the *i-th* row of a *NxN* matrix, *K,* with a column vector, σ, of length *N* can be expressed as follow:

$$f(x_i) = \sum_{j=1}^{N} K(x_i, y_j)\, \sigma_j \tag{3-1}$$

In analogy to Eq. (2-15), the term *f* in Eq. (3-1) may represent a field value evaluated at point x_i due to the influence of sources (governed by the kernel matrix *K*) and located at a set of centers. This computation represents the well-known "N-body problem" and requires *N*x*N* algebraic products or $O(N^2)$ operations to compute the field values at a set of *N* evaluation points, x_i. Therefore, the objective of using FMM is to reduce this calculation to ideally *O(N)* counts by approximating the values of *f*. This approximation is accomplished by classifying the influences into near and far-field interactions according with the distance among field and source points. While the near-field interactions are evaluated as the conventional DDM showing a quadratic complexity, the far-field influences that involve most of the algebraic products are calculated efficiently using FMM to reduce the cost proportional to *N*, *O(N).*

The far-field interactions are approximated by concentrating the influence of a cluster of source particles (or fractures in our case) in a single location by assuming that the influences of such particles become weaker as the distance between field and source locations increases. This procedure requires constructing a hierarchical tree (or quadtree structure in 2D) to decompose and divide the computational domain with increasing level of refinements, identifiying a near and far sub-domains at each level. Based on this space decomposition, Eq. (3-1) can be expressed as (Liu 2009; Morris and Blair 2000; Peirce and Napier 1995):

$$f(x_i) = \sum_{l=1}^{N_{near}} K(x_i, y_l)\,\sigma_l + \sum_{k=1}^{N_{far}} K(x_i, y_k)\,\sigma_k \tag{3-2}$$

where N_{near} and N_{far} represent the number of source points in the near and far-field domains of the summation terms (assuming $N_{near} << N_{far}$) which are computed using the conventional DDM and FMM, respectively. More details and variations of the FMM have been described previously by other authors (Greengard and Rokhlin 1987; Ying et al. 2004).

3.2. Conventional FMM

Consider a general 2D potential problem (e.g., heat conduction, acoustic) governed by the Laplace equation in a circular domain V with boundary S:

$$\nabla^2\phi(x) = 0, \quad \forall x \in V \tag{3-3}$$

under the boundary conditions:

$$\phi(x) = \bar{\phi}(x), \quad \forall x \in S \tag{3-4}$$

where ϕ is the potential.

Using the method of fundamental solutions, for example, and placing N field (x) and source (y) points on the boundary S, (See Figure 3-1), the following system of equations can be formed:

$$\sum_{j=1}^{N} G(x_i, y_j)\mu_j = \bar{\Phi}_i \tag{3-5}$$

with

$$G(x, y) = \frac{1}{2\pi} ln\left(\frac{1}{r}\right) \tag{3-6}$$

Expresssing Eq. (3-6) in complex notation after replacing $\boldsymbol{x}$ and $\boldsymbol{y}$ by z_0 and z, take the form:

$$G(z_0, z) = -\frac{1}{2\pi} ln(z_0 - z) \tag{3-7}$$

where G is the kernel or fundamental solution for potential problems, r is the distance between field and source points, and μ_j is the unknown density at the source points j.

The main idea behind the conventional FMM is to expand the kernel in order to have new approximated expressions where the field (z_0) and source (z) points are separated. For example, by introducing an expansion or “middle” point z_c near z using Taylor series (See Figure 3-1), Eq. (3-7) becomes (Liu et al. 2005):

$$G(z_0, z) = -\frac{1}{2\pi}\left[ln(z_0 - z_c) - \sum_{k=1}^{\infty} \frac{1}{k} \frac{(z - z_c)^2}{(z_0 - z_c)^2}\right] \tag{3-8}$$

Note that in contrast to Eq. (3-7), z_0 and z are separated by z_c in Eq. (3-8). Now, after introducing Eq. (3-8) into the leaf-hand side Eq. (3-5) we have:

$$\sum_{j=1}^{N} G(z_0, z_j)\mu_j = -\frac{1}{2\pi}\left[ln(z_0 - z_c)M_0 - \sum_{k=1}^{\infty} \frac{M_k(z_c)}{(z_0 - z_c)^k}\right] \tag{3-9}$$

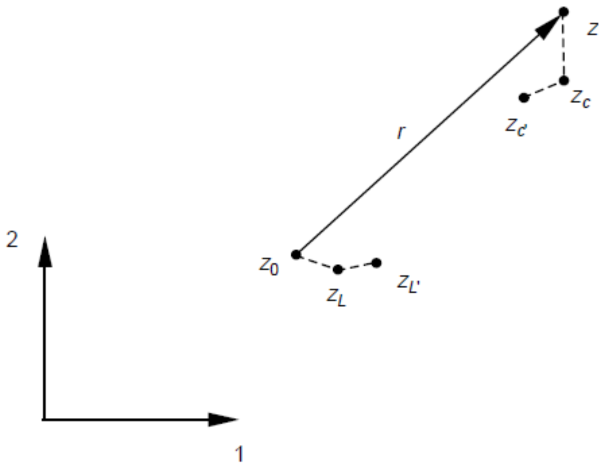

Figure 3-1. Location of expansion points near z_0 and z used in the FMM (Liu et al. 2005).

where the $M_k(z_c)$ are the so called *moments* about z_c which does not depend on z_0:

$$M_k(z_c) = \begin{cases} \sum_j \mu_j & for\ k = 0 \\ -\frac{1}{k}\sum_j \left(z_j - z_c\right)^k \mu_j & for\ k \geq 1 \end{cases} \tag{3-10}$$

Therefore, given a set of values for the unknowns μ_j contained in a cell *c* centered at z_c, these moments are needed to be computed once, and then Eq. (3-9) can be used to evaluate left-hand side of Eq. (3-5) for z_0 far away from z_c.

Additional expansion approximations near z_0 and z points obtained through mathematical manipulation are necessary in the FMM to compute the influence of points z_0 located far away from to z. The *Moment-to-Moment translation* (M2M) is used to translate the effects of moments from points z_c in Eq. (3-10) to a new location $z_{\acute{c}}$, commonly the center of the father cell of cell *c* without recomputing the moments:

$$M_k(z_c) = \begin{cases} M_0(z_c) & for\ k = 0 \\ -\frac{1}{k}\sum_j (z_c - z_{\acute{c}})^k M_0(z_c) & \\ +\sum_{l=1}^{k} \binom{k-1}{l-1} (z_c - z_{\acute{c}})^{k-1} M_l(z_c) & for\ k \geq 1 \end{cases} \tag{3-11}$$

On the other hand, by introducing a new expansion point z_L close to z_0, the so-called *local expansion* is obtained:

$$\sum_j G(z_0, z_j)\mu_j = \sum_{l=0}^{\infty} L_l(z_L)(z_0 - z_L)^l \tag{3-12}$$

where the coefficient are given by the *Multipole-to-Local* (M2L) translation by:

$$L_L(z_L) = \begin{cases} -\frac{1}{2\pi}\left[ln(z_L - z_c)M_0 + \sum_{k=1}^{\infty} \frac{M_k(z_c)}{(z_L - z_c)^k}\right] & for\ l = 0 \\ \frac{1}{-2\pi}\left[\frac{(-1)^{l+1}}{l}\frac{M_0}{(z_L - z_c)^l} + \frac{(-1)^l}{(z_L - z_c)^l}\right. & \\ \left.\sum_{l=1}^{k} \binom{l+k-1}{k-1} \frac{M_k(z_c)}{(z_L - z_c)^k}\right] & for\ l \geq 1 \end{cases} \tag{3-13}$$

Finally, by moving the local expansion point z_L to $z_{\acute{L}}$, a new expression local expansion using *n*-terms is obtained:

$$\sum_j G(z_0, z_j)\mu_j = -\frac{1}{2\pi}\left[ln(z - z_L)M_0 + \sum_{k=1}^{\infty} \frac{M_k(z_L)}{(z - z_L)^2}\right] \tag{3-14}$$

where the new coefficients are called *Local -to-Local* (L2L) translation and are given by:

$$L_l(z_{\acute{L}}) = \sum_{m=1}^{n} \binom{m}{l} (z_{\acute{L}} - z_L)^{m-l} L_m(z_L), \quad for\ l \geq 0 \tag{3-15}$$

Eqs. (3-10), (3-11), (3-13), and (3-15) associated with the moments, M2M, M2L, and L2L represent the building block operations used in the FMM and are key to understand the solution algorithm.

3.2.1. Solution algorithm

This section presents a general algorithm (Liu 2009; Liu et al. 2005) for the far-field calculation in Eq. (3-5) which involves the following four (4) steps: a) Discretization of the boundary, b) Construction of the quad-tree structure of the boundary element, c) Upward pass, and d) Downward pass as described below:

a) Discretization of the boundary: The FMM uses the same discretization of the conventional BEM by dividing the boundary of the problem Γ into several boundary elements of constant length.

b) Construction of quad-tree structure of the boundary elements: Starting from a square (or parent cell of level 0) enclosing all boundary elements, this parent cell is divided into four equal squares (called children cells of level 1) and the process is continued recursively and stopped when the number of boundary elements in a child cell is fewer than a prespecified number (called leaf cell) or alternatively when the specified number of levels of the quad-tree, *l,* is reached. As a result, a data structure is created to determine at each level of partition the distribution of the boundary elements within the cells as well as to classify each cell into near and far categories according to the distance to the field points. This data organization is also useful for storing certain coefficients needed during the following upward and downward operations.

c) Upward pass: This steps involves computing the moments (Liu 2009) on all cells and at all levels and trace the tree structure upward. The moments are used to expand the kernel and separate the source *y* and field *x* points by the introduction of a middle point, y_o. The moment concentrates in this single point, located in the center of the leaf cells, the effects of a cluster of boundary elements enclosed in them ($l=2$) (Figure 3-2). A similar agglomeration process is done at higher levels ($l>2$) for the parent cells by summing the moments on its four children cells and concentrate them at point y_1 through a Moment to Moment translation (M2M).

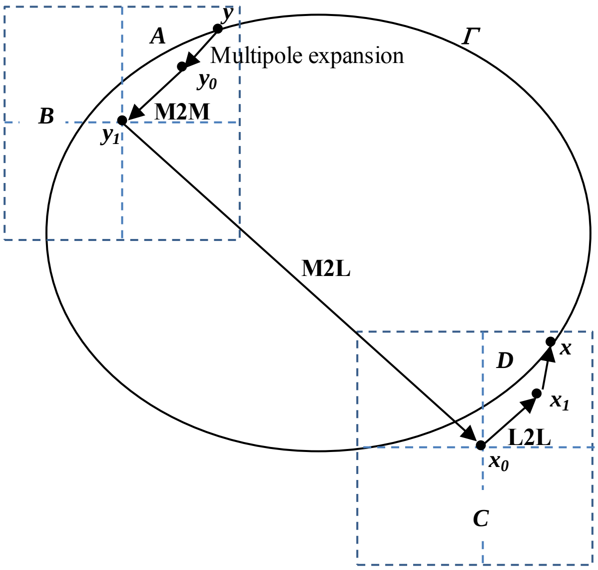

Figure 3-2. Principal operations of the FMM (Wang et al. 2007).

d) Downward pass: In this step the influence of the far source points stored in the cells at different levels (by computing the moments) is finally translated to the field points. This is accomplished by calculating the local expansion coefficients on all cells, starting from level 2 and tracing the tree structure downward to all the leaves. The coefficients associated with a cell D is the sum of the contributions from the Moment to Local translation (M2L) and Local to Local translation (L2L) operations. M2L shifts the cluster effect from y_1 to x_0 and L2L translates it from x_0 to x_1. A local expansion operation (Liu 2009) is used to finally pass the information from point x_1 to the field point x.

Note that the moments as well as the M2M, M2L, and L2L operations are kernel dependent and involve analytical equations. Currently, although there is a solid mathematical development of these operations for selected decaying kernels of the form of Eq. (3-6), complex mathematical derivations (in case of exist) are necessary for new kernels even those of simple form.

3.2. Kernel-Independent FMM (Black-Box FMM)

In contrast with the conventional FMM, the black-box FMM (bbFMM) does not require the implementation of multiple expansions of the kernel using only the kernel evaluations. It shows to be very useful for problems where the kernel is known analytically but is complicated for which analytical expansions might be difficult to obtain. To briefly describe some of the components of bbFMM, let assume a computation similar to that found in Eq. (3-5):

$$\sum_{j=1}^{N} K(r_i, r_j)\sigma_j = \phi_i \tag{3-16}$$

To compute the far-field approximation of the kernels, the Black-Box FMM requires three (3) main steps:

a) Creates a low-rank approximation of the kernel using Chebyshev polynomials:

Assuming a closed interval [-1, 1], any smooth function $f(x)$ can be approximated using:

$$f(x) \approx \sum_{k=1}^{p} w_k(x)\, f(X_k) - \frac{1}{p} \tag{3-17}$$

with

$$w_k(x) = \frac{2}{p}\sum_{m=1}^{p} T_{m-1}(X_k)\, T_{m-1}(x) - \frac{1}{p} \tag{3-18}$$

where $T_m(x)$ is s Chebishev polynomial of order m and X_k are the zeros of $T_p(x)$. Now, let assume that $K(x, y)$ is desired to be approximated in both x and y in the interval. By substituting (3-18) into (3-17), we have:

$$K(x, y) \approx \sum\nolimits_{k,l} w_k(x) w_l(y) K(X_k, X_l) \tag{3-19}$$

Therefore, for two set of N points x_i and y_j, an $O(N)$ method are constructed by first calculating the equivalent charges at node X_l:

$$Q_l = \sum\nolimits_{j=1}^{N} w_l(y_j)\sigma_j \tag{3-20}$$

Next, by computing the potential at Chebyshev node X_k

$$\phi(X_k) = \sum\nolimits_{j=1}^{N} K(X_k, X_l) Q_l \tag{3-21}$$

and finally, the potential at the N nodes x_i

$$\phi_i = \sum\nolimits_{k=1}^{p} w_k(x_i)\phi(X_k) \tag{3-22}$$

In general, the advantage of using a low-rank approximation approach for the FMM is that minimal pre-computing and only requires the ability to evaluate the kernel (K) at several locations avoiding any kernel dependent analytical expansion. In bbFMM, the adoption of Chebyshev polynomials along with their roots as the interpolation nodes serve as the basis to approximate the far-field behavior of a non-oscillatory K. Using Chebyshev nodes ensures the stability of the interpolation scheme providing uniform error distribution across the domain as the number of interpolation nodes (n) become large. Therefore, it allows the specification of fewer nodes for a given accuracy avoiding suffering from the Runge's phenomenon.

b) Build a FMM approach using the approximated kernel:

Once constructed the low-rank approximation of a continuous kernel defined over arbitrary rectangular domains, the M2L operator (described previously) consists in evaluating the field due to source particles located at the n Chebyshev nodes, independent of the N source locations.

c) Accelerate the performance of the M2L operation using Singular Value Decomposition (SVD).

The performance of the M2L which is by far the most expensive operation in FMM is further optimized using SVD by compressing the Chebyshev's interpolation scheme and producing a more compact multipole and local expansion. A more detailed description of bbFMM can be found in (Fong and Darve 2009).

4. FAST MULTIPOLE – DISPLACEMENT DISCONTINUITY METHOD (FM-DDM)

DDM has been extensively applied in mining and hydraulic fracturing (Curran and Carvalho 1987; Tao et al. 2009a; Tao et al. 2009b; Tao and Ghassemi 2010) but it is inefficient when facing large problem sizes. Direct solvers requires $O(N^2)$ memory and $O(N^3)$ to compute the coefficient matrix and solve the system of equations. On the other hand, iterative methods such as the GMRES still need $O(N^2)$ memory but the number of operations to perform a matrix-vector multiplication in k iterations for convergence could be reduced to $O(kN^2)$ in case of well-conditioned systems ($k<<N$). However, realistic representation of most fracture problems of interest that involve a high number of boundary elements are still beyond the current capability of personal computers because matrix-vector products become prohibitive so other methods are necessary to make improvements.

This section presents a new approach called Fast Multipole–Displacement Discontinuity Method (FM-DDM) for the efficient solution of large-scale fracture problems with linear complexity. It combines the DDM and FMM described in Sections 2 and 3, respectively, using for the latter a kernel-independent version of the classical FMM called black-box FMM (bbFMM) based on kernel evaluations where multipole and local expansions are not required. In this section, the FM-DDM is described in terms of its main components for the fast matrix-vector product associated with each geomechanical model, iterative algorithm, and preconditioner. Additional details of the numerical procedure and computational implementation are also presented.

4.1. Description

In general, FMM relies on an iterative strategy in which the large matrix-vector multiplication is accelerated without forming the coefficient matrix explicitly. As described in Section 3, this acceleration is carried out by efficiently calculating the interaction between elements using the same BEM discretization but by recursive operations of a quad-tree structure for computation and storage.

In our approach, the normal and shear tractions caused by geomechanical interactions among all fractures can be expressed mathematically as the sum of near and far-field components:

$$t_i = t_i^{near} + t_i^{far} \quad i = n, s \tag{4-1}$$

where the near-field interactions are evaluated as the conventional DDM (Section 2) showing a quadratic, $O(N^2)$, computational complexity and the far-field influences that involves most of the algebraic products are efficiently calculated using FMM (Section 3) to reduce to $O(N)$ the cost proportional to the number of degrees of freedom (N).

4.1.1. Fast computation of matrix-vector multiplications

The calculation of the traction components via iterative techniques in Eq. (4-1) requires the evaluation of several expensive matrix-vector products (denoted as *mvp*). If the ED or FED models are considered, these operations involve only the effects of displacement discontinuities for the multiplication of the coefficient matrix and solution vector during the iterative search. However, the FPDD model poses a more complex situation by requiring the combined elastic and poroelastic effects due the displacement discontinuities and fluid leak-off for the matrix-vector product of interest and also for the calculation of the right-hand side of the system of equations at very time step.

4.1.2. FMM approach for the ED and FED models

Before using the black-box FMM to solve our geomechanics problem of interest several enhancements have to be done. First, it is necessary to express in a compact representation the product of the displacement discontinuity vector and the matrix kernel governing the influence of an arbitrary source fracture *j* over the stress components in a field location or fracture *i*:

$$\begin{bmatrix} \sigma_{xx}^{i,j} \\ \sigma_{yy}^{i,j} \\ \sigma_{xy}^{i,j} \end{bmatrix} = c \begin{bmatrix} \left(K_{xx,s}\right)^{i,j} & \left(K_{xx,n}\right)^{i,j} \\ \left(K_{yy,s}\right)^{i,j} & \left(K_{yy,n}\right)^{i,j} \\ \left(K_{xy,s}\right)^{i,j} & \left(K_{xy,n}\right)^{i,j} \end{bmatrix} \begin{bmatrix} D_s^j \\ D_n^j \end{bmatrix} \tag{4-2}$$

where *c* is an elastic constant computed by:

$$c = \frac{2G}{4\pi(1-v)} \tag{4-3}$$

Eq. (4-3) can be written for *N* elements as:

$$\qquad \therefore \qquad\qquad ; \tag{4-4}$$

$$_{j=1}$$

The next step is to decompose the matrix-vector product in (4-4) into a sum of two (2) matrix-vector products by each stress component. For instance, σ_{xx} is expressed as:

$$\sigma_{xx}^{i} = \sum_{j=1}^{N} K_{xx,s}^{i,j}\, D_s^j + \sum_{j=1}^{N} K_{xx,n}^{i,j}\, D_n^j \tag{4-5}$$

with

$$K_{xx,s}^{i,j} = F_4 + \left(F_4 + F_6\bar{y}^i\right)cos2\beta_j + (F_5 - F_7\bar{y}^i)sin2\beta_j \tag{4-6}$$

$$K_{xx,n}^{i,j} = -F_5 + F_7\bar{y}^i cos2\beta_j + F_6\bar{y}^i sin2\beta_j \tag{4-7}$$

where β_j is the angle of the fracture *j*. After substituting Eqs. (4-6) and (4-7) into Eq. (4-5), σ_{xx} could now be computed using six (6) matrix-vector products:

$$\begin{aligned}\sigma_{xx}^{i} = {} & \sum_{j=1}^{N}(F_4)q_1^j + \sum_{j=1}^{N}\left(F_4 + F_6\bar{y}^i\right)q_2^j + \sum_{j=1}^{N}\left(F_5 - F_7\bar{y}^i\right)q_3^j - \sum_{j=1}^{N}(F_5)q_4^j + \sum_{i=0}^{n}\left(F_7\bar{y}^i\right)q_5^j \\ & + \sum_{j=1}^{N}\left(F_6\bar{y}^i\right) q_6^j\end{aligned} \tag{4-8}$$

with

$$q_1^j = D_s^j \tag{4-9}$$

$$q_2^j = cos2\beta_j D_s^j \tag{4-10}$$

$$q_3^j = sin2\beta_j D_s^j \tag{4-11}$$

$$q_4^j = D_n^j \tag{4-12}$$

$$q_5^j = cos2\beta_j D_n^j \tag{4-13}$$

$$q_6^j = sin2\beta_j D_n^j \tag{4-14}$$

where q_1^j, q_2^j, q_3^j, q_4^j, q_5^j and q_5^j are vectors grouping unknown variables (e.g., D_s^j, D_n^j), fracture parameters (β_j) and even rock properties (for heterogeneous cases) associated exclusively with the source locations j. Note that functions F_4 to F_7 in Eqs. (2-11) to (2-14) are expected to be evaluated at the field position and require proper angular transformations from the global (x, y) to the local $(\bar{x}, \bar{y})$ coordinate system using Eq. (4-15):

$$\begin{bmatrix} \bar{x}^i \\ \bar{y}^i \end{bmatrix} = \begin{bmatrix} \cos\beta_j & \sin\beta_j \\ -\sin\beta_j & \cos\beta_j \end{bmatrix} \begin{bmatrix} (x^i - x^j) \\ (y^i - y^j) \end{bmatrix} \tag{4-15}$$

It should be noted at this point that computing σ_{xx} with Eq. (4-8) using the kernels enclosed by parentheses follows the form of Eq. (3-1). However, additional analytical modifications are required to express such kernels as a function of global coordinate (x,y) as imposed by any FMM algorithm including the bbFMM. It means the presence of β_j inside F_4 to F_7 need to be factored and grouped outside in the vector of unknowns. Following Morris and Blair (Morris and Blair 2000), it can be shown that the influence functions in Eqs. (2-11) to (2-14) can be approximated for large distances as dependent only on global coordinates using the Chain rule:

$$F_4(\bar{x}, \bar{y}) \approx cos2\beta_j F_4(x, y) - sin2\beta_j F_5(x, y) \tag{4-16}$$

$$F_5(\bar{x}, \bar{y}) \approx sin2\beta_j F_4(x, y) + cos2\beta_j F_5(x, y) \tag{4-17}$$

$$F_6(\bar{x}, \bar{y}) \approx cos3\beta_j F_6(x, y) + sin3\beta_j F_7(x, y) \tag{4-18}$$

$$F_7(\bar{x}, \bar{y}) \approx -sin3\beta_j F_6(x, y) + cos3\beta_j F_7(x, y) \tag{4-19}$$

After substituting Eqs. (4-16) to (4-19) into Eq. (4-8) the number of kernels and pseudo-charges will increase. Finally for compacness, the traction components can be represented mathematically as:

$$\sigma_q^i = c \sum_{m=1}^{mvp_{q,p}} \left(\sum_{j=1}^{N} K_m^{i,j} Q_m^j \right) \therefore q = xx, yy, xy\ ;\ p = s, n;\ i = 1,2,.,N \qquad (4\text{-}20)$$

where the subscripts q and p represent the directions of tractions and displacement discontinuities components, and K_m and Q_m are the kernel matrix and vector associated to the *m-th* matrix-vector product of $mvp_{q,p}$. Initially, the total number of mvp required for q and p directions are 26 in total. However, as many K_m and Q_m are repeated only 10 unique FMM approximations with 16 different pseudo charges are needed. Appendix A presents the corresponding analytical expressions of those kernels used by bbFMM to evaluate the three stress components $(\sigma_{xx}, \sigma_{yy}, \sigma_{xy})$. As a final step in the calculation, a post-processing stage to rotate the stress components to the normal and shear directions is performed using Eqs. (2-17) and (2-18).

The description above for the computation of the traction components due to the far-field effect of displacement discontinuities applied for both the ED and FED models. For the latter, no additional multipole approximations are needed for the fluid flow equation as it is evaluated within the near-field computation.

4.1.3. FMM approach for the FPDD model

This model incorporates elastic and poroelastic effects to solve for simultaneous changes of the normal (n) and shear (s) displacement discontinuities, fluid leak-off rate and pore-pressure. In a compact form, the far-field of the tractions due to poroelastic rocks is expressed as the sum of several matrix-vector products (*mvp*) as:

$$t_q^i = c\left(K_m^{i,j} Q_m^j\right) \tag{4-21}$$

where $q = xx, yy, xy$, and $m = 1, ., mvp_q^k$. Note that Eq. (4-21) follows the form of Eq. (3-1) in order to apply the FMM approximation and accounts also for the influence of the fluid leak-off rate (Q_l) over the tractions components (*xx*, *yy*, and *xy*) and the pore pressure (*p*). In addition, to reduce the number of multipole approximations of our FMM approach, the poroelastic kernels that relate the stress components and displacements discontinuities are replaced by their elastic versions of the ED and FED models.

To satisfy Eq. (3-1), the mathematical expressions of the new kernels associated with the fluid leak-off rate and pore pressure need to be simplified (See Appendix B). Final forms of these four (4) kernels for the far-field effects in the local $\bar{x}$, $\bar{y}$ co-ordinate system of the fracture but in terms of *x* and *y* at global coordinates are presented below:

$$\sigma_{\overline{xx}}^{Q_l} \approx -8dM_1 Sin2\beta - 4dM_2 Cos2\beta \tag{4-22}$$

$$\sigma_{\overline{yy}}^{Q_l} = -\sigma_{\overline{xx}}^{Q_l} \tag{4-23}$$

$$\sigma_{\overline{xy}}^{Q_l} \approx -8dM_1 Cos2\beta + 4dM_2 Sin2\beta \tag{4-24}$$

$$P^{Q_l} \approx 2a.\, \mathrm{E}_1[\xi(x, y, 0)^2] \tag{4-25}$$

with

$$\mathrm{E}_1[\xi(x, y, x')^2] \approx 4ct(M_3 + 4ctM_4) \tag{4-26}$$

$$\xi(x, y, x' = a) = \frac{r}{2\sqrt{c.t}} = \frac{\sqrt{(x-a)^2 + y^2}}{2\sqrt{c.t}} \tag{4-27}$$

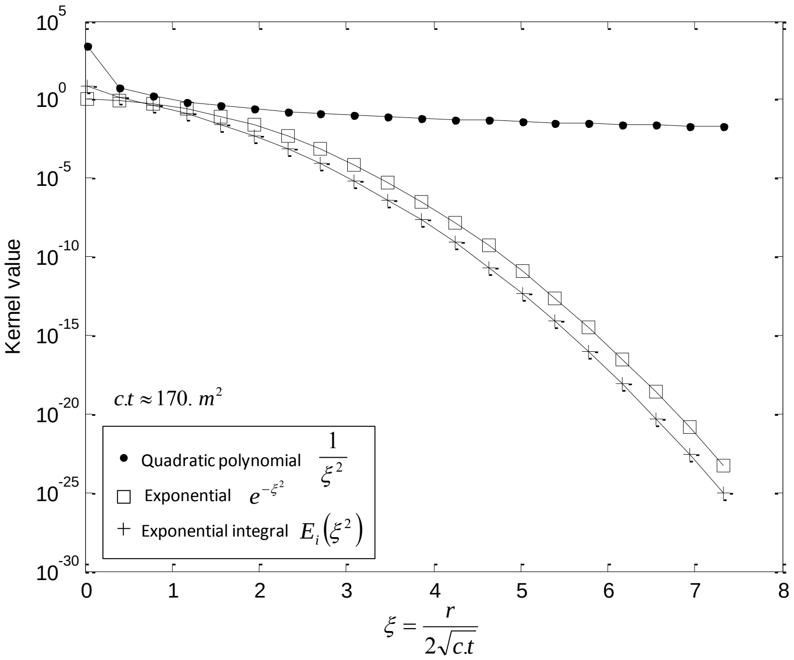

Figure 4-1. Far-field behaviour comparison of the polynomial, exponential, and exponential integral kernels. Note how the polynomial one exhibits the lowest decay with distance.

Mathematical expressions for the additional kernels M_1 to M_4 and related poroelastic parameters (c, M), and constants (d) can be found in Appendix C.

Note that kernels σ_{xx}^{Ql}, σ_{yy}^{Ql}, σ_{xy}^{Ql} in Eqs. (4-22) to (4-24) were simplified from their original forms by keeping only the quadratic polynomial components in the corresponding Eqs. (A1) to (A3) and by neglecting exponential and exponential integrals terms which exhibit a relative faster decay with distance as shown in Figure 4-1.

On the other hand, the far-field of the pore-pressure, which involves only a single integral of exponential integral function, was transformed by first changing the analytical integration with a numerical approximation using the midpoint rule and then by replacing the function with an asymptotic expansion (Press 1992) where only the first two terms were taken into account.

For more details, Appendix B shows the procedure to integrate and rotate elastic and poroelastic kernels of the tractions components from the $\bar{x}$, $\bar{y}$ local to the x, y global coordinate of the j-th fracture element. As a final step, the above traction components have to be computed to the shear and normal directions of the i-th fracture using common stress transformation equations.

4.2. Iterative algorithm and preconditioner

FM-DDM uses the Generalized Minimal RESidual method (usually abbreviated GMRES) as the iterative strategy along with a preconditioner to solve the linear system of equations.

4.2.1. Iterative algorithm GMRES

The GMRES is an iterative method for the numerical solution of a nonsymmetric system of linear equations (Ayachour 2003). The method approximates the solution by the vector in a Krylov subspace with minimal residual. The Arnoldi iteration is used to find this vector. Denote the Euclidean norm of any vector v by $||v||$. Denote the system of linear equations to be solved by:

$$Ax = b \tag{4-26}$$

where the matrix A is assumed to be invertible of size m-by-m. Furthermore, it is assumed that b is normalized, i.e., that $||b|| = 1$. The nth Krylov subspace for this problem is:

$$K_n = K_n(A, b) = span\{b, Ab, A^2b, \ldots, A^{n-1}b\} \tag{4-27}$$

This algorithm approximates the exact solution of $Ax = b$ by the vector $x_n \in K_n$ that minimizes the Euclidean norm of the residual $Ax_n - b$. The vectors b, Ab, …, $A^{n-1}b$ might be almost linearly dependent, so instead of this basis, the Arnoldi iteration is used to find orthonormal vectors $q_1, q_2, \ldots., q_n$ which form a basis for Kn. Hence, the vector $x_n \in K_n$ can be written as $x_n = Q_n y_n$ with $y_n \in R^n$, where Q_n is the m-by-n matrix formed by $q1, \ldots, qn$.

The Arnoldi process also produces an $(n+1)$-by-n upper Hessenberg matrix $\widetilde{H}_n$ with

$$AQ_n = Q_{n+1}\widetilde{H}_n \tag{4-28}$$

Because Q_n is orthogonal, we have

$$\|Ax_n - b\| = \left\|\widetilde{H}_n\, y_n - \beta e_1\right\| \tag{4-29}$$

where $e_1 = (1,0,0, \ldots ,0)$ is the first vector in the standard basis of R^{n+1}, and

$$\beta = \|b - Ax_0\| \tag{4-30}$$

x_0 being the first trial vector (usually zero). Hence, x_n can be found by minimizing the Euclidean norm of the residual:

$$r_n = \left\|\widetilde{H}_n\, y_n - \beta e_1\right\| \tag{4-31}$$

This is a linear least squares problem of size n. This yields the GMRES method. At every step of the iteration:

1. do one step of the Arnoldi method.
2. find the y_n which minimizes $||r_n||$.
3. compute $x_n = Q_n y_n$.
4. repeat if the residual is not yet small enough.

At every iteration, a matrix-vector product Aq_n must be computed. This costs about $2m^2$ floating-point operations for general dense matrices of size m. In addition to the matrix-vector product, $O(nxm)$ floating-point operations must be computed at the *nth* iteration.

4.2.2. Preconditioning

Preconditioning transforms the original linear system $Ax = b$ into an equivalent one which is easier to solve by an iterative technique. A good preconditioner M is an approximation for A which can be efficiently inverted, chosen in a way that using $M^{-1}A$ or AM^{-1} instead of A leads to a better convergence behavior (Liu 2009).

GMRES is rarely used directly. In practice, they are always applied in combination with some preconditioner. Note that, whereas GMRES is a general purpose technique, the preconditioner typically incorporates information about the specific problem under consideration. Two (2) types of preconditioning could be used in this work: left and right preconditioners:

– Left preconditioning:

$$M^{-1}Ax = M^{-1}b \tag{4-32}$$

– Right preconditioning:

$$AM^{-1}u = b \tag{4-33}$$

with

$$x = M^{-1}u \tag{4-34}$$

where the latter involves a substitution *u* for the original variable *x*.

The matrix M is chosen in such a way that the spectral properties of $M^{-1}A$ are better than those of A and, at the same time, the inverse of M is not expensive to compute. The Jacobi preconditioner (also known as diagonal scaling), is the simplest of other known approaches and consists of diagonal elements of the original coefficient matrix which are easy to calculate and implement. Of the same family, the block-diagonal or block Jacobi preconditioner is more accurate and uses the sub-matrices along the diagonal, inverting M through the Gauss-elimination method. More specifically, given a coefficient matrix *A* in a block form:

$$A = \begin{bmatrix} A_{1,1} & A_{1,2} & \cdot & A_{1,k} \\ A_{2,1} & A_{2,2} & \cdot & A_{2,k} \\ \cdot & \cdot & \cdot & \cdot \\ A_{k,1} & A_{k,2} & \cdot & A_{k,k} \end{bmatrix} \tag{4-35}$$

a preconditioner could be chosen so that

$$M_J^{-1} = \begin{bmatrix} A_{1,1}^{-1} & & & \\ & A_{2,2}^{-1} & & \\ & & \cdot & \\ & & & A_{k,k}^{-1} \end{bmatrix} \tag{4-36}$$

Here, of course, we assume that the diagonal blocks $A_{i,i}$ are cheaply invertible.

4.3. Solution algorithm

This section will describe the numerical procedure associated with the solution of FPDD model as it represents the most general geomechanical case. Eqs. (2-25), (2-26), (2-27), and (2-35) are solved iteratively using a scaling and diagonal-block preconditioned GMRES following the next steps. Initially, the input data of the fracture network associated with geometry, discretization, element connectivity, rock and fluid properties, multipole, solver parameters as well as initial and boundary conditions are set. Then, the quad-tree structure of the boundary elements, multipole approximations of the kernels are constructed in a pre-processing stage along with the preconditioning data. Next, the time loop of the simulation begins and for a given a time step, the right-hand side vector is initially computed. Then, the multiplication between the coefficient matrix and the solution guess at the k^{th} iteration is carried out efficiently using the FMM approach. For the problem of interest, the unknowns are the changes of the displacement discontinuities ΔD_s^k and ΔD_n^k, fluid pore-pressure p^k, and fluid leak-off rate ΔQ_l^k at each time step. The residual vector is obtained after assembling near and far-field approximations using the conventional poroelastic DDM and FMM, respectively. When convergence is achieved, the unknown variables associated with stresses, fracture geometry and permeability are updated and the simulation for the next time step is initiated. The above procedure is repeated for the remaining time steps followed by the evaluation of accuracy and computational performance.

4.4. Computational implementation

FM-DDM was implemented in C language using NetBeans Platform on Linux. All cases were run in a Notebook PC with modest computational resources (2.0 GHz Intel Core 2 Duo T5750 Processor with 4GB of RAM). Access to the BLAS/LAPACK libraries in Fortran 77 is also needed during the computation. These libraries are available from Netlib (http://www.netlib.org/). Double precision is used to represent floating-point numbers. Our approach uses a preconditioned GMRES to solve iteratively the system of linear equations (Wang, H. et al. 2005). In this work, the scaling and block-diagonal preconditioner were chosen and coupled with GMRES to reduce the condition number and then the number of iterations.

5. VERIFICATION OF GEOMECHANICAL MODELS AND COMPUTATIONAL PERFORMANCE EVALUATION

During the last two decades FMM have been used to improve the performance of some large-scale boundary-value problems in terms of memory requirements and CPU time showing linear complexity. However, FMM has not been extensively applied in combination with the DDM mainly because of the difficulty of understanding the method and lack of mathematical developments for the fundamental solutions of interest as well as high programming complexity.

This section presents several cases studies to evaluate accuracy and computational performances of the FM-DDM on those numerical models described in Section 2. These models are associated with geomechanical conditions of increasing complexity involving elastic deformation (ED), flow-elastic deformation (FED), and flow-poroelastic deformation and diffusion (FPDD). The results using FM-DDM show an excellent agreement with both analytical and numerical solutions under well-known fracture configurations with a linear complexity in both memory and execution time, outperforming the conventional DDM that demands quadratic and cubic requirements. Problems sizes with up to two hundred thousand of DOFs were successfully evaluated using the proposed approach.

5.1. Model verification

5.1.1. ED model verification – Case 1

FM-DDM was verified comparing its predictions with an analytical solution for the problem of a single pressurized crack in a homogeneous and isotropic rock. As shown in Figure 5-1, the situation of interest involves a single pressurized line fracture of length *2a* embedded in an infinite 2-D elastic rock.

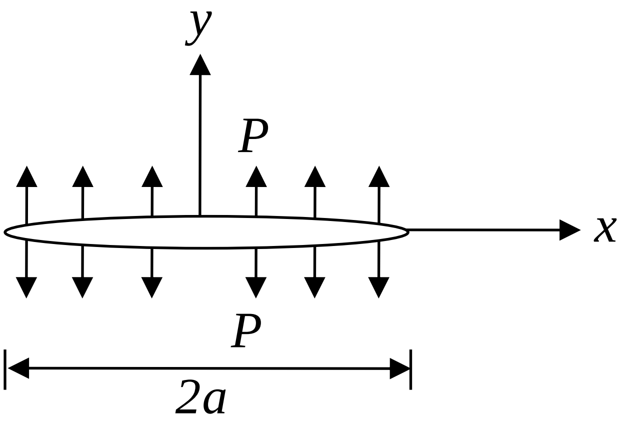

Figure 5-1. A pressurized single crack in an infinite domain configuration used to verify FM-DDM – Case 1.

The fracture is centered at the origin of the coordinate system and oriented along the *x*-direction. An analytical approximation for the normal displacement discontinuity (D_n) is available from the elastic theory as follow (Crouch 1984):

$$D_n(x) = -\frac{(1-v)}{G} p\sqrt{b^2 - x^2} \tag{5-1}$$

Table 5-1. Data set used in ED model verification – Case 1.

Parameter	Value
Domain length, L (m)	400
Shear modulus, G (GPa)	15
Poisson's ratio, v (-)	0.1
Initial normal stiffness, K_{ni} (GPa/m)	30
Shear joint stiffness, K_s (GPa/m)	15
Initial fracture aperture, D_n^0 (m)	$3\text{x}10^{-3}$
Maximum fracture closure, D_{nmax}, (m)	$3\text{x}10^{-3}$
Initial field stress in xx direction, σ_{xx}^{∞} (MPa)	30
Initial field stress in yy direction, σ_{yy}^{∞}(MPa)	30
Initial field stress in xy direction, σ_{xy}^{∞}(MPa)	0
Fluid pressure, p (MPa)	25
Number of chebyshev nodes per dimension, n (-)	5

Table 5-1 presents common rock and fluid properties as well as FMM parameters. Other parameters associated with the iterative algorithm such as tolerance of convergence, Krylov subspace dimension, and maximum number of restart of the Krylov iteration are $3\text{x}10^{-5}$, 50, and 10, respectively.

In the numerical analysis, the fracture is divided into 1000 elements of uniform length. Then the fracture opening of every segment is solved and compared with analytical values. From Figure 5-2 it is clear that the numerical results agree well with the analytical solution showing a maximum relative error less than 0.03%.

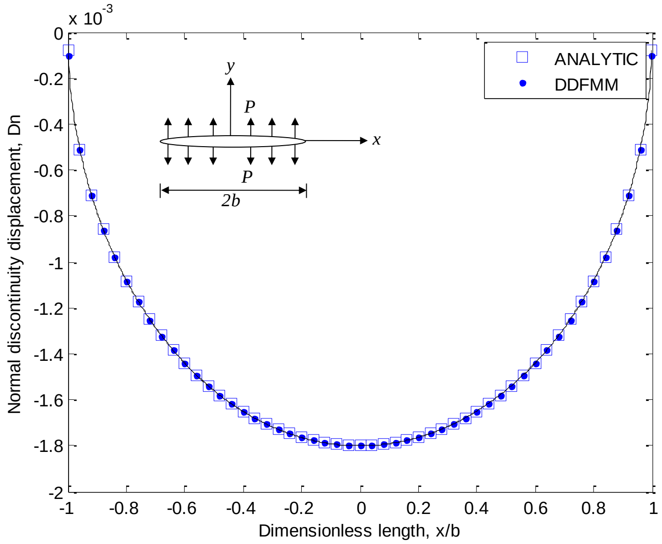

Figure 5-2. Comparison of the fracture opening between FM-DDM and the analytical solution of the pressurized crack problem for different discretizations – Case 1.

Once satisfied this initial verification stage, FM-DDM was then used to compute high definition distributions of normal stress for well-known fracture problems (See Figures 5-3 and 5-4). For both cases, 1000 source elements with 10,000 field points were employed for the visualization whose results agree with those provided by widely used numerical tools (TWODD) (Crouch 1984) and reported in the literature (Behnia et al. 2011, 2012).

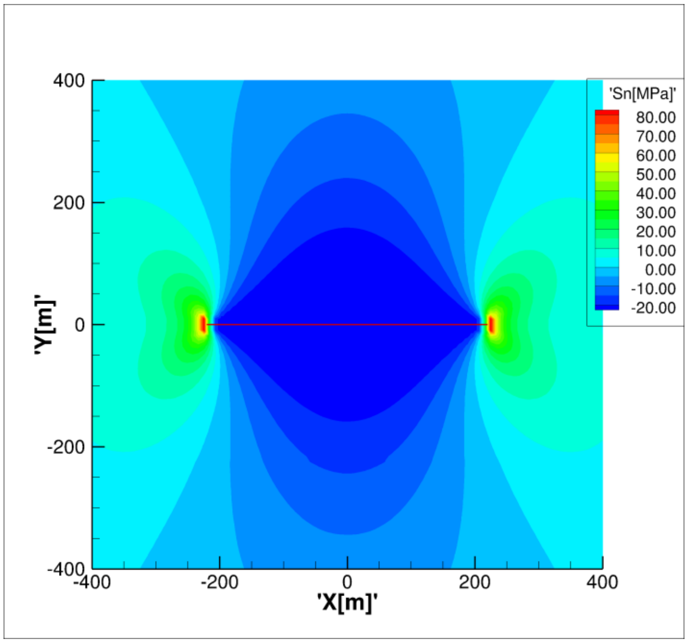

Figure 5-3. High quality normal stress distribution around a pressurized fracture computed with FMM. 1,000 source elements with 10,000 field points were used for the visualization – Case 1.

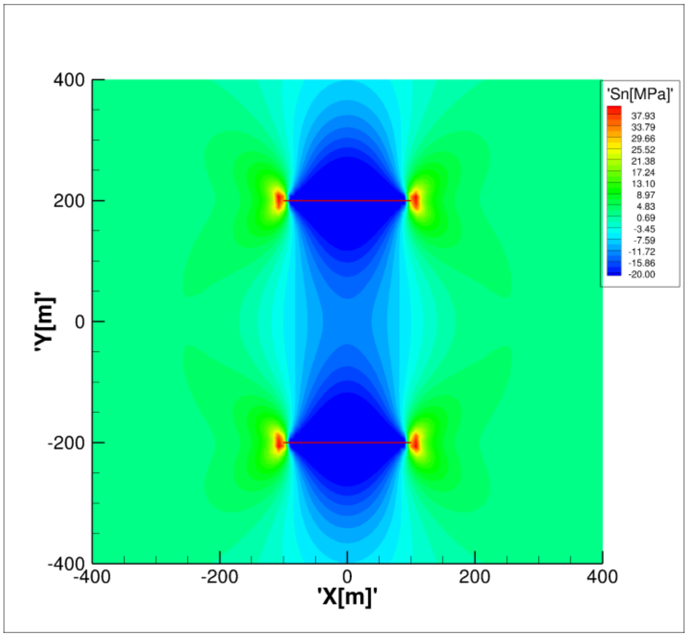

Figure 5-4. High quality normal stress distribution around two parallel horizontal fractures computed with FMM. Equal number of sources and field points of Case 1(a) were used – Case 1.

5.1.2. FED model verification – Case 2

In this case study, a linear fracture embedded in an elastic rock and subjected to injection and production at both ends is considered (See Figure 5-5). As transient analytical solutions to predict simultaneous changes of both displacement discontinuities and fluid pressure are not available, this work proposed to conduct the verification process by inspecting residual values of the traction and diffusion equations described previously. A residual tolerance of 1x10-3 has been set as a threshold for comparison purposes. Additional qualitatively verifications will be carried out by analyzing some expected patterns of the dynamic pressure and displacements responses to ensure the numerical solution obeys the physical processes. Most of the attention will be focused on the pressure computation because the normal and shear displacement discontinuities were previously verified using an analytical solution. Table 5-1 presents rock and fluid properties, FMM parameters as well as production and injection data.

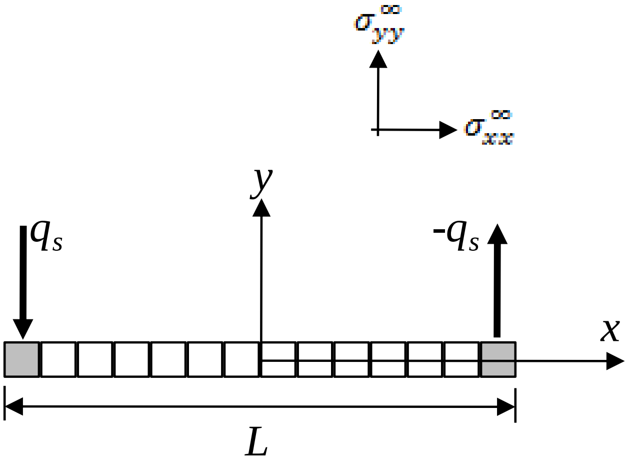

Figure 5-5. Linear fracture configuration subjected to fluid injection and production used to verify the FED model – Case 2.

Table 5-2. Data set used in the FED model verification – Case 2.

Parameter	Value
Domain length, L, (m)	400
Shear modulus, G, (GPa)	15
Poisson's ratio, v, (-)	0.1
Shear joint stiffness, K_s (GPa/m)	7.5
Initial normal stiffness, K_{ni}, (GPa/m)	15.0
Maximum fracture closure, D_{nmax}, (m)	$5\text{x}10^{-4}$
Far-field stress in *xx* direction, σ_{xx}^{∞} , (MPa)	15.1
Far-field stress in *yy* direction, σ_{yy}^{∞}, (MPa)	15.1
Far-field stress in *xy* direction, σ_{xy}^{∞}, (MPa)	0
Initial fracture aperture, D_n^0, (m)	$5\text{x}10^{-4}$
Initial shear displacement, D_s^0, (m)	0
Initial fluid pressure, p, (MPa)	15
Fluid compressibility, c_f, (1/MPa)	$5\text{x}10^{-5}$
Fluid viscosity, μ_f, (MPa.s)	$5\text{x}10^{-9}$
Total injection or production rate, q_s, (m^3/s)	$2.16\text{x}10^{-4}$
Total simulation time, t_s, (s)	$1\text{x}10^{6}$
Number of time steps, *ndt*, (-)	30
Number of chebyshev nodes per dimension, n, (-)	5

For this case the fracture length is divided in 400 boundary elements. Figure 5-6 presents the residual mean squared error of the equations for each time step while Figure 5-7 shows the transient response of pressure and displacements at both wells with respect to their initial values. Values above (below) zero correspond to the injector (producer) well. Observe that the residual errors are significatively smaller than the prescribed tolerance during all the simulation, with a maximum value of 10^{-4} for the pressure. On the other hand, it is clear from Fig. 4 that the solution response at both wells shows as expected: i) symmetry pressure pattern respect to the initial value, ii) steady state behavior at late time, iii) null shear displacements, and iv) maximum (minimum) normal displacement discontinuity at the injector (producer) which indicate the numerical solution is qualitatively correct.

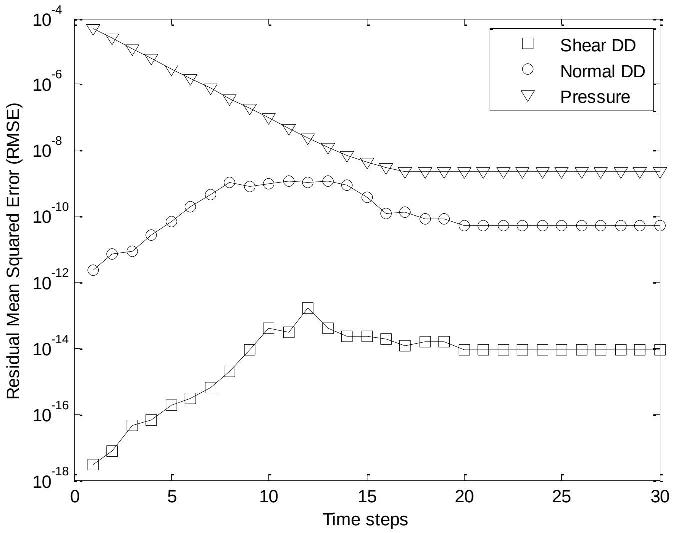

Figure 5-6. Mean values of the residual equations for each time step – Case 2.

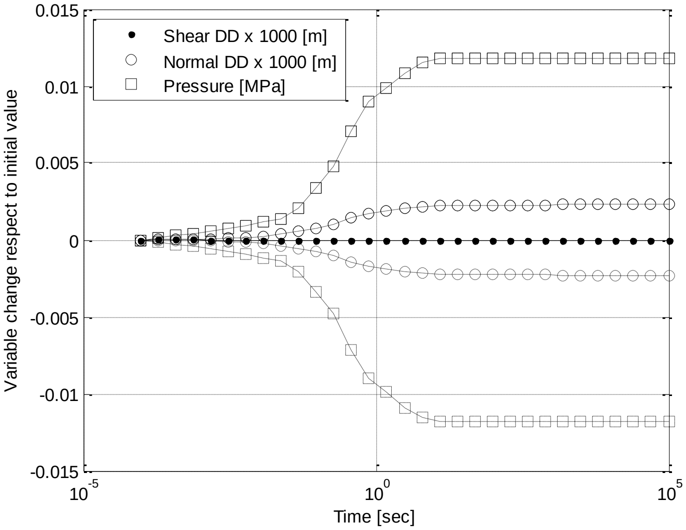

Figure 5-7. Transient response of pressure and displacements at the injector and producer wells – Case 2.

5.1.3. FPDD model verification – Case 3

The elastic version of this model was verified in the previous section. Now, the poroelastic model is tested here using again the problem of a pressurized crack (Figure 5-1). The crack is suddenly and uniformly pressurized. Under a one-way coupling scenario, the fracture response (aperture) is a sum of the aperture under elastic loading and a closure caused by the stressed induced by pore pressure diffusion (Curran and Carvalho 1987; Tao et al. 2011; Vandamme and Roegiers 1990; Zhou and Ghassemi 2011). The input for the problem is from [3] and the element and time are divided into forty (40) elements and time steps. Figure 5-8 shows the response of the fracture (at its center) under a pore pressure or Mode 2 loading. As expected the impact of pore pressure is negligible at zero plus time and gradually increases as the fluid diffuses into the rock matrix causing it to dilate and hence lead to a fracture closure.

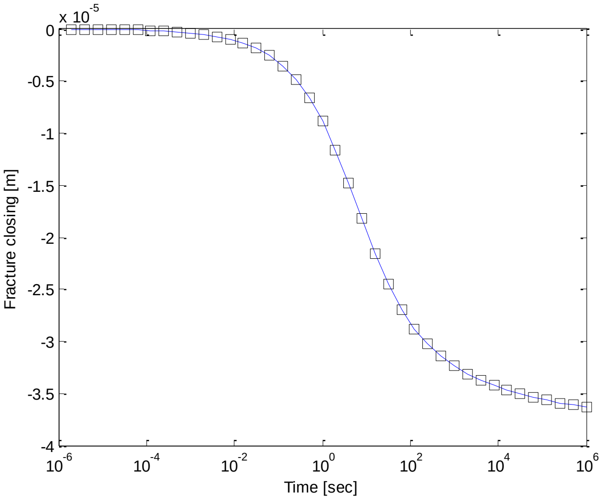

Figure 5-8. Fracture response to Mode II or pore pressure loading. The fracture tends to close under this loading mode – Case 3.

The result predicted by the model is in good agreement with those in (Tao et al. 2011; Vandamme and Roegiers 1990). Figure 5-9 shows the maximum fracture aperture (at its center) under combined Mode I and II loading. Mode I is assumed elastic in this study and occurs instantaneously. The fracture opening gradually decreases with time under the action of pore pressure diffusion.

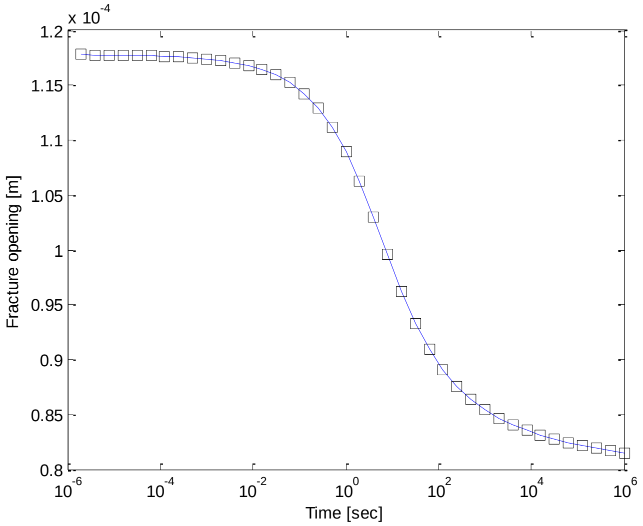

Figure 5-9. Fracture response under elastic and pore pressure loading. Pore pressure diffusion makes the aperture response time dependent – Case 3.

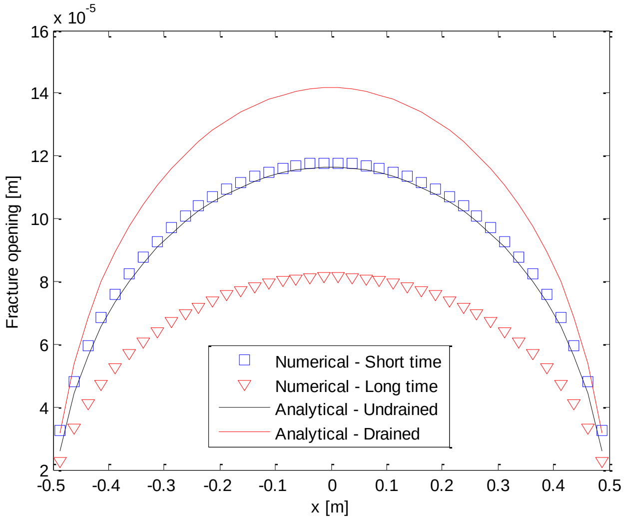

Figure 5-10. Fracture profile for different times representing drained and undrained conditions – Case 3.

In Figure 5-10, the facture opening profile is shown for small and large time. The profile is elliptical and again, the opening is smaller at larger time in agreement with the results in (Tao et al. 2011).

An additional verification step is presented by comparing the results of FM-DDM with a well-known analytical solution of uniform flux in a vertical fracture for the specific case of constant width by ignoring geomechanical effects. Figure 5-11 presents the comparison between the wellbore and dimensionless pressure of both FM-DDM and the analytical solution for uniform flux in fractures.

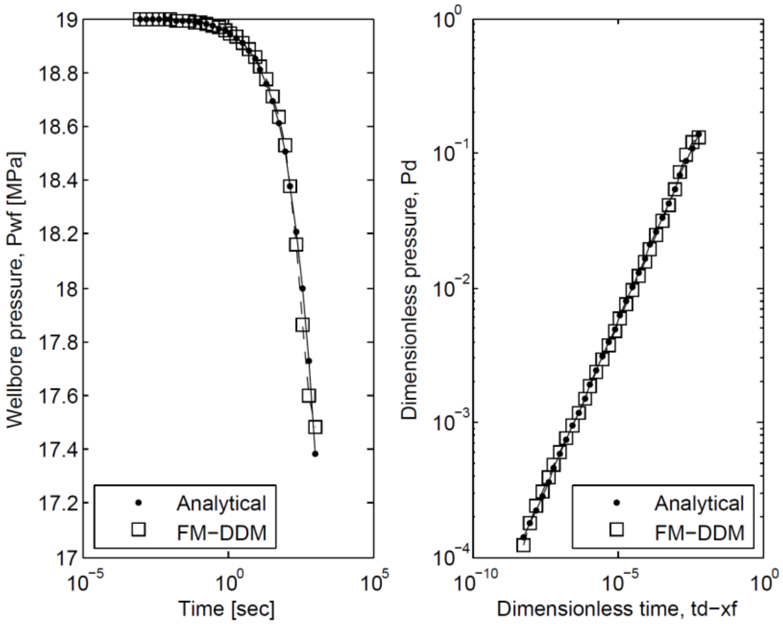

Figure 5-11. Comparison between the wellbore pressure (left) and dimensionless pressure (right) computed with FM-DDM and the analytical solution for uniform flux in a vertical fracture – Case 3.

Similar to Fig. 5-5, a linear fracture is considered but the producer well is located in the center of the linear fracture and no injection is assumed allowing the reservoir fluid comes into the fracture. Note that only the linear flow behavior of the analytical solution at the early time of the response will be used here for comparison purposes. Therefore, our geomechanical model which account for one dimensional flow sustained mainly by expansion of fluids in front of the fracture faces could be used. For dimensionless time ($t_{D_{xf}}$) less than 0.16, the full analytical solution for the dimensionless pressure (P_D) can be reduced during this regime to (Cinco-Ley and Samaniego-V. 1981):

$$P_D = \sqrt{\pi t_{D_{xf}}} \tag{5-1}$$

with

$$P_D = \frac{2\pi kh\left(P_i - P_f\right)}{q\mu} \quad and \quad t_{D_{xf}} = \frac{kt}{\phi\mu c_t x_f^2} \tag{5-2}$$

where P_i and P_f are the initial and flowing wellbore pressure, t is the time, x_f is the fracture length and h is the formation thickness. The results of the comparison show in general a good agreement in both the flowing wellbore pressure (Fig. 5-11 - Left) with an average error of 0.2%, and the dimensionless pressure (Fig. 8 - Right) where the usual half slope on the log-log plot associated with the linear flow regime is observed.

5.2. Computational performance evaluation

This evaluation process involves solving geomechanical problems of increasing number of fractures (e.g., 10,000, 20,000, 50,000) and then registers and compares the corresponding memory and time requirements for both the conventional DDM and the FM-DDM. For all case studies, an orthogonal fracture network is assumed so that the number of fracture segments and corresponding constant length are determined after given the fracture spacing. Therefore, fracture networks generated with different fracture spacing correspond to different geometries and their results cannot be compared even though with the same reservoir dimension.

5.2.1. ED model evaluation – Case 4

Figure 5-12 shows the largest fracture network discretized into 100,000 fractures of 0.42m (or 200,000 DOFs as every element has associated two unknowns). As shown in the enlarged zone, the network consists of orthogonal fractures whose elements are chosen randomly. The spacing between the fractures is equal to the fracture element size. The network is subjected to a constant fluid pressure that is lower than the far-field stress so that the fracture elements behave as joints. The input data is showed in Table 5-1.

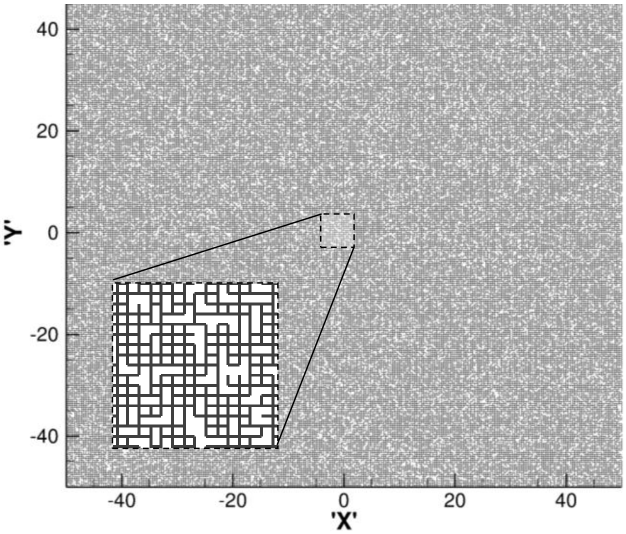

Figure 5-12. Fracture network of 100,000 boundary elements used to evaluate the performance of FM-DDM – Case 4.

Figures 5-13 and 5-14 show the CPU time and the percent of RAM memory used by DDM and FM-DDM to solve geomechanic models of increasing number of degrees of freedom (DOF), respectively.

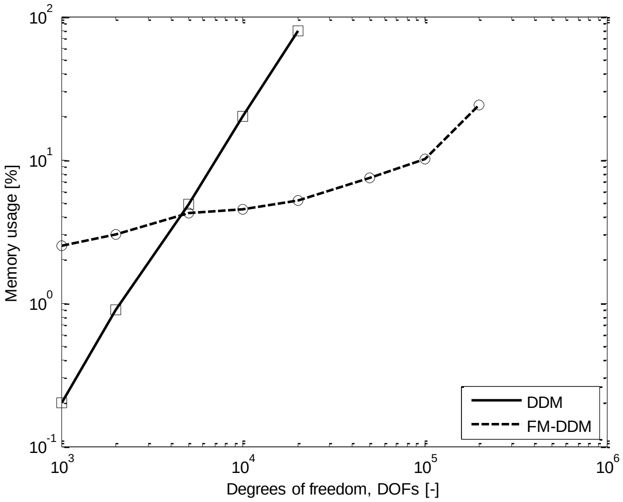

Figure 5-13. Comparison of the memory space between DDM and FM-DDM for increasing numbers of DOFs – Case 4.

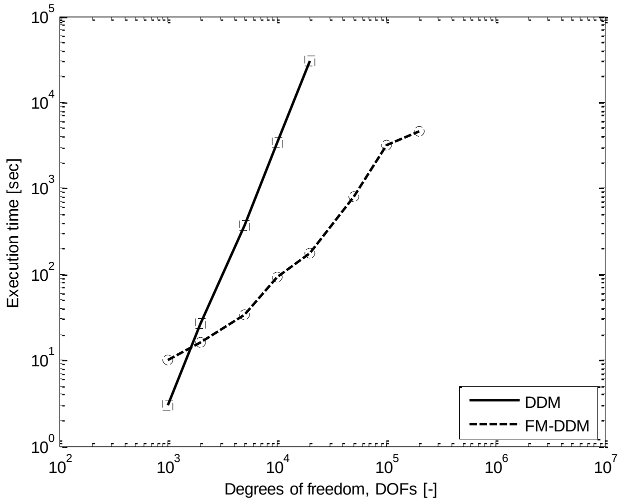

Figure 5-14. Comparison of the CPU time between DDM and FM-DDM for increasing numbers of DOFs – Case 4.

Table 5-3 presents the numerical values of Figs. 5-13 and 5-14 including the number of iterations for convergence required by the preconditioned version of FM-DDM. Moreover, the relative error of the final solutions between this iterative approach and the direct calculation (DDM) is also included for additional verification purpose.

Table 5-3. Computational performance of FM-DDM and DDM for various problem sizes – Case 4.

DOFs	DDM		FM-DDM			Error $x10^{-4}$ (%)
	Time (sec)	Mem. (%)	Time (sec)	Mem. (%)	No. Iter.	
1000	3	0.2	10	2.5	7	2.75
2000	27	0.9	16	3.0	8	1.54
5000	372	4.9	34	4.2	10	2.22
10,000	3372	20.2	93	4.5	10	2.02
20,000	30,000	80	176	5.2	14	1.98
50,000	-		794	7.4	16	-
100,000	-		3218	10.2	18	-
200,000	-		4522	24.3	22	-

The numbers of level *l* of the quad-tree for the first five (5) cases corresponding to 1000, 2000, 5000, 10,000, and 20,000 DOFs were 2, 2, 3, 3, and 4, respectively. As can be seen from Figs. 5-13 and 5-14, the memory and CPU time demanded by the conventional DDM present as expected a quadratic and cubic behaviour (a slope of 2 and 3 in the log-log plot) in terms of the DOFs. Also, the maximum number of DOFs that DDM can handle was around 20,000 with the available memory resources (4 GB) after 8.3 hours of computation.

On the other hand, FM-DDM shows a linear trend exhibiting a theoretical unit slope in both memory and CPU time so larger problems can be treated. In comparison with DDM, only 1.2 hours was required by FM-DDM to obtain the solution for the largest fracture network and is more efficient for problems with more than 2000 DOFs. Note that by extrapolating the DDM's performance curves, the same simulation would require at least: i) 320 GB of RAM to construct and allocate the coefficient matrix, and ii) more than 1.2 years of computation to solve the linear system of equations, approximately. The FM-DDM also shows scalable properties as achieving convergence at comparable number of iterations for various problem sizes as shown in Table 5-2.

5.2.2. FED model evaluation – Cases 5 and 6

5.2.2.1. FED model for numerical solution – Case 5

Figure 5-15 shows the locations of the injector and producer wells within the fracture network associated with the largest problem of 200,000 DOFs.

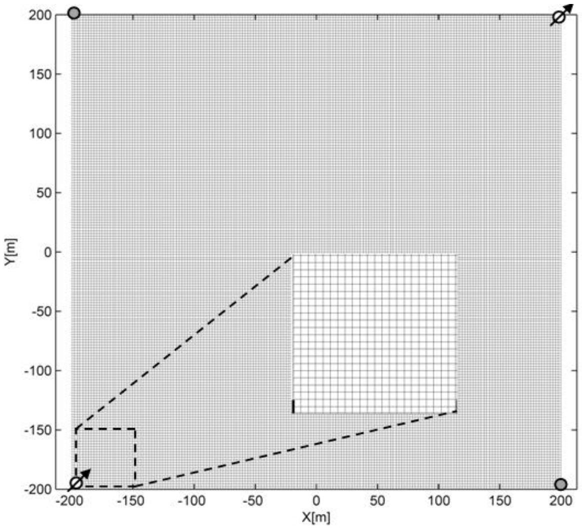

Figure 5-15. Locations of the injector and producer wells in the fracture network of 200,000 DOFs used to evaluate the performance of the FMM approach – Case 5.

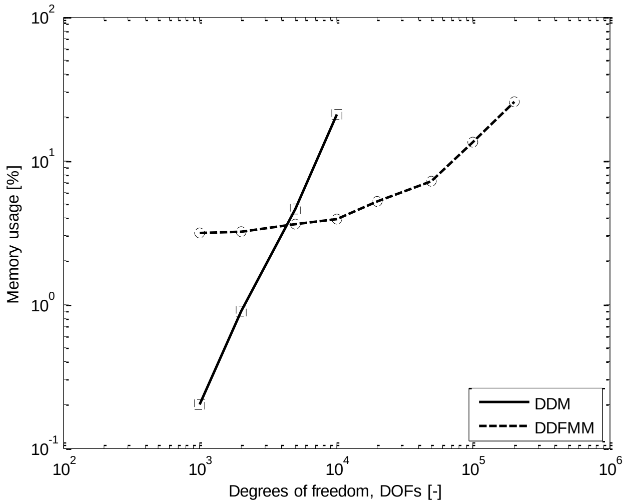

Figure 5-16. Comparison of the memory usage between DDM and the FMM proposed approach for increasing numbers of DOFs – Case 5.

Figures 5-16 and 5-17 show the percent of RAM memory and execution time required by the FMM approach and the conventional DDM to perform coupled fluid flow-geomechanical simulations of increasing number of DOFs, respectively. Table 5-4 presents the numerical values of Figures 5-16 and 5-17 including the number of iterations for convergence required by the preconditioned version of the program. For additional verification purposes, the relative error of the fluid pressure at the end of the injection between the direct calculation (DDM) and FMM approach is also included. The number of levels *l* of the quad-tree for the eight (8) cases corresponding to 1000, 2000, 5000, 10,000, 20,000, 50,000, 100,000, and 200,000 DOFs were 2, 2, 3, 3, 3, 4, and 4, 5, respectively.

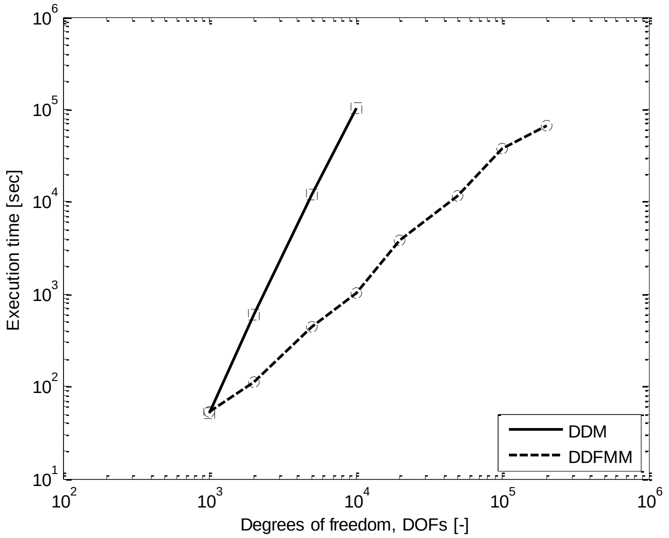

Figure 5-17. Comparison of the CPU time between DDM and the proposed FMM approach for increasing numbers of DOFs – Case 5.

Figure 5-18 presents the fluid pressure distribution for the largest regular fracture network of 66,666 boundary elements (or 200,000 DOFs as every element has associated three unknowns) used for this case.

Table 5-4. Computational performance of the FMM approach and DDM for various problem sizes – Case 5.

DOFs	DDM		FM-DDM			Error $x10^{-12}$ (%)
	Time (sec)	Mem. (%)	Time (sec)	Mem. (%)	No. Iter.	
1000	51	0.2	53	3.1	245	13.51
2000	589	0.9	112	3.2	286	5.23
5000	12,090	4.6	448	3.6	326	3.12
10,000	102,000	21.1	1010	3.9	400	0.82
20,000	-	-	3777	5.2	476	-
50,000	-	-	11,463	7.1	699	-
100,000	-	-	38,110	8.5	878	-
200,000	-	-	65,690	25.7	1043	-

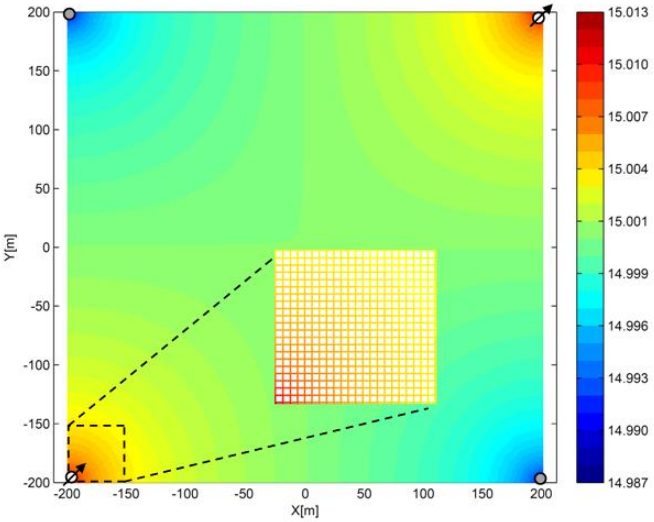

Figure 5-18. Fluid pressure distribution (in MPa) at the end of injection for the largest fracture network of 200,000 DOFs used to evaluate the FMM approach – Case 5.

Figs. 5-16 and 5-17 show as expected that the memory and execution time employed by the conventional DDM presents a quadratic and cubic behaviour in term of the DOFs. With the available RAM memory (4 GB), DDM needed 21.1% (0.844 GB) for the 10,000 DOFs case after 28.3 hours of computation and is only able to handle a maximum of 20,000 DOFs which were estimated by extrapolating the quadratic performance curve. On the other hand, the proposed simulator showed a linear trend in both memory and CPU time so larger number of fracture elements can be evaluated. In contrast with the conventional method, the current approach based on the FM-DDM is faster (higher memory-efficient) than DDM for problems with more than 1000 (4000) DOFs needing only 25.7% of memory and 18.4 hours to solve the largest fracture network problem. Note that in the hypothetical case of doing the same calculation in a personal computer using DDM, such computation would require 4x100 GBs of RAM and more than 317 years of computation, approximately. Finally, see in Table 5-4 that again the proposed simulator achieves solution convergence at comparable number of iterations for various problem sizes, showing additionally scalable properties.

5.2.2.2. FED model for visualization purposes – Case 6

This case study evaluates the execution time of FM-DDM for visualizing high-resolution stress variations in large-scale fracture networks. Figure 5-19 shows the CPU time used by DDM and FM-DDM to compute the normal stress distribution around 10,000 horizontal fractures with increasing number of field points. Table 5-5 presents the associated numerical values of Fig. 5-19. Note in this figure how the complexity of the matrix-vector multiplication required to compute the stress components at the prescribed field locations has been successfully reduced from a quadratic calculation with conventional DDM to linear one using FM-DDM. According with the values in Table 5-5, an average speed-up, which is the ratio between the execution time of DDM and FM-DDM, of 4.5 was gained over the conventional DDM for this particular case study with an apparent superior performance for higher number of fractures.

Table 5-5. Computational performance of DDFMM and DDM for different visualization data-sets – Case 6

Filed points	Execution time [sec]		Speed up [-]
	DDM	FM-DDM	
100,000	335	69	4.85
200,000	661	165	4.0
400,000	1328	261	5.0
600,000	2069	481	4.3
1,000,000	-	645	-

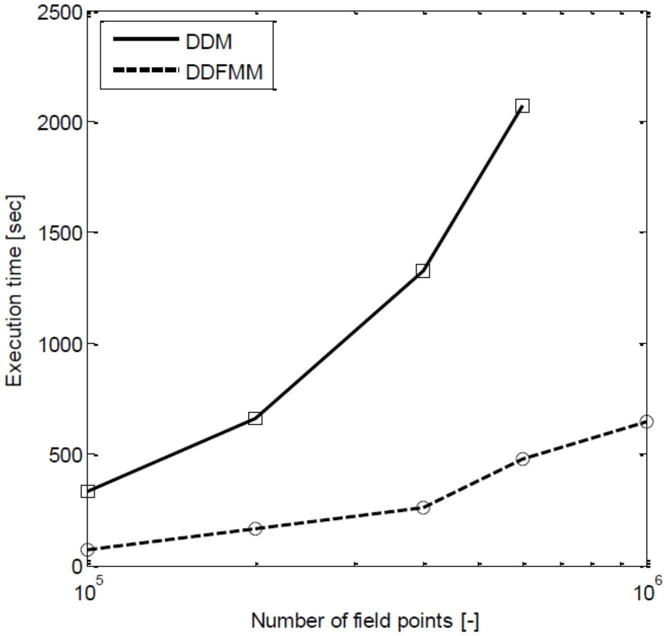

Figure 5-19. Comparison of the CPU time between DDM and FM-DDM for increasing numbers of field points – Case 6

Figure 5-20 shows the normal stress distribution for the fracture network with the highest number of field points (one million) using FM-DDM. Additionally, Figure 5-21 presents a comparison of the above spatial distribution computed with FM-DDM (right) within a small section of the domain with those obtained with DDM (left) using fewer number of field points (200,000). Note how by the inclusion of more field locations additional and subtle details are captured for a better representation (more similar to that presented in Fig. 5-19 for parallel fractures) with a comparable computation time.

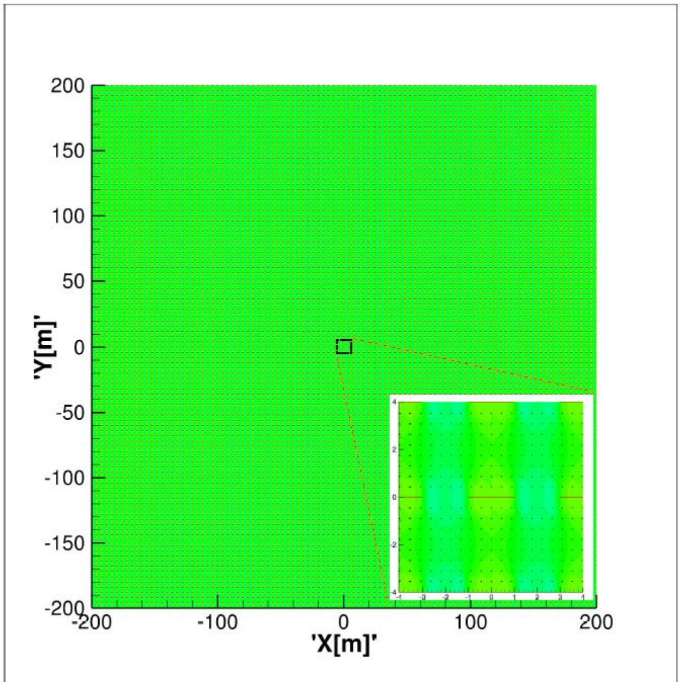

Figure 5-20. Normal stress distribution created with one million field point locations in a reservoir with 10,000 horizontal fractures. Stress variations in the central dashed zone is enlarged and showed for visualization and further comparison purposes – Case 6.

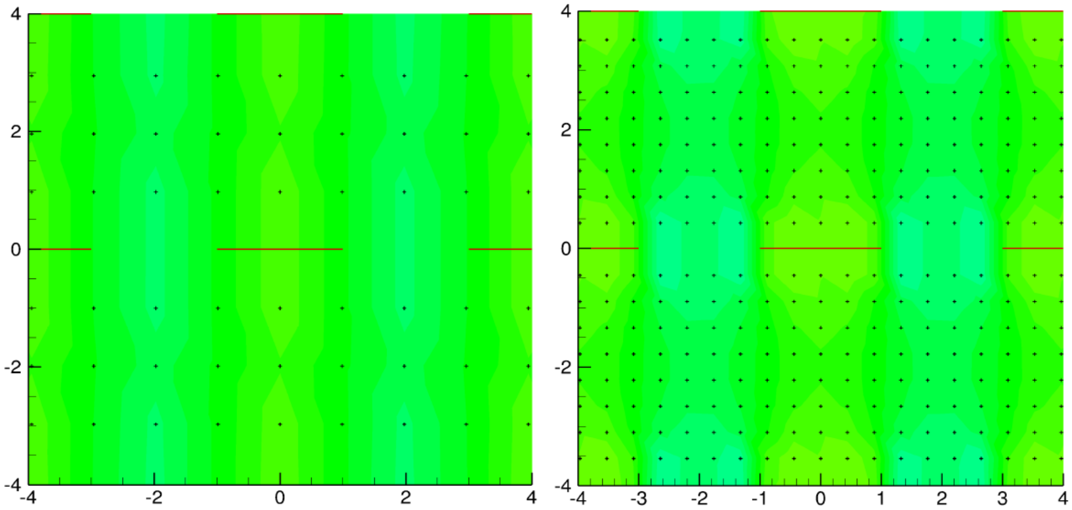

Figure 5-21. Comparison of the normal stress distribution within the small zone of Fig. 8 computed with DDM (left) and FMM (right) using 200,000 and one million field points, respectively – Case 6.

5.2.3. FPDD model evaluation – Case 7

This case study considers a naturally fractured network undergoing fluid injection and production through a five-spot pattern. For the largest problem of 100,000 DOFs, the reservoir dimension, fracture distribution (regular mesh), and locations of wells are presented in Figure 5-22. Input data for this case study can be found in Table 5-6. Note that a constant flow rates is specified on each well and the corresponding magnitude is obtained by dividing the total flow rate presented in Table 5-6 by the number of injector or producer wells. The memory demand and CPU time required by both the conventional poroelastic DDM and the FMM approach are showed in Figures 5-23 and 5-24 after executing geomechanics models of increasing number of degrees of freedom (DOFs), respectively.

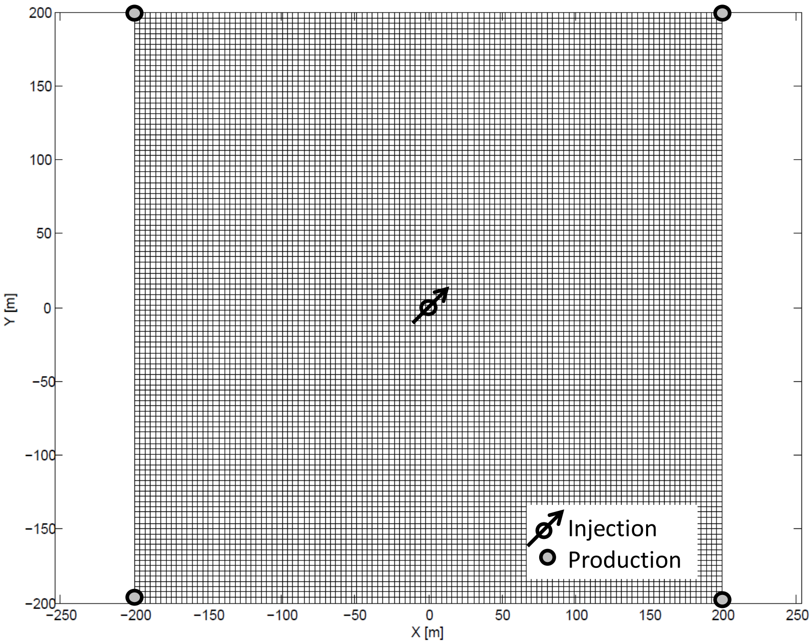

Figure 5-22. Locations of the injector and producer wells in the fracture network of 100,000 DOFs used to evaluate the performance of the FMM approach – Case 7.

Table 5-6. Input data for the FPPD model evaluation – Case 7.

Parameter	Value
Shear modulus, G, (GPa)	15
Poisson's ratio, v, (-)	0.1
Shear joint stiffness, K_s (GPa/m)	7.5
Initial normal stiffness, K_{ni}, (GPa/m)	3.0
Maximum fracture closure, D_{nmax}, (m)	$5\text{x}10^{-4}$
Far-field stress in xx direction, σ_{xx}^{∞} , (MPa)	20
Far-field stress in yy direction, σ_{yy}^{∞}, (MPa)	20
Far-field stress in xy direction, σ_{xy}^{∞}, (MPa)	0
Initial fracture aperture, D_n^0, (m)	$3\text{x}10^{-3}$
Initial shear displacement, D_s^0, (m)	0
Initial fluid pressure, p, (MPa)	19
Fluid compressibility, c_f, (1/MPa)	$5\text{x}10^{-5}$
Fluid viscosity, μ_f, (MPa.s)	$1\text{x}10^{-9}$
Matrix permeability, k, [m^2]	$0.4\ \text{x}10^{-15}$
Porosity, ϕ, [-]	0.02
Biot's poroelastic coefficient, α, [-]	0.4399
Dilation angle, ϕ_d, [rad]	0
Number of Chebyshev nodes per dimension, n, (-)	5
Number of time steps, h, (-)	20

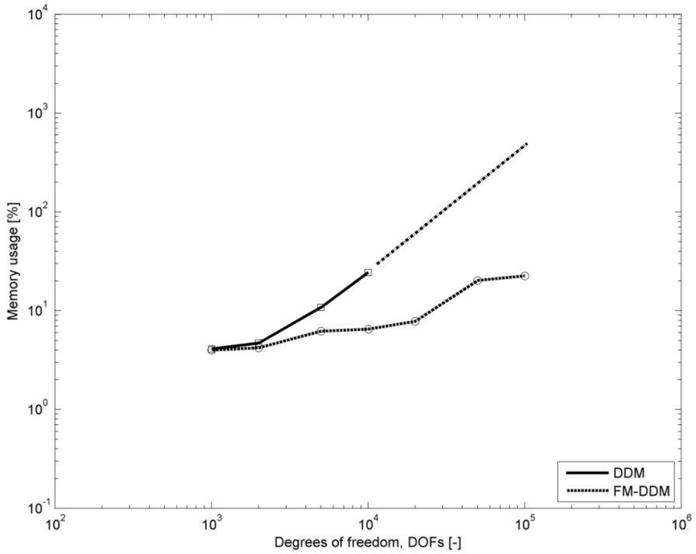

Figure 5-23. Comparison of the memory usage between DDM and the proposed FMM approach for increasing numbers of DOFs – Case 7.

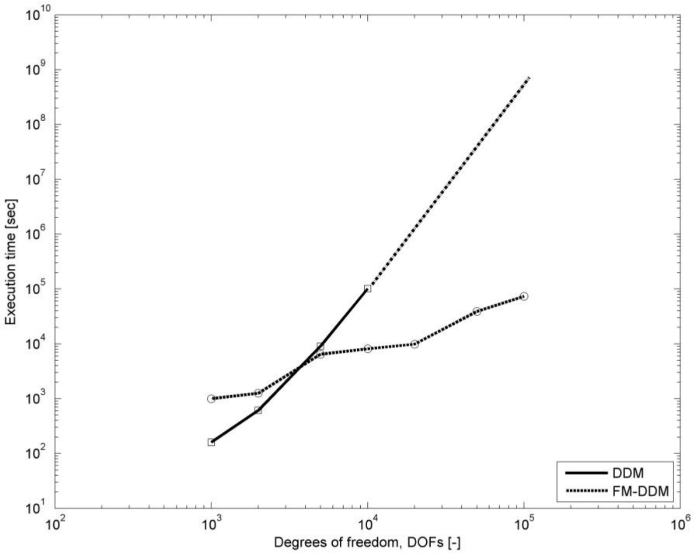

Figure 5-24. Comparison of the CPU time between DDM and the proposed FMM approach for increasing numbers of DOFs – Case 7.

Table 5-7 shows the corresponding numerical values along with the total number of iterations for convergence. In Table 5-5, the relative error of the pore-pressure at the end of the injection process computed with the conventional DDM and the FMM approach is also included for an additional verification. For the seven (7) cases corresponding to 1000, 2000, 5000, 10,000, 20,000, 50,000, and 100,000 DOFs, the number of levels *l* of the quad-tree associated with the FMM approach were 3, 3, 4, 4, 4, 5, and 5, respectively. For the largest problem of 100,000 DOFs, the fracture network is discretized using 25,000 boundary elements (as every element has associated four DOFs). The corresponding spatial distribution of the pore-pressure at the end of injection is presented in Figure 5-25.

Table 5-7. Computational performance of the FMM approach and DDM for various problem sizes – Case 7.

DOFs	DDM Time (sec)	DDM Memory (%)	FM-DDM Time (sec)	FM-DDM Memory (%)	FM-DDM No. Iter.	Error $x10^{-9}$ (%)
1000	160	4.1	1003	4.0	455	206.27
2000	610	4.7	1256	4.2	547	102.30
5000	9084	10.8	6464	6.2	583	2.49
10,000	100713	24.4	8115	6.5	503	58.41
20,000	-	-	9843	7.8	500	-
50,000	-	-	38900	20.2	553	-
100,000	-	-	73753	22.5	684	-

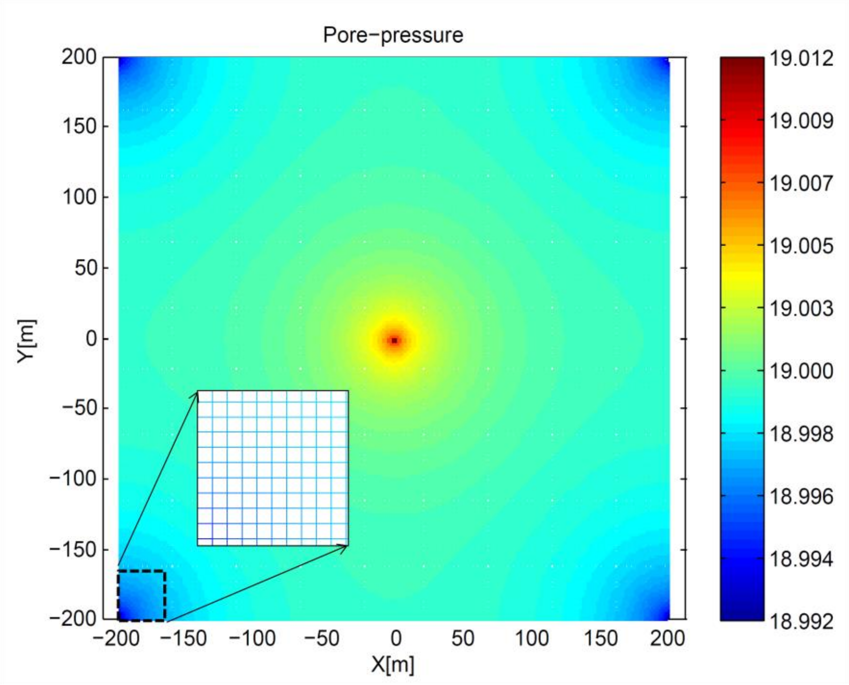

Figure 5-25. Pore-pressure distribution (in MPa) at the end of injection for the largest fracture network of 100,000 DOFs used to evaluate the FMM approach – Case 7.

On the other hand, memory and execution time demanded by the conventional poroelastic DDM show as expected quadratic and cubic trends with respect to the number of unknowns. In reference to the case of 10,000 DOFs, the conventional DDM needed 24.4% (0.976 GB) after 28 hours of processing. By extrapolating its performance curve (dash-dot line), DDM would be able to solve optimistically up to 20,000 DOFs with the current computational resources.

In contrast, a linear performance in both memory and CPU time is showed by the FMM approach so larger problem can be executed. The poroelastic FM-DDM is faster and save more memory than the conventional method for problems with more than 1000 and 4000 unknowns, respectively. In fact, solving the largest fracture network the FMM approach only needed 22.5% of memory with 20.5 hours of calculation. Note that the same calculation using DDM would require 400% more RAM with more than 31.7 years of computation, approximately. Finally, values in Table 5-7 suggest again that the FMM approach exhibit scalable properties by achieving solution convergence at comparable number of iterations even for higher problems sizes.

6. NUMERICAL APPLICATIONS

The proposed method described in Section 5 to evaluate large-scale geomechanical models is used here for several numerical applications. By using FM-DDM, complex interactions between hydraulic and natural fractures are computed and a more realistic opening distribution of the transverse fractures is obtained. In addition, fast visualization of high-resolution stress distribution around fracture intersections are obtained with low-computational resources for realistic representation and characterization of unconventional reservoirs. Finally, several production scenarios in elastic and poroelastic fractured reservoirs are evaluated after computing the coupled flow-geomechanical response associated with different well type, location and configuration.

This section begins describing an application for multiple transverse fractures in unconventional reservoirs using the elastic deformation (ED) model explained in Section 2. Next, examples using the flow-elastic deformation (FED) model for the transient and spatial response of fracture networks are presented. Finally, a case study using the flow-poroelastic deformation and diffusion (FPDD) for the fluid injection and production in a large-scale poroelastic network is shown. Input data for all case studies is the same as in Section 5.

6.1. Multiple transverse fractures in unconventional reservoirs – Case 1

The objective of this case study is to evaluate mechanical interactions between a network of naturally fractures and a set of transverse hydraulic fractures as commonly found in unconventional reservoirs and to further illustrate the computational efficiency of FM-DDM to consider large-scale geomechanical interactions during reservoir stimulation. The three parallel hydraulic fractures, orientated perpendicular to the horizontal well, intersect an interconnected natural fracture network whose elements are distributed in the reservoir with different locations, lengths, and angles (See Fig. 6-1).

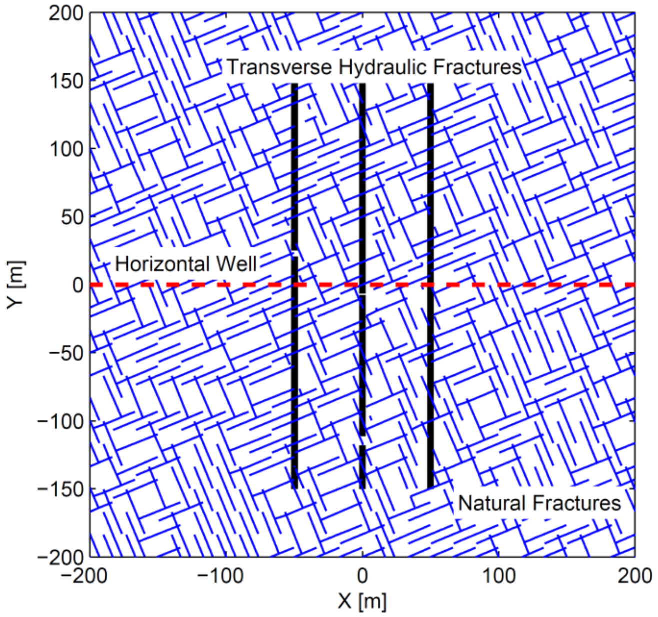

Figure 6-1. Distribution of natural fractures in the reservoir and location of the transverse hydraulic fractures – Case 1.

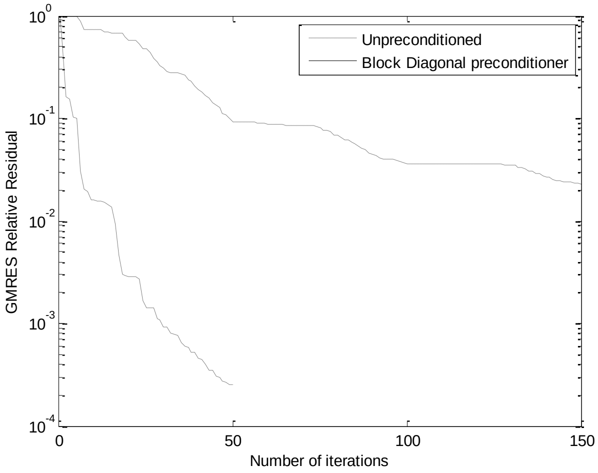

Figure 6-2. Minimization of the relative error during the iterative search for the preconditioned and non-preconditioned FM-DDM – Case 1.

Exploiting the ability of FM-DDM to solve for larger problems, a fine discretization scheme is applied to capture high level of detail using 17,000 fracture elements (34,000 DOFs) of average length of 0.65 m. One set of natural fractures is oriented 22.5 degrees respect to x-axis and the other set is perpendicular to it. The minimum and maximum spacing for both directions are 5.6 m and 25.8 m. The average spacing between the co-linear ones is around to 15.3 m. Constant fluid pressure is assumed in all fractures (10 MPa in the natural fractures and 5 MPa of net pressure in the hydraulically induced ones) as our analysis considers the injection fluid has filled the fractures and the pressure is stabilized. Additionally, neither fracture propagation nor proppant transport is modeled.

Figure 6-2 presents the curves of the relative error during the iterative search for both non-preconditioned and preconditioned versions of FM-DDM. Note that the block-diagonal preconditioner helps to achieve convergence after 48 iterations (497 sec) in contrast with the unpreconditioned version which after 150 iterations (1615 sec) could not drastically reduce the error. Figure 6-3 shows a graphical representation of the fracture opening (not to scale) and shear displacement of both natural and hydraulic fractures. For comparison purposes, Fig. 6-3 also includes in the upper left side the corresponding displacement results in the absence of the fracture network computed by FM-DDM similar to those reported using analytical and conventional numerical methods (Wu and Olson 2013). Note that in this simplified stimulation scenario, the two (2) exterior hydraulic fractures (left and right) have the highest normal aperture in the middle and maximum shear close to the tip. Here, the central fracture exhibits generally lower width as being under compression by the effect of the exterior fractures (Sesetty and Ghassemi 2012; Sesetty and Ghassemi 2013).

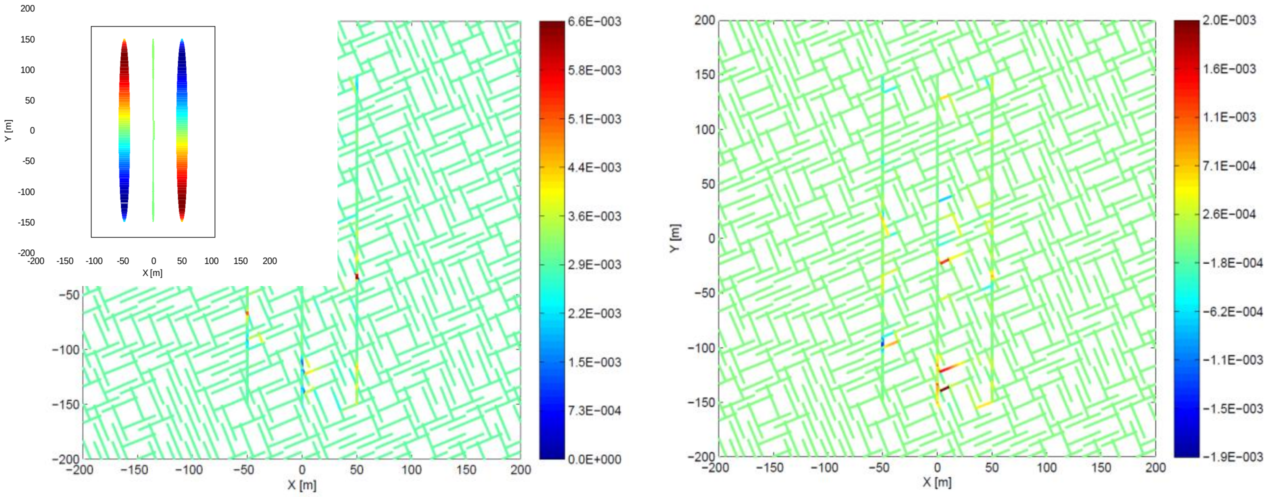

Figure 6-3. Final fracture width (left) and shear (right) DD computed with the preconditioned version of FM-DDM – Case 1.

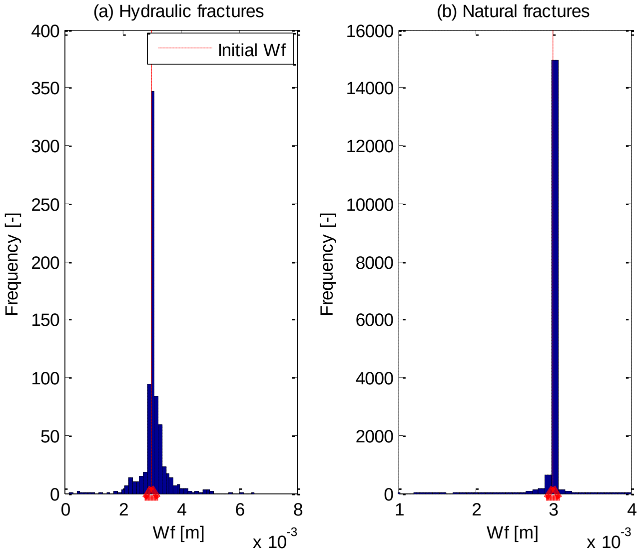

Figure 6-4. Histogram of the final normal aperture of boundary elements associated to both the hydraulic (left) and natural (right) fractures showing the distribution of values above (opening) and below (closure) the initial aperture – Case 1.

The results in Fig. 6-3 show more complex mechanical interactions in the fractured reservoir which create different profiles of the normal and shear displacements for the hydraulic fractures and also some of the natural fractures. The fracture elements with maximum normal aperture and shear displacement are located mostly along the transverse fractures where stress shadow is lower and shear stress is higher. But a well-defined pattern cannot be observed due to the complex nature of the network. Some fracture elements have experienced a decrease in aperture while others have increased apertures.

Figure 6-4 presents a histogram of the normal displacement associated with the hydraulic (left) and natural (right) fractures indicating the distribution of values above (opening) and below (closure) the initial aperture ($3x10^{-3}$ m). Note that around 60%

(75%) of the boundary elements corresponding to the hydraulic (natural) fractures are greater than the initial normal aperture, indicating some degree of stimulation in the reservoir.

6.2. A large-scale flow-geomechanical simulation in a fractured reservoir – Case 2

In this case study, the computational cost, convergence rate, and evolution of flow and geomechanical variables are evaluated. Figure 6-5 shows the locations of the two (2) injector and four (4) producer wells on the reservoir.

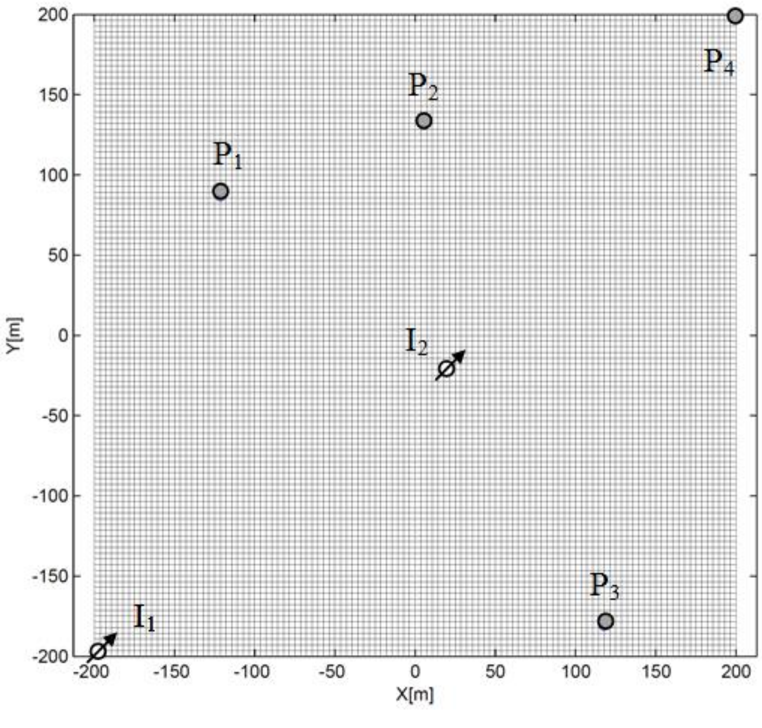

Figure 6-5. Locations of the injector and producer wells in the fracture network – Case 2.

The naturally fracture network is discretized using a regular mesh of 25,000 boundary elements (75,000 DOFs) exploiting the ability of the approach to solve for larger problems. Figure 6-6 shows the changes of the fluid pressure at the injector and producer wells during the simulation while Figure 6-7 shows the distribution of the fluid pressure in the fracture network at the beginning (0.047 sec) and at the end of the injection. On the other hand, Figures 6-8 and 6-9 shows the distributions of the shear displacement discontinuity and fracture width in the network at the corresponding times. Finally, Figure 6-10 and 6-11 show the fracture permeability and the induced stress components σ_{xx}, σ_{yy}, and σ_{xy}, respectively.

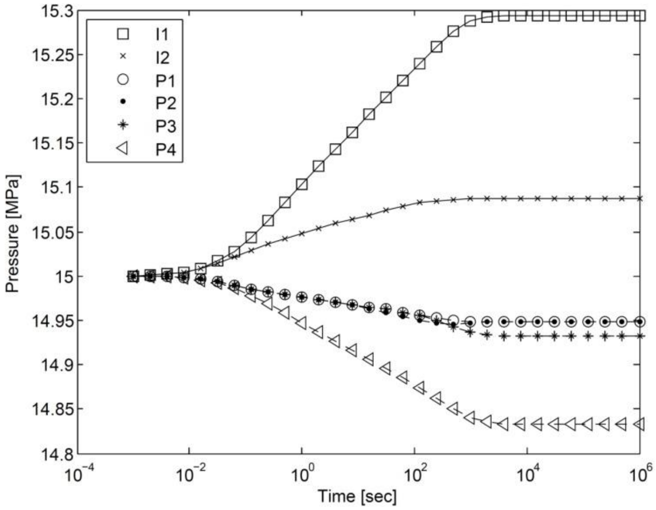

Figure 6-6. Changes of the fluid pressure at the injector and producer wells during the simulation – Case 2.

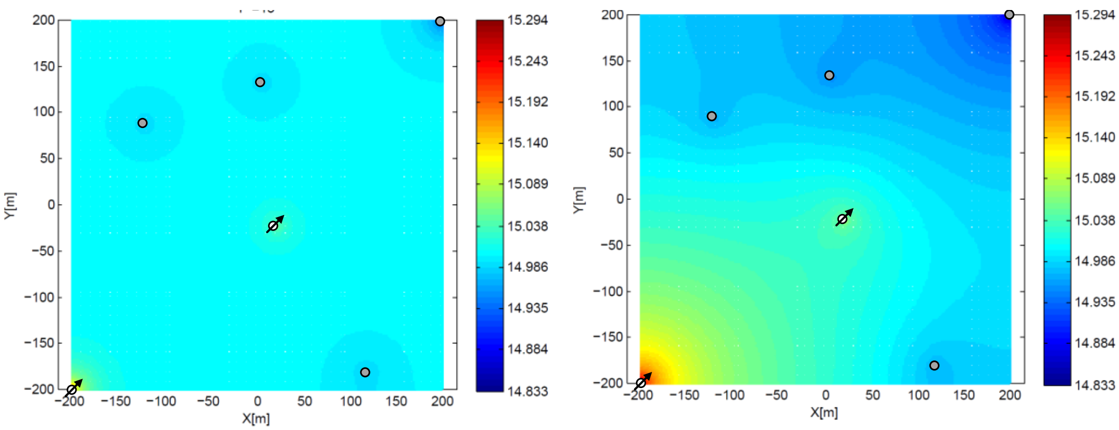

Figure 6-7. Distribution of the fluid pressure in the fracture network computed at the beginning (left) and at the end (right) of injection – Case 2.

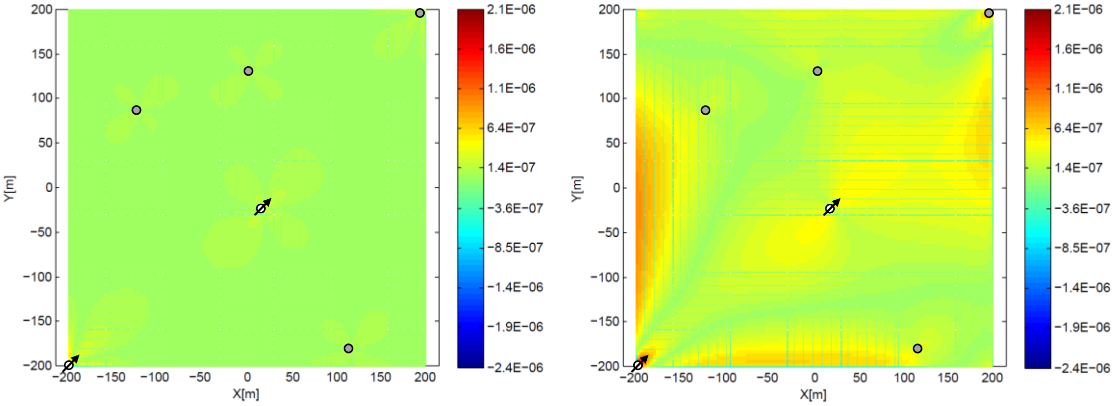

Figure 6-8. Distribution of the shear displacement discontinuity (D_s) in the fracture network computed at the beginning (left) and at the end (right) of injection – Case 2.

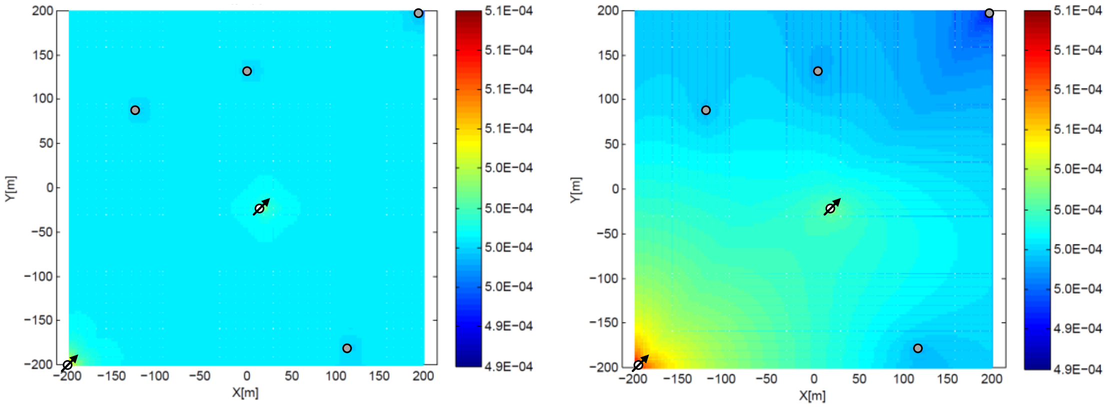

Figure 6-9. Distribution of the fracture width (W_f) in the fracture network computed at the beginning (left) and at the end (right) of injection – Case 2.

As shown in Fig. 6-6, the pressure at the injector (producer) wells increase (decrease) with time and reach a steady-state behavior near the end of injection. Therefore, and as expected, higher (lower) values of fluid pressure are found in regions around the injector (producer) wells. Note that these regions are well-separated at the beginning and their extension limited to fractures around the wells. However, after the fluid injection continues, the connection of these regions is evident and greater isobaric zones are formed in the fracture network (see Figure 6-7). Highest (positive and negative) shear displacement discontinuity in Fig. 6-8 are observed in the vicinity of the injector (I1) and producer (P4) wells during the simulation indicating relevant shear stress concentration at these locations with potential to modify the fracture permeability by shear dilation. Note also that when the injection commence, fracture aperture (or negative normal displacement discontinuity) are located mainly near the injector wells while regions away from this points experiment certain closure in special around the producers (see Fig. 6-9). At the end the injection, smaller changes in fracture aperture are found not only around the injection points but also in regions between them.

Note that fracture permeability in Fig. 6-10 has a pattern similar to the aperture distribution with higher (lower) values around injector (producer) well as expected according to Eq. (2-44). Variations of the spatial gradient apparently depend on several factors such as the relative position between those wells and the induced stresses. The stress distributions are presented in Figure 6-11.

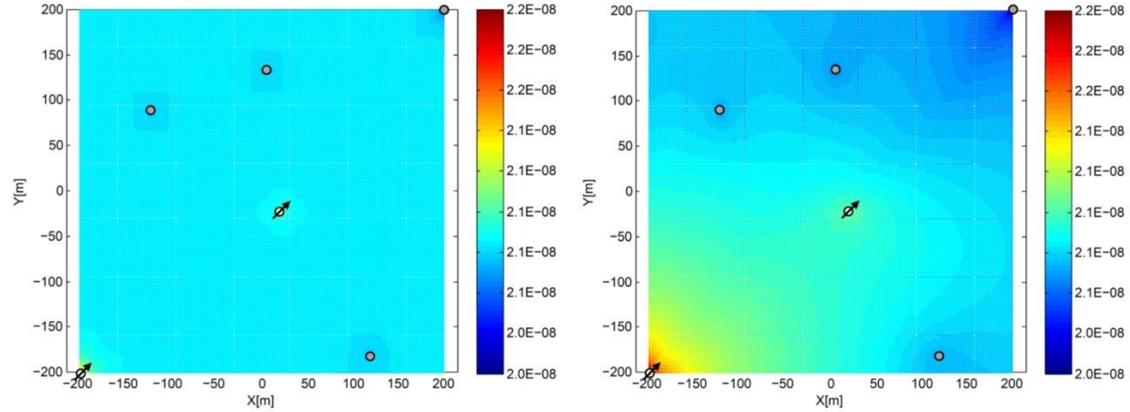

Figure 6-10. Distribution of the fracture permeability (k_f) in the fracture network computed at the beginning (left) and at the end (right) of injection – Case 2.

An analysis of those stress distributions reveals that the gradient of σ_{xx} and σ_{yy} are orientated in the vertical and horizontal directions and in general showing positive (compression) values in the upper-right zone due to the fluid production (P4) and negative (traction) ones on the lower-left corner as a consequence of the injection (I1). Finally inspecting σ_{xy} contour plot, it follows the trend of the associated displacement discontinuity (Fig. 13) presenting higher variations concentrated on the left and lower sides of the fractured reservoir due to the effects of the injection.

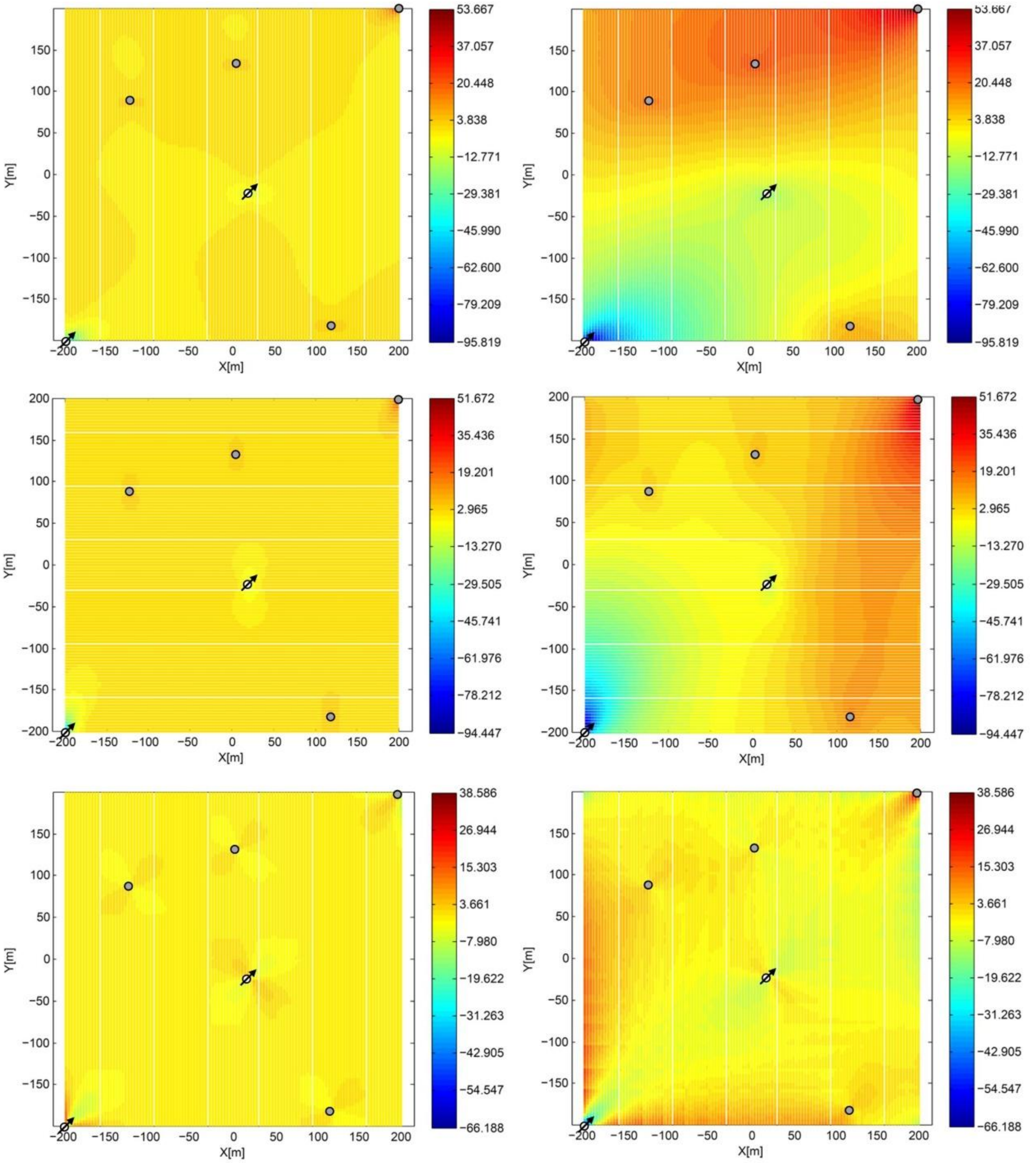

Figure 6-11. Distribution of the induced stresses σ_{xx} (top), σ_{yy} (middle), and σ_{xy} (bottom) in the fracture network computed at the beginning (left) and at the end (right) of injection. Units are in kPa – Case 2.

6.3. Geomechanical response of fractured reservoirs due to injection – Case 3

This case study computes the stress distributions in a reservoir at different times caused by the isothermal fluid injection through an irregular fracture network. The dimension and distribution of the 1000 fractures (16.6 meters each one) as well as the locations of the injector and producer wells at the center of the fracture elements are showed in Figure 6-12. A large number of field points (160,000) were used to capture higher details of the stress variations above and below the initial field stress. Transient numerical solutions were obtained by solving the flow-elastic deformation (FED) model described in Section 2.

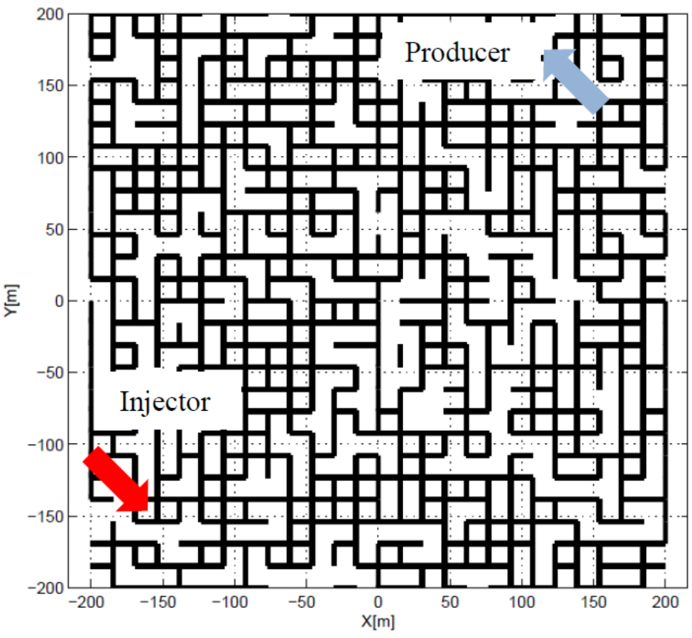

Figure 6-12. Fractured reservoir used for the injection process indicating the locations of the injector and producer wells– Case 3.

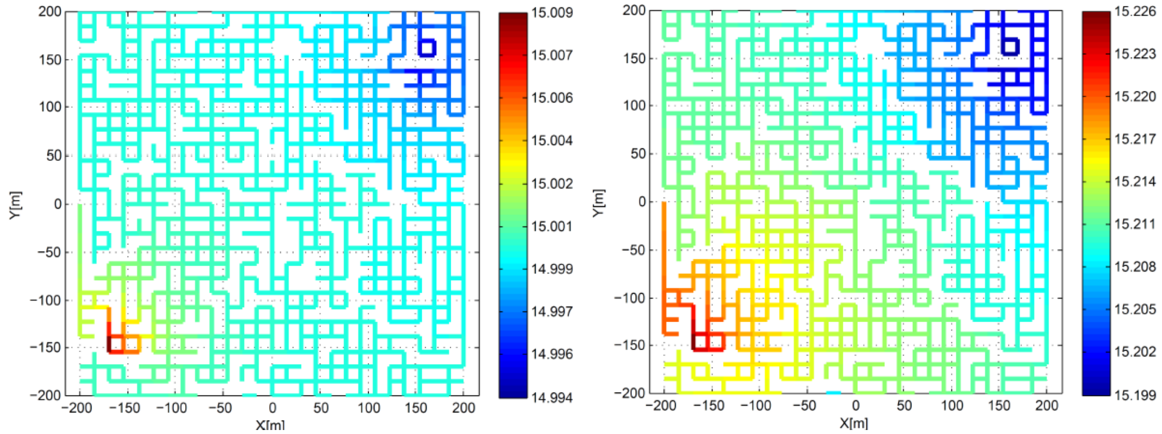

Figure 6-13. Fluid pressure in the fracture network after 2 (left) and 60 (right) days of injection – Case 3.

The fluid pressure in the fracture network during the injection is presented in Figure 6-13. Figure 6-14 presents the mean stress distribution in the reservoir using 160,000 field points after 2 (left) and 60 (right) days of injection. The small dashed zone on the bottom left is used in Figure 6-14 to compare with more details the stress variations near the injector well. A quick examination of Fig. 6-14 shows that slightly changes of the initial value occurred at the beginning of the injection but increase in magnitude during the process. Note that at later times, higher stress values are concentrated around the intersection of fractures where most of them seem to be distributed along NE-SW directions. This coincides with the natural path for the movement of fluids from the injector to the producer wells because greater normal displacements (and then normal stress) are created along this direction to provide transport conduits to the fluid flow.

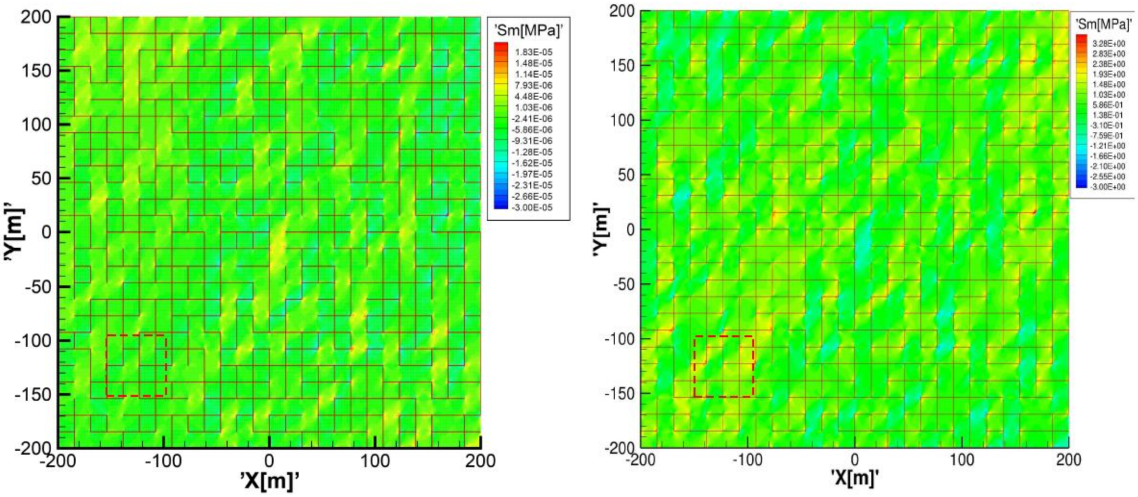

Figure 6-14. High fidelity mean stress distribution in the reservoir constructed using 100,000 field points after 2 (left) and 60 (right) days of injection – Case 3.

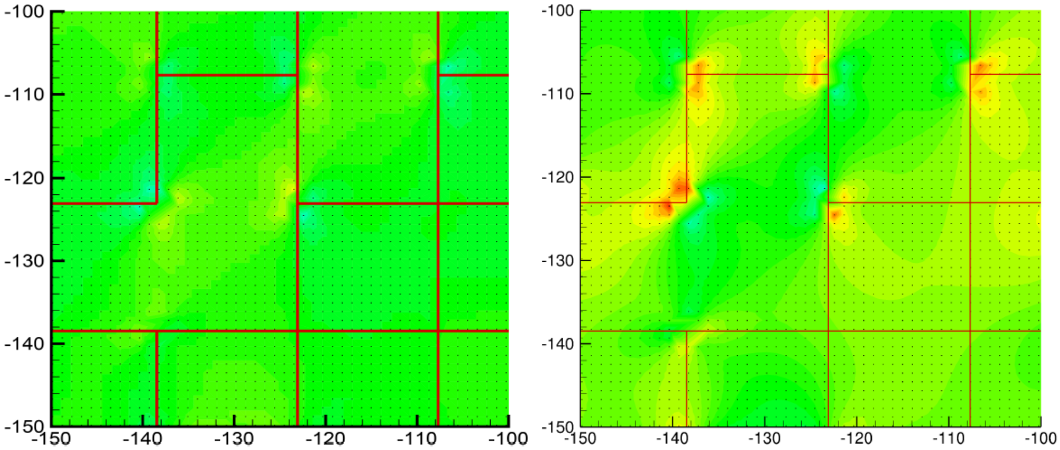

Figure 6-15. Comparison of the mean stress variations near the injector well after 2 (left) and 60 (right) days of fluid injection – Case 3.

Finally as can be seem in Fig. 6-15 (right), a closed inspection of the stress variation near the injector reveals that larger number of field points help to construct a more accurate but computationally cheap spatial distribution in this small area using FM-DDM. It shows again higher stress concentrations at the fracture's intersections that could potentially lead to, for instance, fracture initiation and propagation.

6.4. Fluid injection and production in large-scale poroelastic shales – Case 4

The dynamic evolution of flow and geomechanics variables in a poroelastic shale is analyzed in this case study. For this purpose, an irregular fractured reservoir with sealing faults containing 10,000 boundary elements with two (2) injectors and three (3) producer wells is proposed (see Figure 6-16). The transient response of the pore pressure at the injector and producer well are plotted in Figure 6-17 and the associated spatial distribution of geomechanical and flow variables are presented in Figures 6-18 and 6-19, respectively. For additional details, Figure 6-20 shows the corresponding distribution of the induced stresses in the fracture network computed at the beginning and at the end of the process.

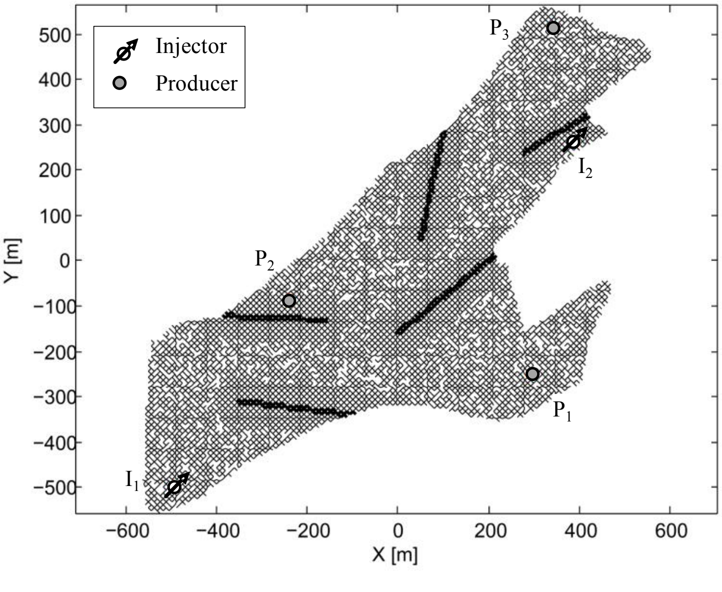

Figure 6-16. Locations of the injector and producer wells in the fracture network with sealing faults – Case 4.

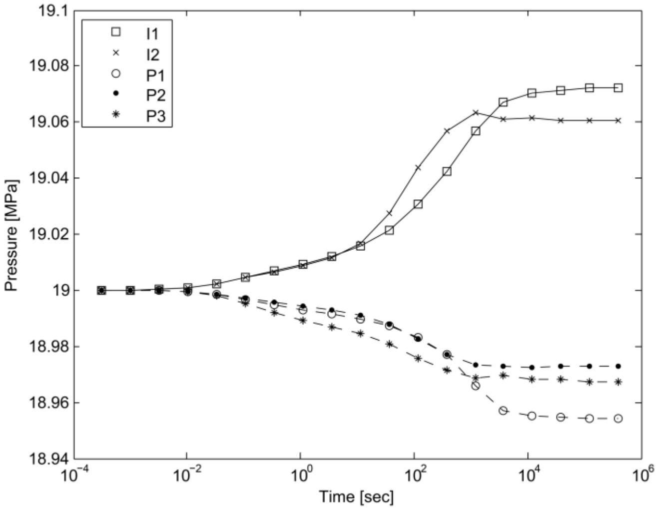

Figure 6-17. Transient response of the pore pressure at the injector and producer wells – Case 4.

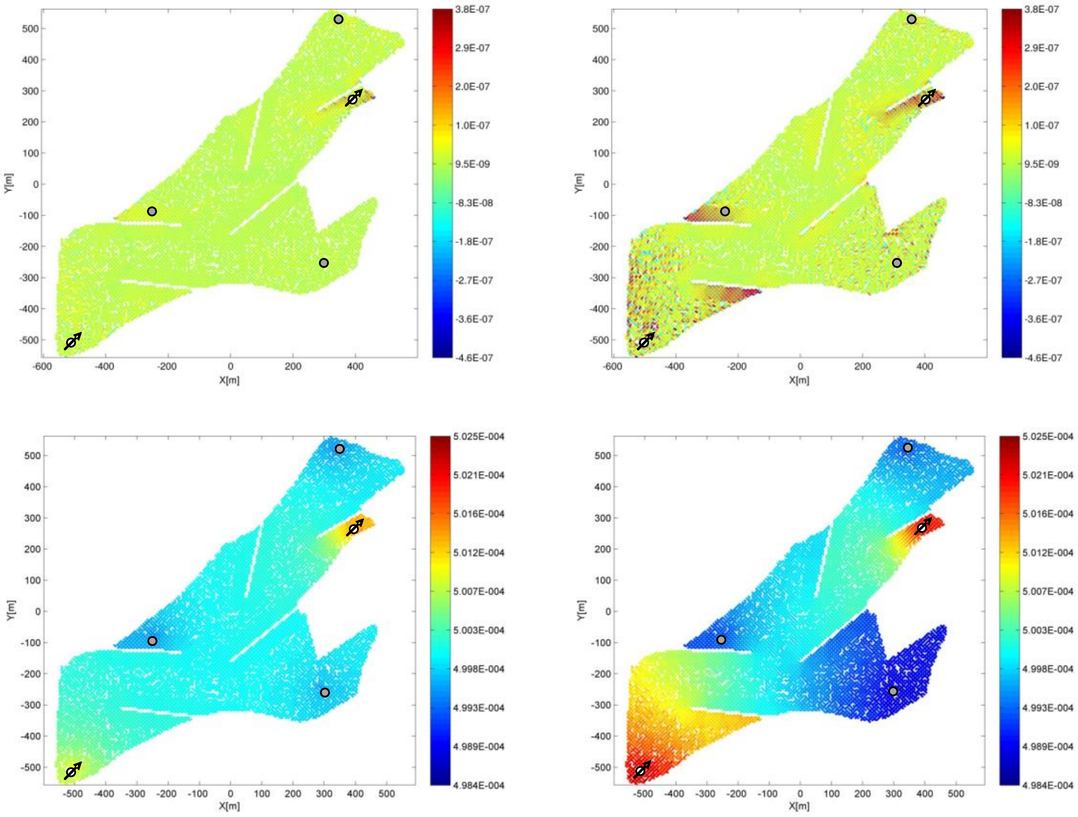

Figure 6-18. Distribution of shear displacement (top) and fracture width (bottom) in the fracture network with sealing faults computed at the beginning (left) and at the end (right) of simulation. Units for D_s and W_f are in m, respectively – Case 4.

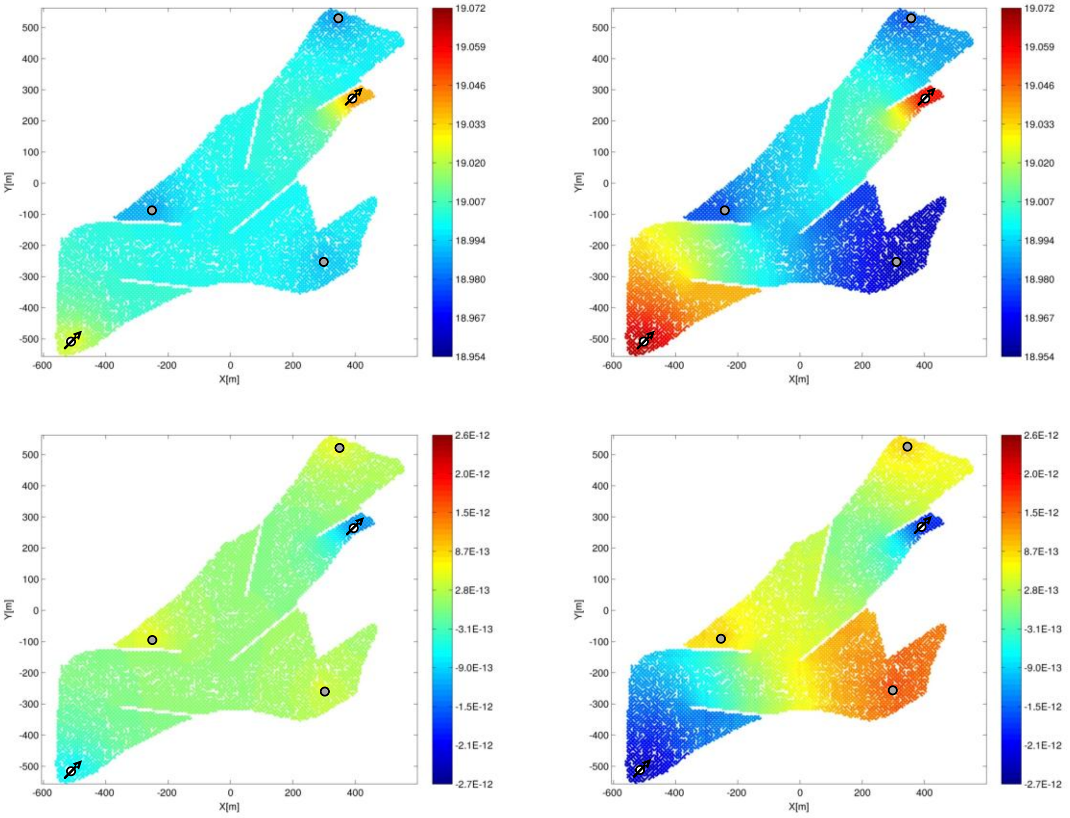

Figure 6-19. Distribution of pore pressure, *p*, (top) and fluid leak-off, Q_l, (bottom) in the fracture network with sealing faults computed at the beginning (left) and at the end (right) of simulation. Units for *p* and Q_l are in MPa and m^2/sec, respectively – Case 4.

For comparison purposes, Figure 6-21 presents the pressure evolution at the injector and producer wells in the network with and without sealing faults. The corresponding pore pressure, fluid leak-off, and fracture permeability are presented in Figure 6-22. Finally, Figure 6-23 presents the evolution of wellbore pressure for both the elastic and poroelastic faulted network cases.

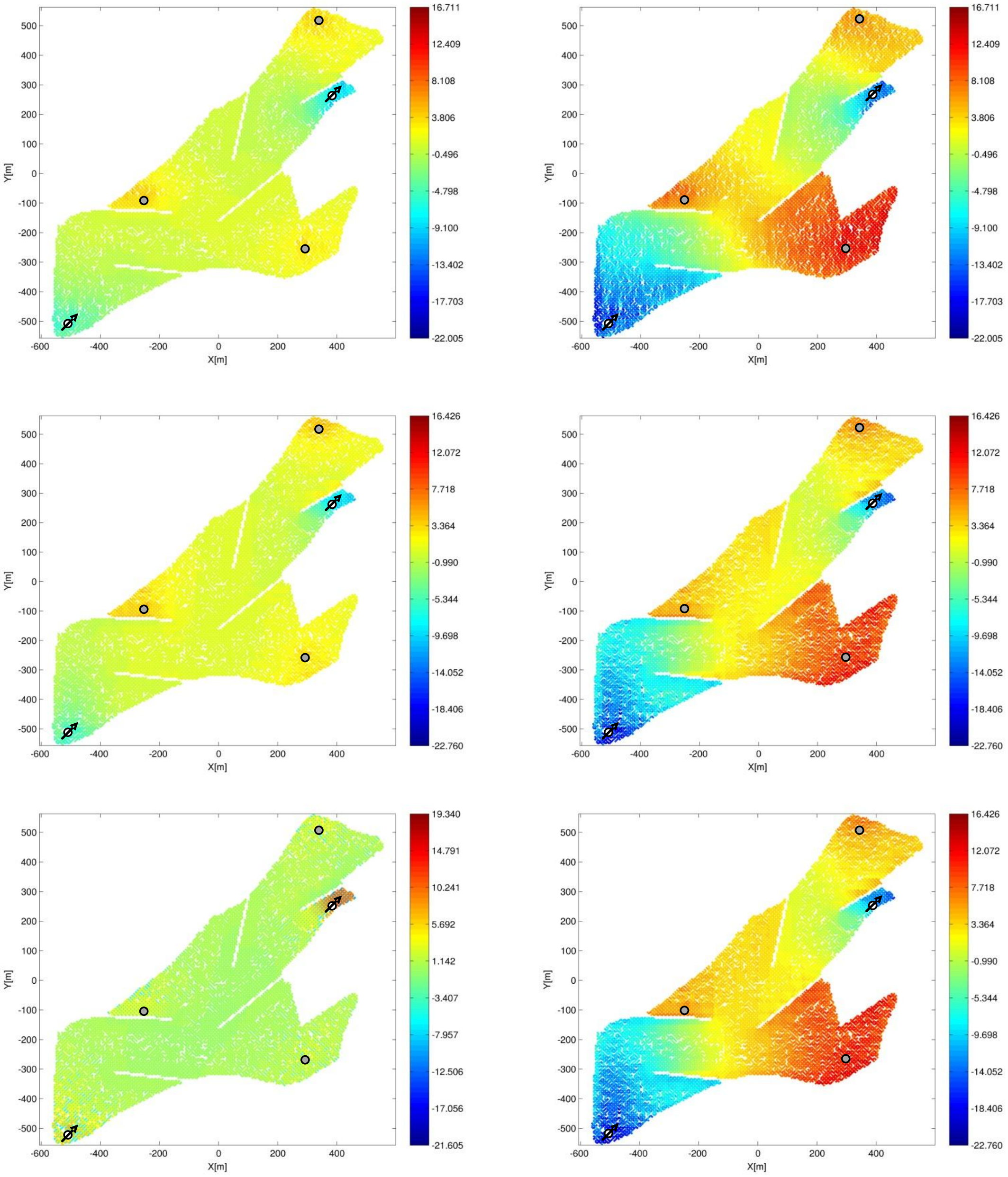

Figure 6-20. Distribution of the induced stresses σ_{xx} (top), σ_{yy} (middle), and σ_{xy} (bottom) in the fracture network with sealing faults computed at the beginning (left) and at the end (right) of injection. Units are in kPa along with tension positive as the sign convention – Case 4.

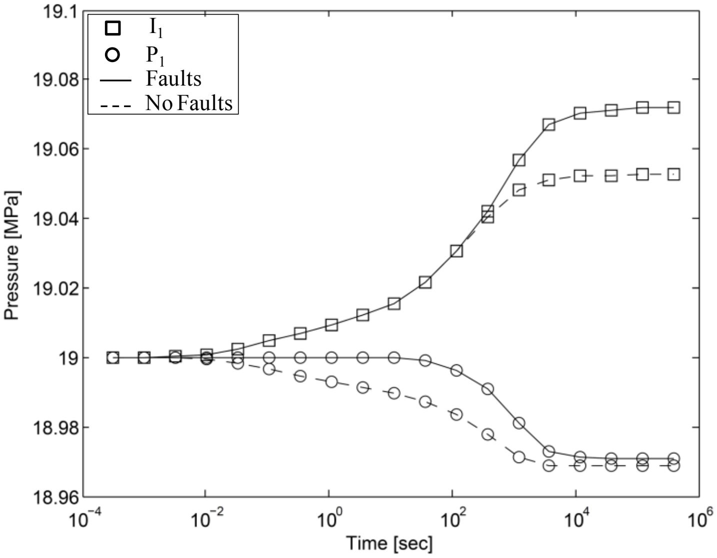

Figure 6-21. Comparison of the pressure evolution at the injector and producer wells in the poroelastic fracture network with and without sealing faults – Case 4.

As can be seen in Fig. 6-17, the pore pressure is higher (lower) at the injector (producer) wells and increases (decreases) with time stabilizing near the end of the simulation. Figs. 6-18 and 6-19 reveal that geological faults play an important role in the reservoir dynamic even at the early stage of the injection. The sealing faults create flow barriers in the fracture network and introduce compartmentalization that produce discontinuous spatial distribution of both geomechanical and flow variables that potentially impact the fluid recovery. In particular, Fig. 6-20 presents how the induced stresses are generally homogeneous in most of the domain's compartments where fluid injection/extraction is carried out showing only stress gradients in the central area of the reservoir where those compartments are in communication.

Note that, for example, if the sealing faults are removed, the pressure response (Fig. 6-21) as well as the flow variables (Fig. 6-22) would change drastically.

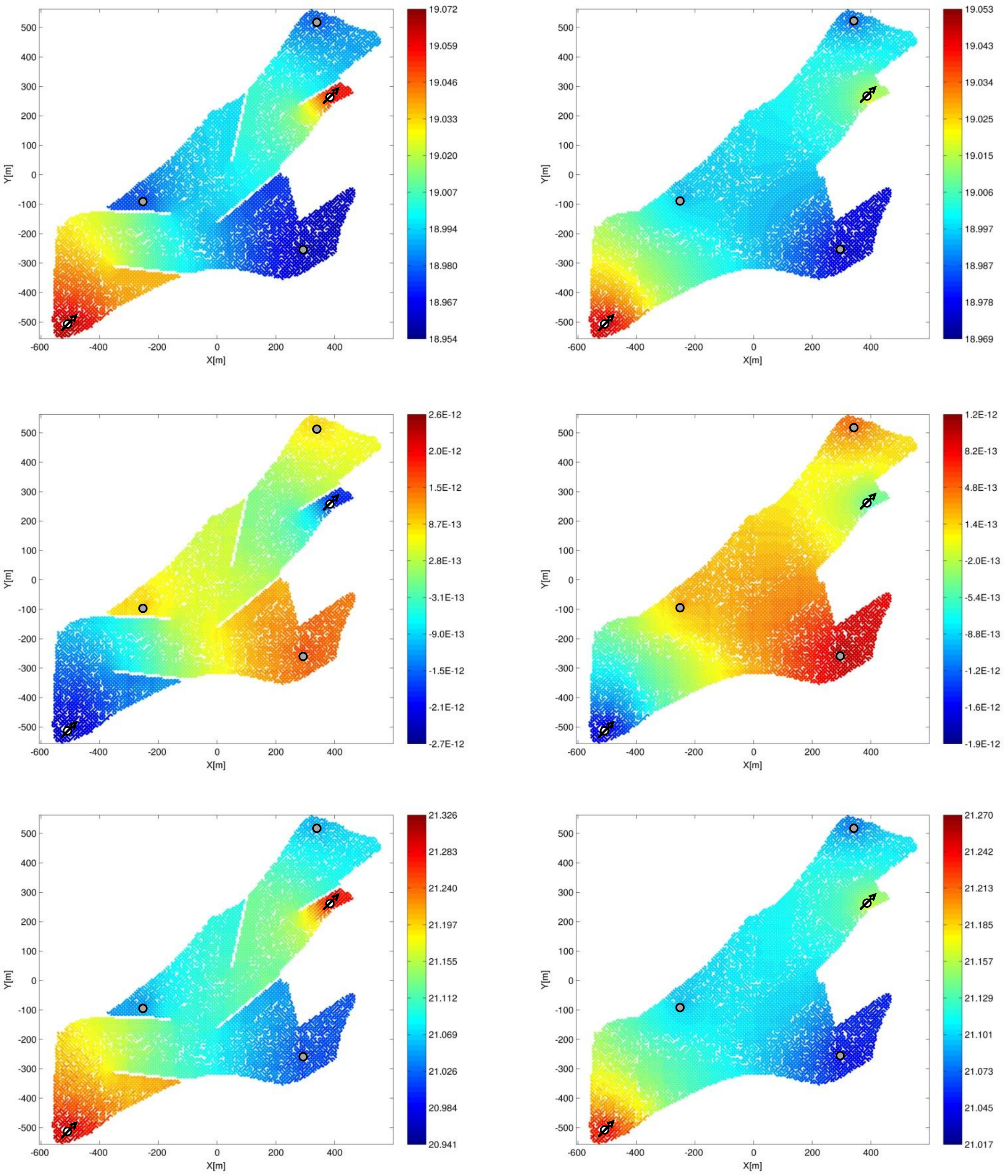

Figure 6-22. Distribution of the pore pressure, (top), fluid leak-off (middle), and fracture permeability (bottom) in the fracture network with (left) and without (right) sealing faults at the end of injection. Fracture permeability's unit is in Darcy x10^{-3} – Case 4.

In general as no flow barriers exist, less pressure at the injector well is needed and the distribution of the fluid leak-off, pressure, and even fracture permeability are more uniform within the domain with gradual spatial gradients.

Finally, the results in Figure 6-23 involving the comparison of the injecting and producing pressure reveals that the elastic faulted network presented lower pressure demands than the corresponding poroelastic case probably by the fact of neglecting the fracture interface flow rate which would involves additional pressure drops.

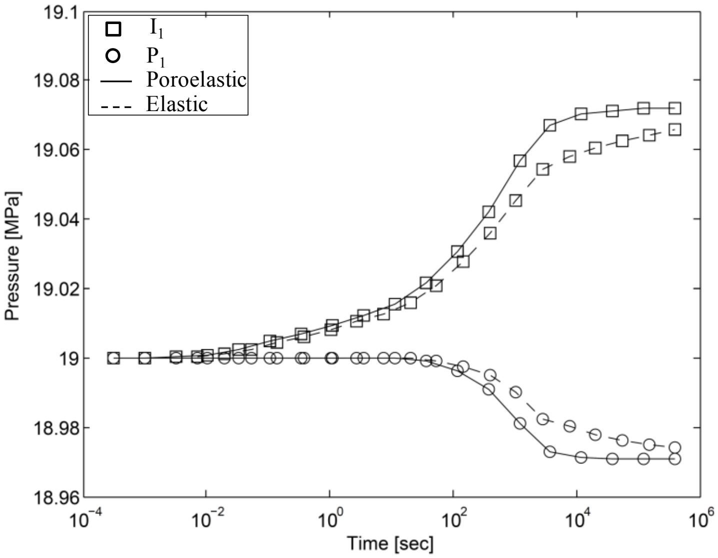

Figure 6-23. Comparison of the pressure at the injector and producer wells for the elastic and poroelastic fracture network with sealing faults – Case 4.

7. CONCLUSIONS AND RECOMMENDATIONS

DDM is commonly used for the solution of fracture problems in mining and hydraulic fracturing. However, it demands computing the influences among all elements so the resulting coefficient matrix is dense and nonsymmetrical and conventional strategies, either direct or iterative, for the solution of the system of equations are computationally intensive when large numbers of elements are involved. This work presents a novel approach to solve large-scale fracture problems using the Fast Multipole Method.

7.1. Conclusions

The main contributions and conclusions from this study are summarized as follow:

1. This work presented a new method called Fast Multipole-Displacement Discontinuity Method (acronymed as FM-DDM) for the efficient fluid flow-geomechanical simulations of large-scale naturally fractured reservoirs under injection and production operations.
2. FM-DDM was applied to simulate the response of field-scale geomechanical models of increasing complexity which account for the normal and shear deformation of fractures embedded in elastic and poroelastic rocks and for the changes in pore-pressure and fluid leak-off due to the flow through a two-dimensional network.

3. The accuracy of FM-DDM was evaluated through several synthetic case studies showing excellent agreement with both analytical and numerical solutions. In addition, the computational performance of the FMM approach and DDM were compared and analyzed after solving goemechanical models of increasing number of fractures. From the results, FM-DDM showed linear complexity in both memory and execution time outperforming the conventional method which demands quadratic and cubic requirements, as expected.
4. Using modest computational resources provided by personal computers, the FM-DDM approach was able to solve for larger problem sizes with up to two hundred thousand DOFs. A variety of large-scale geomechanical situations were successfully evaluated with FM-DDM involving the computation of interactions between transverse hydraulic fractures and a naturally fracture network, design of exploitation strategies in fractured reservoirs with vertical wells, and fast visualization of high-resolution stress distribution around fracture intersections for realistic representation and characterization of unconventional reservoirs.
5. By adopting a kernel-independent version of the classical FMM called Black-Box FMM, the programming complexity of our computational implementation was significantly reduced without the need for any analytical multipole and local expansions, opening a range of new potential applications within the geothermal and oil industries.

7.2. Recommendations

For further studies, the following topics are recommended:

1. Use FM-DDM to evaluate more industrial-oriented problems involving other geomechanical processes (e.g., hydraulic fracturing), physical phenomena (e.g., micro-earthquake), and study types (e.g., sensitivity analysis, characterization, optimization).
2. Extend FM-DDM to account for more complex situations such as 3D fracture networks, variable injection rate scenarios, and full poroelastic or thermal response.
3. Develop a pre-processing module for the automated meshing of stochastically generated fracture networks and improve the preconditioner stage of the iterative solver in order to get faster convergence when more irregular fracture distributions are evaluated.

NOMENCLATURE

a : Fracture half-length

A : Influence coefficient for normal an shear stresses by the displacement discontinuities

c : Elastic constant

c_f : Fluid compressibility

cn : Number of chebyshev nodes per dimension

c_t : Total compressibility of fracture

C : Fluid pressure coefficient between elements *i* and *j*

D : Displacement discontinuity

D_{max} : Maximum possible closure

f : Influence function of the fundamental solution of elastic rocks

G : Shear modulus

k_f : Fracture permeability

k_r : Matrix permeability

K : Joint stiffness

K_{ni} : Initial stiffness

K_m, Q_m : Kernel matrix and pseudo charge vector associated to the *m-th* matrix-vector product

ΔL : Fracture length (or $2a$)

m : Total fracture elements connected to the *ith* fracture

M : Biot's modulus

n : V_f / V_{ef}

N : Number of unknowns or degrees of freedom (DOF)

P : Pore-pressure

V_{ef} : Effective fracture void volume for fluid flow

V_f : Actual fracture void volume

q : Flow rate in the fracture

q_s : Injection or production rate (positive injection) per unit formation thickness

Q_l : Fluid leak-off rate per unit height

s : Spatial coordinate along the fracture length

t : Time

w_f : Fracture width or aperture

Symbols:

μ : Fluid viscosity

β : Angle counterclockwise from the x-axis to the fracture

α : Biot's coefficient

ϕ : Porosity

ϕ_d : Dilation angle

υ : Poisson’s ratio

σ : Stress

σ' : Effective stress

$\sigma\infty$: Field stress

Subscripts

i, j : Index of fracture segments

n, s : Normal and shear directions respect to the fracture orientation

p : Source components associated with the shear, normal displacement discontinuities, and fluid leak-off rate.

q : Effects over the tractions components (xx, yy, and xy) and pressure (p)

$\bar{x}, \bar{y}$: Coordinate direction in the local coordinate system

$\overline{xx}, \overline{yy}, \overline{xy}$: Directions of the stress components in the local coordinate system

x, y : Coordinate direction in the global coordinate system

Superscripts

i : ith fracture element

ξ : Current time step

h : Index of time step

$k, k+1$: Old and new time levels

REFERENCES

Ayachour, E.H. 2003. A Fast Implementation for Gmres Method. *J. Comput. Appl. Math.* **159** (2): 269-283.

Bagheri, M. and Settari, A. 2005. Modeling of Geomechanics in Naturally Fractured Reservoirs. Paper presented at the SPE Reservoir Simulation Symposium, The Woodlands, Texas.

Bängtsson, E. and Neytcheva, M. 2005. Algebraic Preconditioning Versus Direct Solvers for Dense Linear Systems as Arising in Crack Propagation Problems. *Communications in Numerical Methods in Engineering* **21** (2): 73-81.

Behnia, M., Goshtasbi, K., Golshani, A. et al. 2011. Numerical Modeling of Artificial Hydro-Fractures in Hot Dry Rock Reservoirs by Using Displacement Discontinuty Method. *Proceedings, Thirty-Sixth Workshop on Geothermal Reservoir Engineering*: pp. 344–355.

Behnia, M., Goshtasbi, K., Golshani, A.. 2012. On the Crack Propagation Modeling of Hydraulic Fracturing by a Hybridized Displacement Discontinuity/Boundary Collocation Method. *Journal of Mining and Environment (JME).*

Biot, M.A. 1941. General Theory of Three-Dimensional Consolidation. *Journal of Applied Physics* **12** (2): 155-164.

Board, J. and Schulten, K. 2000. The Fast Multipole Algorithm. *Computing in Science and Engg.* **2** (1): 76-79.

Cinco-Ley, H. and Samaniego-V., F. 1981. Transient Pressure Analysis for Fractured Wells. *Journal of Petroleum Technology* **33** (9): 1749-1766.

Crouch, S.S., A. 1984. Boundary Element Methods in Solid Mechanics. *International Journal for Numerical Methods in Engineering* **20** (6): 1175-1175.

Curran, J. and Carvalho, J.L. 1987. A Displacement Discontinuity Model for Fluid-Saturated Porous Media. Paper presented at the 6th ISRM Congress, Montreal, Canada. A.A. Balkema. Permission to Distribute - International Society for Rock Mechanics Congress-1987-014.

Elvin, N. and Leung, C. 1999. A Fast Iterative Boundary Element Method for Solving Closed Crack Problems. *Engineering Fracture Mechanics* **63** (5): 631-648.

Fong, W. and Darve, E. 2009. The Black-Box Fast Multipole Method. *Journal of Computational Physics* **228** (23): 8712-8725.

Fu, Y.H., Klimkowski, K.J., Rodin, G.J. et al. 1998. A Fast Solution Method for Three-Dimensional Many-Particle Problems of Linear Elasticity. *International Journal for Numerical Methods in Engineering* **42** (7): 1215-1229.

Goodman, R.E. 1976. *Methods of Geological Engineering in Discontinuous Rocks*: West Pub. Co. Original edition. ISBN 9780829900668.

Greengard, L. and Rokhlin, V. 1987. A Fast Algorithm for Particle Simulations. *Journal of Computational Physics* **73** (2): 325-348.

Jalali, M.R. and Dusseault, M.B. 2008. Coupled Fluid-Flow and Geomechanics in Naturally Fractured Reservoirs. International Society for Rock Mechanics (ISRM) and Iranian Society for Rock Mechanics (IRSRM) ISRM-ARMS5-2008-153.

Kolk, K., Weber, W., and Kuhn, G. 2006. Investigation of 3d Crack Propagation Problems Via Fast Bem Formulations. *Computational Mechanics* **37** (1): 32-40.

Lai, Y.-S. and Rodin, G.J. 2003. Fast Boundary Element Method for Three-Dimensional Solids Containing Many Cracks. *Engineering Analysis with Boundary Elements* **27** (8): 845-852.

Li, S. and Huang, Q. 2011. A New Fast Multipole Boundary Element Method for Two Dimensional Acoustic Problems. *Computer Methods in Applied Mechanics and Engineering* **200** (9–12): 1333-1340.

Liu, D. and Shen, G. 2005. Multipole Bem for 3-D Elasto-Plastic Contact with Friction. *Tsinghua Science and Technology* **10** (1): 57-60.

Liu, Y. 2009. *Fast Multipole Boundary Element Method*: Cambridge University Press. Original edition.

Liu, Y.J., Nishimura, N., and Yao, Z.H. 2005. A Fast Multipole Accelerated Method of Fundamental Solutions for Potential Problems. *Engineering Analysis with Boundary Elements* **29** (11): 1016-1024.

Morris, J.P. and Blair, S.C. 2000. An Efficient Displacement Discontinuity Method Using Fast Multipole Techniques, Presented at the Fourth North American Rock Mechanics Symposium, Seattle, Wa, 2000.

Nishimura, N., Yoshida, K., and Kobayashi, S. 1999. A Fast Multipole Boundary Integral Equation Method for Crack Problems in 3d. *Engineering Analysis with Boundary Elements* **23** (1): 97-105.

Peirce, A.P. and Napier, J.a.L. 1995. A Spectral Multipole Method for Efficient Solution of Large-Scale Boundary Element Models in Elastostatics. *International Journal for Numerical Methods in Engineering* **38** (23): 4009-4034.

Pham, A.D., Mouhoubi, S., Bonnet, M. et al. 2012. Fast Multipole Method Applied to Symmetric Galerkin Boundary Element Method for 3d Elasticity and Fracture Problems. *Engineering Analysis with Boundary Elements* **36** (12): 1838-1847.

Press, W.H. 1992. *Numerical Recipes in Fortran: The Art of Scientific Computing*: Cambridge University Press. Original edition. ISBN 9780521430647.

Rice, J.R. and Cleary, M.P. 1976. Some Basic Stress Diffusion Solutions for Fluid-Saturated Elastic Porous Media with Compressible Constituents. *Reviews of Geophysics* **14** (2): 227-241.

Sesetty, V. and Ghassemi, A. 2012. Simulation of Hydraulic Fractures and Their Interactions with Natural Fractures. American Rock Mechanics Association ARMA-2012-331.

Sesetty, V. and Ghassemi, A. 2013. Numerical Simulation of Sequential and Simultaneous Hydraulic Fracturing. InTech. Permission to distribute - International Society for Rock Mechanics ISRM-ICHF-2013-040.

Tao, Q., Ehlig-Economides, C., and Ghassemi, A. 2009a. Investigation of Stress-Dependent Fracture Permeability in Naturally Fractured Reservoirs Using a Fully Coupled Poroelastic Displacement Discontinuity Model. Paper presented at the SPE Annual Technical Conference and Exhibition, New Orleans, Louisiana. Society of Petroleum Engineers 124745.

Tao, Q., Ehlig-Economides, C.A., and Ghassemi, A. 2009b. Modeling Variation of Stress and Permeability in Naturally Fractured Reservoirs Using Displacement Discontinuity Method. Paper presented at the 43rd U.S. Rock Mechanics Symposium & 4th U.S. - Canada Rock Mechanics Symposium, Asheville, North Carolina. American Rock Mechanics Association 09-047.

Tao, Q. and Ghassemi, A. 2010. Simulation of Fluid Flow in a Naturally Fractured Poro-Thermoelastic Reservoir. Paper presented at the 44th U.S. Rock Mechanics Symposium and 5th U.S.-Canada Rock Mechanics Symposium, Salt Lake City, Utah. American Rock Mechanics Association 10-292.

Tao, Q., Ghassemi, A., and Ehlig-Economides, C.A. 2011. A Fully Coupled Method to Model Fracture Permeability Change in Naturally Fractured Reservoirs. *International Journal of Rock Mechanics and Mining Sciences* **48** (2): 259-268.

Tornberg, A.-K. and Greengard, L. 2008. A Fast Multipole Method for the Three-Dimensional Stokes Equations. *Journal of Computational Physics* **227** (3): 1613-1619.

Vandamme, L. and Roegiers, J.-C. 1990. Poroelasticity in Hydraulic Fracturing Simulators. *Journal of Petroleum Technology* **42** (9): 1199-1203.

Wang, H. 2000. *Theory of Linear Poroelasticity with Applications to Geomechanics and Hydrogeology*: Princeton University Press. Original edition. ISBN 9780691037462.

Wang, H., Yao, Z., and Wang, P. 2005. On the Preconditioners for Fast Multipole Boundary Element Methods for 2d Multi-Domain Elastostatics. *Engineering Analysis with Boundary Elements* **29** (7): 673-688.

Wang, H.T. and Yao, Z.H. 2005. A New Fast Multipole Boundary Element Method for Large Scale Analysis of Mechanical Properties in 3d Particle-Reinforced Composites. *Cmes-Computer Modeling in Engineering & Sciences* **7** (1): 85-95.

Wang, P., Yao, Z., and Wang, H. 2005. Fast Multipole Bem for Simulation of 2-D Solids Containing Large Numbers of Cracks. *Tsinghua Science and Technology* **10** (1): 76-81.

Wang, P., Yao, Z., and Wei, Y. 2007. Fm-Bem Evaluation for Effective Elastic Moduli of Microcracked Solids. *Tsinghua Science and Technology* **12** (5): 562-566.

Wang, P.B. and Yao, Z.H. 2006. Fast Multipole Dbem Analysis of Fatigue Crack Growth. *Computational Mechanics* **38** (3): 223-233.

Wu, K. and Olson, J. 2013. Investigation of Critical in Situ and Injection Factors in Multi-Frac Treatments: Guidelines for Controlling Fracture Complexity. Paper presented at the 2013 SPE Hydraulic Fracturing Technology Conference, The Woodlands, TX, USA. Society of Petroleum Engineers SPE-163821-MS.

Yao, Z.H., Wang, P.B., Lei, T. et al. 2007. Large-Scale Boundary Element Analysis in Solid Mechanics Using Fast Multipole Method. In *Computational Methods in Engineering & Science*: Springer Berlin Heidelberg.

Ying, L.X., Biros, G., and Zorin, D. 2004. A Kernel-Independent Adaptive Fast Multipole Algorithm in Two and Three Dimensions. *Journal of Computational Physics* **196** (2): 591-626.

Yoshida, K.-I., Nishimura, N., and Kobayashi, S. 2001a. Application of Fast Multipole Galerkin Boundary Integral Equation Method to Elastostatic Crack Problems in 3d. *International Journal for Numerical Methods in Engineering* **50** (3): 525-547.

Yoshida, K.-I., Nishimura, N., and Kobayashi, S. 2001b. Application of New Fast Multipole Boundary Integral Equation Method to Crack Problems in 3d. *Engineering Analysis with Boundary Elements* **25** (4–5): 239-247.

Yoshida, K. Applications of Fast Multipole Method to Boundary Integral Equation Method, Ph.D. Thesis, Department of Global Environment Engineering, Kyoto University, Japan.

Zhou, X. and Ghassemi, A. 2011. Three-Dimensional Poroelastic Analysis of a Pressurized Natural Fracture. *International Journal of Rock Mechanics and Mining Sciences* **48** (4): 527-534.

APPENDIX A

FAR-FIELD APPROXIMATION OF KERNELS FOR THE STRESSES DUE TO THE DISPLACEMENT DISCONTINUITIES

Let write the product of the displacement discontinuity vector and the matrix kernel in Eqs. (2-8) to (2-10):

$$\begin{bmatrix} \sigma_{\overline{xx}}^{i,j} \\ \sigma_{\overline{yy}}^{i,j} \\ \sigma_{\overline{xy}}^{i,j} \end{bmatrix} = c \begin{bmatrix} \left(K_{\overline{xx},s}\right)^{i,j} & \left(K_{\overline{xx},n}\right)^{i,j} \\ \left(K_{\overline{yy},s}\right)^{i,j} & \left(K_{\overline{yy},n}\right)^{i,j} \\ \left(K_{\overline{xy},s}\right)^{i,j} & \left(K_{\overline{xy},n}\right)^{i,j} \end{bmatrix} \begin{bmatrix} D_s^j \\ D_n^j \end{bmatrix} \tag{A-1}$$

For compactness, let express the six (6) kernels of the matrix above as follow:

$$\left(K_{\overline{xx},s}\right)^{i,j} = K_1 + K_2 \tag{A-2}$$

$$\left(K_{\overline{yy},s}\right)^{i,j} = K_1 - K_2 \tag{A-3}$$

$$\left(K_{\overline{xy},s}\right)^{i,j} = K_3 \tag{A-4}$$

$$\left(K_{\overline{xx},n}\right)^{i,j} = -K_4 + K_5 \tag{A-5}$$

$$\left(K_{\overline{yy},n}\right)^{i,j} = -K_4 - K_5 \tag{A-6}$$

$$\left(K_{\overline{xy},n}\right)^{i,j} = K_6 \tag{A-7}$$

where

$$K_1 = F_4 \tag{A-8}$$

$$K_2 = (F_4 + F_6\bar{y}^i)cos2\beta_j + (F_5 - F_7\bar{y}^i)sin2\beta_j \tag{A-9}$$

$$K_3 = (-F_5 + F_7\bar{y}^i)cos2\beta_j + (F_4 + F_6\bar{y}^i)sin2\beta_j \tag{A-10}$$

$$K_4 = F_5 \tag{A-11}$$

$$K_5 = F_7\bar{y}^i cos2\beta_j + F_6\bar{y}^i sin2\beta_j \tag{A-12}$$

$$K_6 = -F_6\bar{y}^i cos2\beta_j + F_7\bar{y}^i sin2\beta_j \tag{A-13}$$

Note that computing the effects of the jth fracture (source) into the ith fracture (field) using kernels in Eq. (A-1) involves proper coordinate transformations of the relative location between both fractures from the global (x,y) to the local ($\bar{x}, \bar{y}$) system using Eqs. (2-6) and (2-7). In addition, note that the final induced stresses ($\sigma_{\overline{xx}}, \sigma_{\overline{yy}}, \sigma_{\overline{xy}}$) are expressed for the local ($\bar{x}, \bar{y}$) system of the ith fracture segment so additional transformations are necessary to rotate it to the global (x,y) one.

Table A1 shows the far-field approximations at global coordinates of the kernels in Eqs. (A-8) to (A-13). Note in Table A1 that the term mvp means the number of matrix-vector products (and then multipole approximations) necessary for the evaluation of kernels K_1 to K_6 at local coordinates $(\bar{x}, \bar{y})$ using kernel expressions (enclosed by parenthesis) at global coordinates (x, y). A total of ten (10) multipole approximations with sixteen (16) mvp are required for this approximation. For instance, to evaluate kernel K_1 at $(\bar{x}, \bar{y})$ is necessary to execute and sum two (2) multipole approximations of F_4 and F_5 at (x, y), grouping the terms $cos2\beta_j$ and $sin2\beta_j$ with the unknown vector, respectively.

Table A1 –Far-field approximation of kernels in Eqs. (A-8) to (A-13)

Kernel $(\bar{x},\bar{y})$	Kernel (x,y)	mvp
K_1	$(F_4)cos2\beta_j-(F_5)sin2\beta_j$	2
K_2	$\frac{1}{2}(2F_4-F_7.x+F_6y)+\frac{1}{2}(F_7.x+F_6.y)cos2\beta_j+\frac{1}{2}(-F_6.x+F_7.y)sin2\beta_j$	3
K_3	$\frac{1}{2}(-2F_5+F_6.x+F_7.y)+\frac{1}{2}(-F_6.x+F_7.y)cos2\beta_j-\frac{1}{2}(F_7.x+F_6.y)sin2\beta_j$	3
K_4	$(F_4)sin2\beta_j+(F_5)cos2\beta_j$	2
K_5	$(F_6.x)sin^2\beta_j-(y.F_6+x.F_7)sin\beta_j cos\beta_j+(F_7.y)cos^2\beta_j$	3
K_6	$-(F_6.y)cos^2\beta_j+(x.F_6-y.F_7)sin\beta_j cos\beta_j+(F_7.x)sin^2\beta_j$	3

APPENDIX B

POROELASTIC KERNELS OF PORE-PRESSURE AND INDUCED STRESSES DUE TO THE FLUID LEAK-OFF

$$p^{Q_l} = \frac{\mu}{4\pi k} \int_{-a}^{a} E_i(\xi^2)\,dx' \tag{B-1}$$

$$\begin{aligned}\sigma_{\overline{xx}}^{Q_l} = \frac{\alpha\mu}{8\pi k}\frac{(1-2\upsilon)}{(1-\upsilon)}\Bigg\{\left[-(x-x')\left(\frac{1}{\xi^2}-\frac{e^{-\xi^2}}{\xi^2}+E_1(\xi^2)\right)\right]\Bigg|_{-a}^{a} \\ - 2\int_{-a}^{a} E_i(\xi^2)\,dx'\Bigg\}\end{aligned} \tag{B-2}$$

$$\sigma_{\overline{yy}}^{Q_l} = \frac{\alpha\mu}{8\pi k}\frac{(1-2\upsilon)}{(1-\upsilon)}\left[(x-x')\left(\frac{1}{\xi^2}-\frac{e^{-\xi^2}}{\xi^2}+E_1(\xi^2)\right)\right]\Bigg|_{-a}^{a} \tag{B-3}$$

$$\sigma_{\overline{xy}}^{Q_l} = \frac{\alpha\mu}{8\pi k}\frac{(1-2\upsilon)}{(1-\upsilon)}\left[-y\left(\frac{1}{\xi^2}-\frac{e^{-\xi^2}}{\xi^2}+E_1(\xi^2)\right)\right]\Bigg|_{-a}^{a} \tag{B-4}$$

APPENDIX C

ANALYTICAL EXPRESSIONS FOR THE FAR-FIELD APPROXIMATION OF POROELASTIC KERNELS

The mathematical expressions to approximate the poroleastic kernels in Eqs. (4-22) to (4-26) are presented below:

$$M_1 = \frac{xy}{r^4} \tag{C-1}$$

$$M_2 = \frac{(x^2 - y^2)}{r^4} \tag{C-2}$$

$$M_3 = \frac{e^{-\xi^2}}{\mathrm{r}^2} \tag{C-3}$$

$$M_4 = \frac{e^{-\xi^2}}{\mathrm{r}^4} \tag{C-4}$$

where

$$c = M\frac{k}{\mu} \tag{C-5}$$

$$M = \frac{1}{\left(\phi c_f + 3(\alpha - \phi)(1 - \alpha)\dfrac{(1 - 2v)}{2G(1 + v)}\right)} \tag{C-6}$$

$$d = tc\frac{\alpha\mu(1 - 2v)}{8\pi k(1 - v)} \tag{C-7}$$

APPENDIX D

ASSEMBLE OF ELASTIC AND POROELASTIC KERNELS FOR THE COMPUTATION OF TRACTIONS COMPONENTS

If a *j-th* fracture element is considered, the traction components at the x, y global coordinate is computed by multiplying the kernel matrix at the $\bar{x}$, $\bar{y}$ local system, the rotation matrix, and the unknown vector (Tao et al. 2009a; Tao and Ghassemi 2010):

$$\begin{bmatrix} \Delta\sigma_{\mathrm{xx}} \\ \Delta\sigma_{\mathrm{yy}} \\ \Delta\sigma_{\mathrm{xy}} \end{bmatrix} = \begin{bmatrix} \sigma_{\overline{xx}}^{D_n} & \sigma_{\overline{xx}}^{D_s} & \sigma_{\overline{xx}}^{Q_l} \\ \sigma_{\overline{yy}}^{D_n} & \sigma_{\overline{yy}}^{D_s} & \sigma_{\overline{yy}}^{Q_l} \\ \sigma_{\overline{xy}}^{D_n} & \sigma_{\overline{xy}}^{D_s} & \sigma_{\overline{xy}}^{Q_l} \end{bmatrix} \begin{bmatrix} cos\beta_j{}^2 & sin\beta_j{}^2 & -sin2\beta_j \\ sin\beta_j{}^2 & cos\beta_j{}^2 & sin2\beta_j \\ cos\beta_j sin\beta_j & -cos\beta_j sin\beta_j & cos\beta_j{}^2 - sin\beta_j{}^2 \end{bmatrix} \begin{bmatrix} \Delta D_n \\ \Delta D_s \\ \Delta Q_l \end{bmatrix} \tag{D-1}$$

The effects of the displacement discontinuities and fluid leak-off rate over the tractions can be separated by splitting the corresponding components in the kernel matrix as:

$$\begin{bmatrix} \sigma_{\overline{xx}}^{D_n} & \sigma_{\overline{xx}}^{D_s} & \sigma_{\overline{xx}}^{Q_l} \\ \sigma_{\overline{yy}}^{D_n} & \sigma_{\overline{yy}}^{D_s} & \sigma_{\overline{yy}}^{Q_l} \\ \sigma_{\overline{xy}}^{D_n} & \sigma_{\overline{xy}}^{D_s} & \sigma_{\overline{xy}}^{Q_l} \end{bmatrix} = \begin{bmatrix} \sigma_{\overline{xx}}^{D_n} & \sigma_{\overline{xx}}^{D_s} & 0 \\ \sigma_{\overline{yy}}^{D_n} & \sigma_{\overline{yy}}^{D_s} & 0 \\ \sigma_{\overline{xy}}^{D_n} & \sigma_{\overline{xy}}^{D_s} & 0 \end{bmatrix}_{\Delta D_{n,s}} + \begin{bmatrix} 0 & 0 & \sigma_{\overline{xx}}^{Q_l} \\ 0 & 0 & \sigma_{\overline{yy}}^{Q_l} \\ 0 & 0 & \sigma_{\overline{xy}}^{Q_l} \end{bmatrix}_{\Delta Q_l} \tag{D-2}$$

After introducing Eq. (D-2) into Eq. (D-1), the final traction components can be expressed as the contribution of two (2) separated effects:

$$\begin{bmatrix} \Delta\sigma_{xx} \\ \Delta\sigma_{yy} \\ \Delta\sigma_{xy} \end{bmatrix} = \begin{bmatrix} \Delta\sigma_{xx} \\ \Delta\sigma_{yy} \\ \Delta\sigma_{xy} \end{bmatrix}_{\Delta D_{n,s}} + \begin{bmatrix} \Delta\sigma_{xx} \\ \Delta\sigma_{yy} \\ \Delta\sigma_{xy} \end{bmatrix}_{\Delta Q_l} \tag{D-3}$$

Note that computing the tractions associated with the displacement discontinuities ($D_{n,s}$) has been described in Appendix A for elastic rocks. The current FMM approach accounts additionally for the poroleastic effects due to the fluid leak-off rate (Q_l) as expressed below:

$$\begin{bmatrix}\Delta\sigma_{\mathrm{xx}}\\ \Delta\sigma_{\mathrm{yy}}\\ \Delta\sigma_{\mathrm{xy}}\end{bmatrix}_{\Delta Q_l}=\begin{bmatrix}\sigma_{xx}^{Q_l}\cos\beta_{\mathrm{j}}{}^2+\sigma_{yy}^{Q_l}\sin\beta_{\mathrm{j}}{}^2-\sigma_{xy}^{Q_l}sin2\beta_j\\ \sigma_{xx}^{Q_l}\sin\beta_{\mathrm{j}}{}^2+\sigma_{yy}^{Q_l}\cos\beta_{\mathrm{j}}{}^2+\sigma_{xy}^{Q_l}sin2\beta_j\\ \sigma_{xx}^{Q_l}\cos\beta_{\mathrm{j}}\sin\beta_{\mathrm{j}}-\sigma_{yy}^{Q_l}\cos\beta_{\mathrm{j}}\sin\beta_{\mathrm{j}}+\sigma_{xy}^{Q_l}\left(\cos\beta_{\mathrm{j}}{}^2-\sin\beta_{\mathrm{j}}{}^2\right)\end{bmatrix}\Delta Q_l \qquad \text{(D-4)}$$

Corresponding mathematical expressions for the far-field approximation of kernels $\sigma_{xx}^{Q_l}$, $\sigma_{yy}^{Q_l}$, and $\sigma_{xy}^{Q_l}$ are found in Eqs. (4-22) to (4-24). Note that after proper simplification of elastic and poroelastic terms, only a total of 14 unique multipole approximations with 28 *mvp* are needed.